A Hybrid Computational Framework for the Simulation of Ships Maneuvering In Waves

by

Paul F. White

A dissertation submitted in partial fulfillment
of the requirements for the degree of
Doctor of Philosophy
(Naval Architecture and Marine Engineering)
in The University of Michigan
2020

Doctoral Committee:

Associate Professor Kevin Maki, Chair
Associate Professor Eric Johnsen
Doctor Dominic Piro, Navatek Ltd.
Professor Armin Troesch
Professor Yin Lu Young

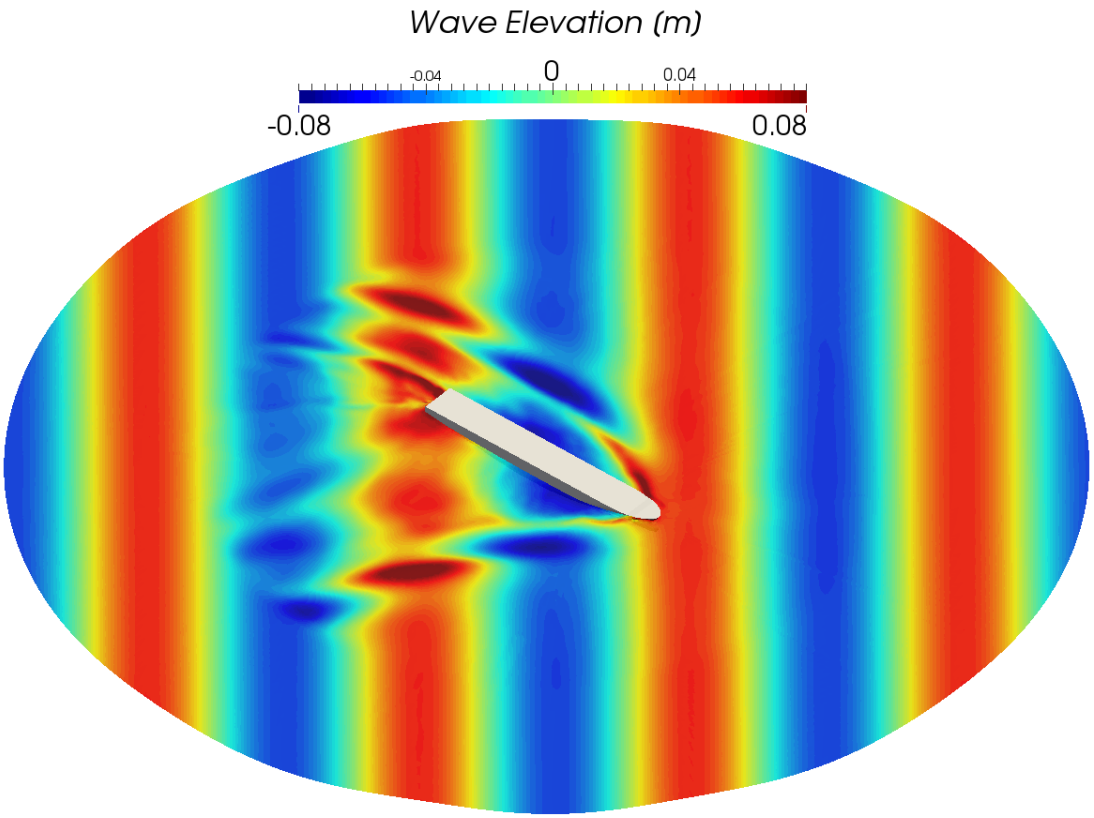

Duisburg Test Case hull turning circle computation in waves.

Paul F. White
pfwhite@umich.edu
ORCID id: 0000-0002-5805-4226

To my wife Heidi and my parents Linda and Mike.

ACKNOWLEDGEMENTS

Many people have made an impact on me throughout my studies. I begin by offering thanks to my friends and peers, especially those in the CSHL (Computational Ship Hydrodynamics Lab). You've generously shared your knowledge and created a rich environment for research. Above all, you made the NAME department a fun place to conduct research.

I want to extend special thanks to my advisor, Professor Kevin Maki, for his guidance throughout my studies. Kevin's love for teaching and all things related to marine hydrodynamics always made for easy conversation with him. Kevin's guidance and advise has taught me to be a better researcher and a better person.

Many thanks are owed to Dr. Dominic Piro who helped adapt and develop the software, Aegir, for my use in this thesis. Dominic shared a great deal of time and knowledge with me regarding the theory and implementation in Aegir. Our collaboration is something I will not forget.

I wish to thank Professor Eric Johnsen, Professor Armin Troesch, and Professor Julie Young for sitting on my committee. Your feedback and constructive critique was immensely helpful in the quality construction of this thesis.

A need to thank Professor Bob Beck also comes to the forefront of my mind. From the first Naval Architecture class I enrolled in at Michigan and continuing through his transition into Emeritus status, Bob's vigor for hydrodynamics shines through. Even in "semi-retirement" Bob has been especially generous in lending me his time and sharing his expertise.

I am thankful for my family's and my friends' perpetual support through all my years of schooling. My parents Linda and Mike have always supported my academic goals by offering their nurturing love, encouragement, and guidance. Mostly, you've helped me stay level-headed when in rough waters.

I owe my wife Heidi the most thanks of all. Throughout the most-trying periods of my journey to earn a PhD, if something went wrong, she was the first to hear about it. If I reached a success, she was by my side to celebrate. Her love, patience, and endearment gives me the strength and pride to carry on.

Lastly, I wish to acknowledge the Office of Naval Research as my source of funding. The opportunities provided to me allowed me to research freely and independently. The funding also provided opportunities to travel and collaborate with colleagues around the world, experiences I will cherish for the rest of my life.

TABLE OF CONTENTS

LIST OF FIGURES

Figure

LIST OF TABLES

Table

LIST OF APPENDICES

Appendix

LIST OF ABBREVIATIONS

AMI Arbitrary Mesh Interface

BEM Boundary Element Method

BIE Boundary Integral Equation

BVP Boundary Value Problem

CFD Computational Fluid Dynamics

DTC Duisburg Test Case

FCT Flux Corrected Transport

FOAM Field Operation and Manipulation

FVM Finite Volume Method

HPC High Performance Computer

KCS Korea Research Institute of Ships and Ocean Engineering Container Ship

NURBS Non-Uniform Rational B-Spline

RAO Response Amplitude Operator

VOF Volume-of-Fluid

RANS Reynolds-averaged Navier-Stokes

ABSTRACT

The maneuvering characteristics of a ship directly impact its safety of navigation, economy, environmental impact, and overall operational efficiency. Ships are routinely tasked to perform basic maneuvers that involve turning, stopping and backing, and course keeping. However, vessels are also required to execute challenging maneuvers such as taking evasive action or maintaining course in adverse weather. The performance of the vessel must be adequate in various water depths, in confined or open water, and in a multitude of environmental conditions. While most ship maneuvering analysis has been done in calm water, and seakeeping performance analyzed entirely separately, vessels regularly need to maneuver in a seaway, where wave forces can have an important influence on ship maneuverability. Consequently, predictive tools are necessary in ship design in order to evaluate the maneuvering response of vessels in both calm water and in waves.

This thesis formulates a novel computational approach to simulate ships maneuvering in waves. To resolve wave forces, viscous forces, and propeller forces entirely through use of Computational Fluid Dynamics (CFD) is computationally expensive. The spatial and temporal discretization requirements lead to very large problem sizes that are expensive to solve even with high performance parallel computing. The method proposed here takes a hybrid approach where multiple numerical methods are selected for their strengths and efficiencies. A single-phase Reynolds-averaged Navier-Stokes solver is utilized to solve for the slowly-varying viscous-dominated horizontal plane forces common to a ship maneuvering in calm water. A propeller force model is utilized to predict the time-varying propeller loads. The discrete propeller

is therefore omitted from the CFD, allowing a significantly larger time step to be taken. The induced velocity from the propeller is introduced into the CFD through a momentum source disk.

A linearized time-domain high-order Boundary Element Method (BEM) is used to model all unsteady wave forcing. The time-domain BEM predicts first-order wave forces with zero mean value and second-order forces that are derived from first-order quantities. The second-order wave loads are computed in a postprocessing step after the solution to the first-order seakeeping problem, providing an efficient means of computing wave forces.

The proposed hybrid simulation method is tested in two case studies: maneuvering of the Duisburg Test Case hull form and maneuvering of the KRISO Container Ship. The hybrid method is compared to high-fidelity CFD results computed using a two-phase solver with free-surface capturing by the Volume-of-Fluid method. The maneuvering trajectories computed with the hybrid method are found to compare favorably with the nonlinear results produced using the two-phase solver. Moreover, the hybrid simulation method shows (at minimum) a factor of ten reduction in computational cost for all cases tested herein, hence showing promise as an efficient option for simulation of ships maneuvering in waves.

CHAPTER I

Introduction

The maneuvering characteristics of a surface ship play a critical role in the safety of navigation both in port and in an open seaway, and are paramount to the overall operational efficiency of the ship. Thus, having predictive tools to analyze maneuvering capabilities of ships in calm water and in waves is necessary during the ship design process. Further, the classification status of a vessel with its flag state is contingent upon a baseline requisite maneuvering ability. The American Bureau of Shipping has adopted the International Maritime Organization's Maritime Safety Committee resolution on standards for ship maneuverability. The guidelines define minimum recommendatory capabilities for course keeping, turning, and stopping abilities of a ship (American Bureau of Shipping, 2017).

The American Bureau of Shipping guidelines specify three methods for provisional determination of the vessel's maneuvering capabilities, with eventual validation of the predictions made during full-scale sea trials. The suggested methods are comparative predictions based on similar hull forms, free-running trials at model-scale, and numerical simulations. This thesis focuses specifically on predictive methods utilizing numerical simulation.

The challenge of numerically predicting a vessel's ability to maneuver in the design phase exists due to the demanding computational costs associated with numerical

simulation of the underlying, complex physics of a ship maneuver. A purely computational approach is appealing over an experimental test campaign because the design space can be investigated more rapidly in a virtual setting, where multiple environments or tests can be executed simultaneously. Experimental approaches to maneuvering prediction, while accurate, have inherent error sources as well. Furthermore, physical testing requires manufacturing of the physical model, instrumentation of the model, and access to facilities where the experiments can be performed. Experimental ship maneuvering prediction methods are also limited by wave basin or towing tank size and the consequential physical scaling effects arising from a limited model scale; a numerical approach holds promise for simulation at full scale.

Thus a strong incentive exists for development of a purely numerical approach to determine maneuvering behavior of ships. A variety of numerical prediction methods already exist, each with its own strengths and limitations. Potential-flow methods have been used successfully for many years to predict seakeeping motions of ships. However, potential-flow methods inherently lack the ability to predict viscous forces important to predict the maneuvering capabilities of a ship. Alternatively, use of Computational Fluid Dynamics (CFD) to simulate ship maneuvers shows promise as a viable alternative to model testing. Yet, inclusion of a discretized, rotating propeller presents one of the more costly aspects to simulating free maneuvers with CFD due to the small time step needed to resolve transient flow over the propeller. Also, mesh resolution requirements for accurate propagation of free surface waves lead to large problem sizes that are prohibitively expensive to solve even with modern parallel computing techniques.

The numerical framework presented in this thesis proposes a hybrid approach, where a single-phase CFD computation is used to compute viscous-dominated forces governing the maneuver and a potential-flow method is incorporated for efficient modeling of unsteady wave effects. In this manner, wave modeling can be removed

entirely from the CFD, presenting an opportunity to reduce dense mesh resolution in the far-field. In addition to coarser meshes, the hybrid method allows for a larger time step than would otherwise be needed to accurately propagate a numerical wave in the CFD. The efficiency gain from reducing CFD mesh size is joined by temporal discretization time savings achieved through use of a propulsion model instead of a discrete, rotating propeller within the CFD. The unique combination of numerical methods used to predict components of the total hydrodynamic force provides an appealing framework that offers the accuracy of CFD methods but at a reduced computational expense.

1.1 Literature Review of Maneuvering Prediction Methods

An overview of approaches to predict the maneuvering characteristics of ships is given in this section. The methods mentioned here do not constitute an exhaustive list but rather provide a selection of historically popular methods as well as the state-of-the-art practices. Figure 1.1 is adapted from ITTC (2008) and provides a wholistic view of different predictive approaches for ship maneuvering. This literature review covers the methods in Figure 1.1, first in the context of maneuvering in calm water and then describes extensions of those methods, where possible, to maneuvering prediction in waves.

Methods for predicting ship maneuverability can be classified into three categories. The first category is labeled as "Experimental Methods" and includes physical model testing at model scale up to and including full-scale sea trials. This category is perhaps the most historically relevant as shipbuilding was largely experiential before naval architecture introduced a scientific approach to ship design. Before mathematical models were invented to model the problem of a ship maneuvering, and before the advent of modern computing, ship design was driven by testing and observation at full-scale. Successful hull forms were absorbed into shipwrights' collective knowledge

database and future designs were born from past successful designs.

Present day experimental procedures typically work at model scale and overlap a significant amount with the second category: "Systems Based Maneuvering Simulation". Systems-based methods all share one common aspect; they each feature, to some degree, a mathematical model formulated on experimental data. One of the most popular mathematical models was introduced in the pioneering work of Abkowitz (1964). Abkowitz-style methods all feature a multivariate higher-order polynomial with coefficients representing perturbations to the total hydrodynamic force as a function of the vessel state vector. For instance, a low-order term that might appear in the polynomial for hydrodynamic surge force could be $X_r r$ where X_r is called a hydrodynamic derivative. When X_r is multiplied by the yaw-rate, r, the model produces the appropriate change to surge force. An Abkowitz-style force model does require *a priori* definition of the full mathematical form. The work by Strøm-Tejsen and Chislett (1966) gives an exposition on the testing campaign necessary to populate an Abkowitz-style maneuvering force model. In that work, over forty hydrodynamic derivatives are derived, with some coefficients requiring multiple model captive model tests where the vessel is prescribed along a certain trajectory and hydrodynamic forces are measured on the total system.

The number of model tests required to populate an Abkowitz-style model is costly. To this end, a separate group of methods was developed to make use of theory and empiricism where possible to reduce the number of physical model tests needed to build the model. This class of method, closely related to the works by Abkowitz, is known as the Maneuvering Modeling Group (MMG) method (Yasukawa and Yoshimura, 2015). Amongst other purposes, one main objective of the MMG method was to increase the adaptability of the method. The MMG method achieves this by taking a modular approach to force determination, rather than fitting functions to hydrodynamic derivatives that produce the total hydrodynamic force on the combined hull,

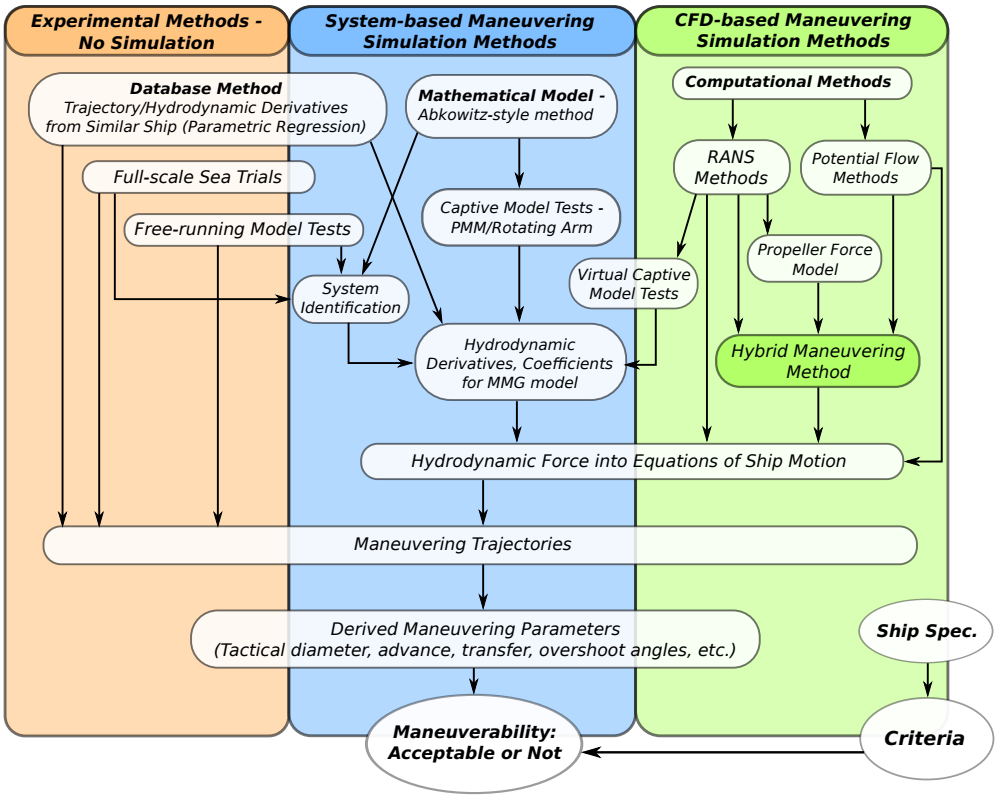

Figure 1.1: Maneuvering simulation methods overview. Figure adapted from ITTC (2008).

rudder, appendage, propeller system. To facilitate a modular approach, theory is melded with physical test data for modeling propeller and rudder forces, their interactions with one another, and their interactions with the hull. The Japan Society of Naval Architects and Ocean Engineers has developed a standardized procedure for developing these semi-empirical models called the "MMG standard method".

A limitation of both the Abkowitz-style models and the MMG models is that coefficients are often derived about a baseline speed and model tests performed to populate the hydrodynamic coefficients may not encounter all states a vessel is exposed to during a maneuver. In essence, the concern is that the physical model tests could overlook relevant physics. Further, the richness of the model is bound by the chosen functional form of the modified Taylor-series representation of the hydrodynamic forces. A class of methods, called "System Identification Methods" here and

in Figure 1.1, was developed to broaden the generality of the force model by exposing the model to a greater variety of states in the physical model tests. Furthermore, these methods are often able to utilize free running model tests, rather than captive model tests, which is closer in principle to the actual state of a ship (model) executing a free maneuver.

The "System Identification" class of methods still requires a functional definition of the total hydrodynamic force but it can often afford to be more complex as compared to the functional form of a model to be built from captive model testing. The reason why more complexity is possible is that "System Identification" techniques often employ machine learning and optimization techniques to obtain the best functional fit for the hydrodynamic derivatives. A downside of "System Identification" techniques is that the physical hydrodynamic force is generally not measured as the tests are free running, and so determination of the hydrodynamic derivative is based on error between predicted state variables and measured experimental values. Representative works using the "System Identification" approach to maneuvering prediction include those of Oltmann (1993), Luo et al. (2013), and Bonci et al. (2015).

The use of CFD for the solution of maneuvering problems has increasingly gained popularity, much of it within the last decade. An outcome of the Workshop on Verification and Validation of Ship Manoeuvring Simulation Methods (SIMMAN 2008) was the conclusion that CFD methods show promise in solving ship maneuvering problems but still have need for improved accuracy before they become widely accepted.

Application of CFD for the solution of free-running zigzag tests and turning circle maneuvers in calm-water is gradually becoming common practice. In the work of Carrica et al. (2013) the authors simulate a 20/20 zigzag maneuver and a 35° turning circle for the 5415 combatant hull in calm water using RANS CFD computations with a level-set free-surface capturing scheme. Shen et al. (2015) simulates a 10/10 zigzag maneuver and a modified 15/1 zigzag maneuver for the Korea Research Institute of

Ships and Ocean Engineering Container Ship (KCS) using a RANS CFD solver with VOF free-surface capturing.

The aforementioned methods were initially developed for application towards solving calm-water maneuvering problems. Several of the methods have extensions to solving maneuvers in waves and are now reviewed. The computational methods have the most relevance in comparison to the framework developed in this thesis and so deserve a thorough description, but first a brief review of experimental methods for ships maneuvering in waves is provided.

Experimental investigation of ships maneuvering in waves is not a well-documented subject and there exists a scarcity of published results in the public domain. Currently an interest is growing within the field, driving attention towards the variability in ship maneuverability in a seaway as compared to in calm water. Yasukawa and Nakayama (2009) completed turning circle experiments in waves for the single-rudder, single-screw S-175 container ship. The experiments tested turns to both port and starboard into an initial head seas regular wave field for four different wavelengths. The experiments also made port and starboard turns for the vessel initially in beam seas, again using four different regular waves.

More recently Sanada et al. (2013) completed experiments for the ONR Tumblehome hull in contribution to the Tokyo 2015 CFD Workshop (Larsson et al., 2015). The experiments executed zigzag tests in head and following seas and turning circle maneuvers in waves.

The maneuvering characteristics in waves were experimentally tested for a post-Panamax container ship (Duisburg Test Case) in affiliation with the European Union funded Energy Efficient Safe Ship Operation (SHOPERA) project (el Moctar et al., 2016). The experiments related to that project mainly focused on maneuvering in shallow waters at low speed, though some low speed turning circles and zigzag maneuvers in waves were tested. An objective of the SHOPERA project was to answer

concerns about maneuverability of ships given the decreasing installed power in the next generation of energy-efficient ships.

The system-based methods previously mentioned, that build mathematical models for the hydrodynamic force, have also been extended to solve maneuvers in waves. One of the first extensions of an Abkowitz-style model to include wave drift forces was the work of Hirano et al. (1980). In this work the authors test a Ro-Ro ship model executing turns in waves of different lengths. This work also introduces a precomputed mean drift force assuming zero-speed and using a far-field momentum conservation method such as Maruo (1960).

The computational efforts by Hirano et al. (1980) motivated two types of extensions to include waves using system-based formulations, namely, "Unified Methods" and "Two-Time-Scale Methods". The unified methods are developed similarly to how the hydrodynamic derivatives would be populated for purposes of simulating calm-water maneuvers. The primary difference is that frequency dependent coefficients, particularly the linear degrees of freedom related to wave radiation and memory effects, are replaced with convolution integrals or an approximation thereof such as in McCreight (1986) and Fossen (2005). These methods are fast-running and popular in real-time simulators and control system design, but ultimately they suffer from their treatment of higher-order wave loads. These methods capture some nonlinearity by transforming linear terms from the seakeeping computations into the body-fixed frame, but do not recognize the importance of proper second-order wave drift forces. Furthermore, the implementation of convolution integrals for wave radiation forces is only strictly valid for ships with zero drift angle; for a ship maneuvering in waves, time-varying seakeeping quantities are actually affected by steady sway velocity and yaw-rate.

Unified theories have also been developed to include nonlinear wave excitation forces as in the work of Yen et al. (2010) and Subramanian and Beck (2015). The

implementation in Subramanian and Beck (2015) utilizes the MMG-type model of Son and Nomoto (1981) for the S-175 container ship. The MMG model provides hydrodynamic derivatives on the hull, rudder forces, and propulsion forces. The hydrodynamic derivatives related to linear added mass effects are replaced with hydrodynamic forces from a nonlinear desingularized Boundary Element Method (BEM). The potential flow formulation utilizes a body-exact desingularized strip theory for boundary conditions on the body. The linear free-surface conditions are also imposed using a desingularized formulation.

The second extension of the Abkowitz-style maneuvering model to include waves is the "Two-time-scale Method". The two-time scale method takes its name from the process used to separate the low-frequency maneuvering dynamics from the high-frequency wave-induced motions. The assumption that two different time scales govern the maneuvering and seakeeping motions provides a method to separate the dynamics into two separate systems of equations, a nonlinear system for the slowly-varying maneuvering motions and a linear six degree of freedom system for the seakeeping motions that vary at the wave encounter frequency. The first instance of a method like this was the work of Hirano et al. (1980), with the caveat that the author in that work did not solve the high-frequency seakeeping motion.

The work by Skejic and Faltinsen (2008) was one of the earliest efforts to compute updates to the second-order drift force concurrently in time with the temporal evolution of the low-frequency maneuvering equations. The updates are calculated using four different theories for computation of second-order wave force. The first three theories all require solution of the fluid boundary value problem and compute second-order mean drift forces as a postprocessing step. The evaluated theories are those of Faltinsen et al. (1981), Salvesen (1974), and Loukakis and Sclavounos (1978). The work in Faltinsen et al. (1981) also features an asymptotic theory for short wavelengths for Froude numbers less than 0.2.

Yasukawa and Nakayama (2009) use the two-time-scale method to simulate the S-175 container ship turning in waves and compare against experiments. While Yasukawa and Nakayama (2009) solve both the high-frequency and low-frequency problems to construct the total motions, the time-domain strip theory in their work does not calculate the second-order drift force in time. Instead, second-order drift force is precomputed using a momentum conservation method and tabulated for use as a look-up table during change of heading in the simulation. This work concluded that the two-time-scale method could roughly capture the turning characteristics of the S-175 in waves.

The two-time-scale method is further improved by Seo and Kim (2011) by introducing a time-domain BEM solution. Use of a time-domain Rankine panel method enables the proper treatment of ship motions in a slowly-turning frame of reference. Moreover, the computation of second-order wave force is computed using the instantaneous seakeeping motions which are impacted by the maneuvering motion. The distinction between this approach and the older works is that all prior attempts had either used frequency domain seakeeping methods or precomputed, tabulated measurements of second-order wave force.

Further improvements to seakeeping quantities of a ship turning at a drift angle are made by Zhang et al. (2017) and Lee and Kim (2020). Both of these studies investigate the use of a double-body basis flow and trailing vortex sheet to modify the basis flow. The modifications to the double-body potential ultimately impact the seakeeping prediction as the unsteady wave flow is affected by the steady basis flow.

The two-time-scale approach used in Cura-Hochbaum and Uharek (2016) and Uharek and Cura-Hochbaum (2018) is an Abkowitz-style model but with all coefficients derived using CFD. The approach used in these works simulates only the low-frequency maneuvering problem with hydrodynamic coefficients derived from virtual captive model tests. The mean wave loads are introduced through construction of a

wave-force model. The wave forces (and moments) are constructed from CFD simulations for a ship advancing at several different speeds across multiple wave headings and wave lengths. To build a robust enough model, a significant amount of computing resources is required. Although the seakeeping computations include radiation and diffraction effects, the wave-model's prediction is limited on the assumption of quasi-steady updates to forward speed, and the sway velocity and yaw rate are omitted from the seakeeping computations. Moreover, the presented wave-force model is intended for low-speed maneuvering when wave radiation and diffraction effects can be approximated as those on a fixed course.

The last category identified by the ITTC Maneuvering Committee is "Computational Methods". This category could be further split into potential-flow methods and CFD methods. However, potential flow has, to this date, been used almost exclusively for seakeeping prediction due to its limitations in predicting viscous phenomena which govern the horizontal plane maneuver. As such the potential flow methods straddle the line between computational methods and system-based methods because the potential methods tend to be used more often in conjunction with Abkowitz-style or MMG-type methods.

Within the last decade CFD computations for ships maneuvering in waves have begun to appear in the literature but are still scarce. The advantages that CFD offers are with its ability to model viscous fluid effects and nonlinear wave-body interaction within a single mathematical formulation. Works representative of the state-of-the-art application of CFD to combined simulation of maneuvering and seakeeping include Carrica et al. (2013) and Wang and Wan (2018). Both works feature usage of an overset mesh method to accommodate rotating propellers and moving rudders. The nonlinear free surface is captured in the work of Carrica et al. (2013) with a single-phase level-set method and in the work by Wang and Wan (2018) with a VOF method. The publication by Wang and Wan (2018) lists a run time of over one month on a

small computing cluster to simulate one turning circle in waves. The computational cost is considerable with CFD approaches, but the accuracy of the computation and insight into the fluid physics is what stands to be gained with the associated costs.

The hybrid formulation presented in this work is classified entirely within the computational methods region of Figure 1.1 and makes use of both CFD and a potential flow method. While the hybrid formulation demonstrated here uses a propeller model, the model is constructed purely from CFD. The following section proceeds to explain the gap in computational capability and what new capabilities the hybrid method offers.

1.2 Overview of Thesis: Objectives and Contributions

A primary goal for this thesis work is reduce the simulation costs associated with CFD approaches to solving maneuvering and seakeeping problems. The value behind developing more efficient algorithms is strongly tied to developments in computer processing power. Although Moore's law, which roughly states that computer processing power doubles every two years, has been the prevailing estimation of future computing power, advancements in microchip design are lagging the law. Thus, responsibility also resides with scientists and engineers to write efficient and robust algorithms.

In the context of this thesis work, the goal is to develop a computational framework to simulate the combined maneuvering and seakeeping response of a ship in a seaway. The proposed computational framework provides a modular and flexible approach to modeling the various physical phenomena involved in the case of a ship maneuvering in waves. The approach presented herein circumvents the need for constructing a mathematical model and the accompanying burden (experimental or computational) associated with generating the data to build the models. Instead, this framework solves the transient governing equations for the fluid and rigid body.

The importance of the modular aspect of the hybrid framework is stressed; it is

the key to obtaining both accuracy and efficiency. Each piece of the hybrid framework is selected for its strengths and efficiencies, as will be explained in Chapter II. A single-phase, incompressible RANS solution will be used to obtain viscous and pressure forces common to those acting on a ship maneuvering in calm water. The hybrid method removes all wave-modeling and computational costs from the CFD simulation and instead treats them with a potential flow BEM. The BEM solves the small amplitude wave-induced seakeeping motions and higher-order waves loads and is evolved in time concurrently with the CFD. A propeller model is used to provide propulsion forces. The overall structure of the hybrid method is outlined in Chapter II followed by a description of the numerics.

Following the overview of the hybrid computational framework, two test cases are presented to benchmark the performance of the hybrid method against high-fidelity numerical results generated with a nonlinear Volume-of-Fluid (VOF) method. The first test case is a study of the maneuvering characteristics of the Duisburg Test Case (DTC) hull form. The study first computes the seakeeping response of the DTC hull using the VOF method to ensure adequate resolution in the computational mesh before the costly turning circle maneuvers are computed. Next, the study computes the calm-water maneuvering response of the DTC hull using a simplified hybrid method and, for comparison, a nonlinear VOF method. The maneuver is made at an initial speed of 1.48 m/s ($Fn = 0.2$). Then the performance of DTC hull turning in waves is investigated by comparing computations made with the proposed hybrid method to high-fidelity VOF computations.

Chapter IV presents the second test case for the combined seakeeping and maneuvering performance of the KCS hull in regular waves. Seakeeping and added resistance computations are first computed using the VOF method to isolate the seakeeping problem and verify adequate grid resolution. Next, calm-water turning circles using both the hybrid approach and VOF are predicted for the KCS hull at an

initial speed of 0.86 m/s ($Fn = 0.157$). Finally, the performance of KCS hull turning in waves is investigated by comparing computations made with the proposed hybrid method to high-fidelity VOF computations.

CHAPTER II

Theory, Numerical Methods, and Implementation

2.1 Introduction

The hybrid method for combined simulation of maneuvering and seakeeping of a vessel is a formulation developed in this work that allows for an efficient and modular approach to modeling the forces and dynamics of a ship maneuvering in a seaway. The method is labeled as a "hybrid" method because it offers flexibility in how the various forces are modeled while providing a framework to consolidate forces and moments from each model into a total hydrodynamic force vector.

The application of the hybrid method in this work employs multiple numerical methods including single-phase incompressible Reynolds-averaged Navier-Stokes (RANS) simulations, a Boundary Element Method (BEM), and surrogate modeling of propulsion forces (including the side force). The RANS simulations are computed on a computational mesh that simplifies the free surface to the calm-water plane, thereby removing all wave modeling from the CFD. The RANS computations contribute the viscous and pressure forces common to a ship maneuvering in calm water. The BEM is utilized to model small amplitude radiation and diffraction wave loads the ship experiences while maneuvering in a seaway. The ship is propelled by a propulsion model that allows for the removal of the propeller from the CFD discretization.

Usage of the BEM and propeller model are critical pieces of the hybrid formulation

that contribute towards the reduced computational cost. The BEM models all wave effects, thereby relaxing the demanding spatial and temporal requirements otherwise necessary to propagate a numerical wave using the VOF method. The propeller model allows for removal of a discrete propeller from the CFD and the strict time step requirements to resolve the propeller transient flow features. The following sections will introduce each method in detail, beginning with the overall structure of the hybrid formulation.

2.2 Hybrid Method Formulation

The hybrid method makes use of a two-time-scale theory originally formulated for the design of dynamically positioned or moored floating structures (Triantafyllou, 1982). The two-time-scale theory provides an alternative way to add two time-varying signals. Consider a total signal, $r_T(t)$, composed of two signals, one signal that varies rapidly, $r_f(t)$, and another signal that varies slowly, $r_s(t)$. The amplitude of the slowly varying signal is considered to be $\mathcal{O}(1)$ and the ratio of amplitudes $r_f/r_s = \epsilon$ ($\epsilon \ll 1$). The total signal is represented by the linear superposition of the two signals given in Equation 2.1.

$$r_T(t) = \epsilon r_f(t) + r_s(t) \tag{2.1}$$

An equivalent way of representing the slowly varying signal is to introduce a compressed time-scale, $\tau = \epsilon t$. The total signal, with the slowly varying part written in the compressed time-scale, appears as in Equation 2.2.

$$r_T(t) = \epsilon r_f(t) + r_s(\epsilon t) \tag{2.2}$$

Returning the discussion to ship dynamics, the total signal r_T is interpreted as a vector of displacements of a ship's center of gravity from and Earth-fixed origin. The Earth-fixed frame is an inertial frame and the translation of the ship center of gravity

is governed by Newton's second law of motion. The ship is forced by a first order (in ϵ) force, $\mathbf{F}_1(t)$, that varies at the wave encounter frequency and a second order force, $\mathbf{F}_2(\tau)$, that varies on a time scale related to the overall maneuver and is represented as a function of the compressed time scale. When the decomposition (Equation 2.1) is inserted into Newton's second law the result is Equation 2.3.

$$m\frac{\partial^2 \mathbf{r}_T}{\partial t^2} = m\left(\epsilon\frac{\partial^2 \mathbf{r}_f}{\partial t^2} + \epsilon^2\frac{\partial^2 \mathbf{r}_s}{\partial \tau^2}\right) = \epsilon\mathbf{F}_1(t) + \epsilon^2\mathbf{F}_2(\tau) \tag{2.3}$$

Equation 2.3 leads to a simple and natural decoupling of slowly maneuvering motions from the rapidly varying wave-induced seakeeping motions through the parameter ϵ. Furthermore, the decomposition in Equation 2.3 does not preclude nonlinear interactions between the large amplitude maneuvering response and the small amplitude seakeeping response. The same reasoning and decomposition is used for the change in ship heading (yaw) in the horizontal plane relative to the Earth-fixed frame.

The large amplitude, slowly varying dynamics are modeled in this work through a three degree of freedom system governing the surge, sway, and yaw (horizontal plane) motions. The small amplitude, rapidly varying seakeeping dynamics are modeled through a six degree of freedom linearized system of equations. The wave-induced displacements and rotations are conveniently formulated in a moving coordinate system, which provides the basis for the linearization. The systems of equations governing the dynamics will be outlined in detail including the approaches to predict the hydrodynamic force vectors and separate them into the two segregated time-scale problems.

Multiple frames of reference are utilized in this work and are now outlined before establishing the equations governing the dynamics of the vessel. Figure 2.1 depicts the kinematic description used to define the position of the center of gravity of the ship and the ship's orientation. The primary reference frame is an Earth-fixed frame

which is considered as an inertial frame of reference. Coordinates in the Earth-fixed frame are measured with vector $\mathbf{X}_E$ and velocities written in the Earth-fixed frame are given by $\dot{\mathbf{X}}_E$. The second (intermediate) reference frame, the maneuvering frame, has origin O_M located at the ship's longitudinal center of gravity at its undisturbed position (no wave induced motion) in the horizontal plane. The horizontal plane displacement of O_M is measured in Earth-fixed coordinates with the vector $\mathbf{X}_E$. The maneuvering frame is also permitted to rotate about the Earth-fixed vertical axis and the orientation of the maneuvering frame relative to the Earth-fixed frame is measured with yaw angle Ψ. The rate of heading change (yaw rate) is denoted $\dot{\Psi}$. In the context of the two-time-scale assumption, $\mathbf{X}_E$ and Ψ represent the large-amplitude, slowly varying part of the total vessel response.

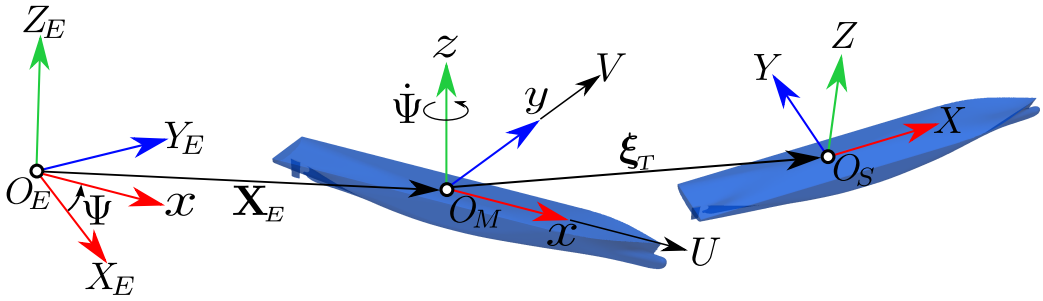

Figure 2.1: Coordinate systems used in the hybrid method

Finally, the rightmost frame in Figure 2.1 is a body-fixed frame with origin O_S that moves relative to O_M by vector $\boldsymbol{\xi}_T$. The displacements $\boldsymbol{\xi}_T$ and rotations $\boldsymbol{\xi}_R$ originate due to small-amplitude wave forcing which occurs at the wave encounter frequency. In the context of the two-time-scale assumption, these displacements represent the small-amplitude, rapidly varying part of the signal.

The ensuing sections give a detailed discussion of the degrees of freedom in the kinematic description of the vessel in the hybrid method. The equations governing the rigid body dynamics for each degree of freedom are stated. Special effort is invested in describing each component of the hydrodynamic force, the methods used to compute each force, and the aggregation of forces and subsequent distribution to

each time-scale problem.

To begin, the nonlinear equations of rigid body dynamics are developed as they are a generalization of the systems governing the degrees of freedom within the hybrid method. Further, the case studies presented in Chapters III-IV compare the hybrid method results to computations made using a nonlinear VOF method. The VOF method features not only a nonlinear formulation for the fluid but also fully nonlinear body motion which is tightly coupled to the fluid solution. The equations of motion for the slowly varying maneuvering motion and, separately, the rapidly varying, small-amplitude wave-induced motion will be developed as specializations of the nonlinear six degree of freedom equations of motion.

2.2.1 Six Degree of Freedom Nonlinear Equations of Motion

The ship is treated as a rigid body and the translational motion of its center of gravity is governed by Newton's second law of motion. The origin of the maneuvering coordinate system, O_M, is placed at the ship center of gravity and permitted to translate relative to the Earth-fixed origin, O_E, with displacement, $\vec{X}_E$, shown in Figure 2.2.

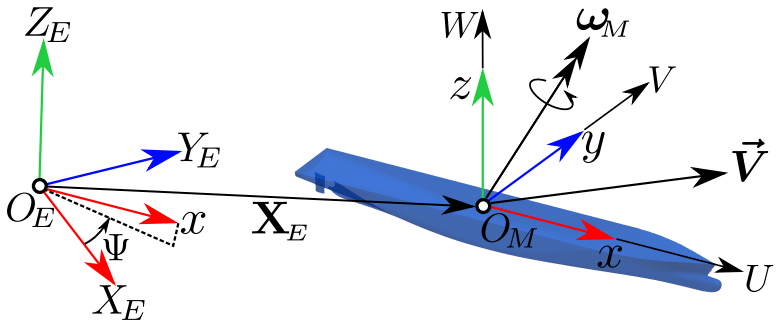

Figure 2.2: Coordinate systems used in formulating the nonlinear six degree of freedom equations of motion

The solution of the three translational equations is accomplished in the inertial Earth-fixed frame where the equations are uncoupled from the body's rotational degrees of freedom. If the forces and moments are computed in the Earth-fixed frame

and the motion of the center of gravity of the ship is evolved in the Earth-fixed frame, the governing equations take the familiar form of Newton's second law of motion.

The equations governing the rotation of the body are formed by taking time-derivative of angular momentum equal to the sum of the moments about a point fixed within the body. The angular momentum of the body is conveniently defined in the body-fixed frame about the center of gravity of the body and the body angular velocity, $\boldsymbol{\omega}_M$, is described in coordinates $O_M(x, y, z)$. With this choice of reference frame and formulating the equations about the center of gravity, the rotational inertia tensor, $\overline{\overline{\mathcal{I}}}$, remains constant in time. The resulting equations governing the rotational motion of the body are Euler's equations of rotational motion.

Many parameterizations exist for tracking the orientation of the body-fixed frame with respect to the Earth-fixed frame. In this work, a 3-2-1 Euler angle rotation sequence is adopted. The orientation of the ship is tracked by first rotating a yaw angle, Ψ, about the Earth-fixed Z_E-axis followed by a pitch, Θ, about an intermediate y-axis, and lastly a roll, Φ, about the body-fixed X_M-axis. Together, Newton's second law and Euler's rotational equations uniquely define the body's motion and orientation and are shown in Equation 2.4.

$$\begin{aligned} m\ddot{\mathbf{X}}_E &= \mathbf{F}_E \\ \overline{\overline{\mathcal{I}}}\dot{\boldsymbol{\omega}}_M &= \mathbf{M}_M - \boldsymbol{\omega}_M \times \left(\overline{\overline{\mathcal{I}}}\boldsymbol{\omega}_M\right) \end{aligned} \tag{2.4}$$

The total force vector, $\mathbf{F}_E$, and the total moment vector, $\mathbf{M}_M$, act as forcing on right-hand-side of the equations of motion. The total force (moment) is composed of the total hydrodynamic force and the propulsion force which is supplied from the propeller model (Knight and Maki, 2020) described in Section 2.5. In the VOF method, described in Section 2.3, the total hydrodynamic force is derived from integration of the viscous stresses and pressure over the hull and rudder surfaces; viscous forces and wave forces are implicitly captured. Moreover, the maneuvering motions are indistin-

guishable from the seakeeping motions in contrast to the kinematic description used for the hybrid method (Figure 2.1).

The rigid body dynamics and hydrodynamics are solved in a tightly-coupled algorithm, necessary for modeling a ship operating in a dense fluid with added mass forces. The added mass and buoyancy forces tend to cause the system in Equation 2.4 to be numerically stiff. At each time step, the fluid-structure coupling is enforced by sequentially (and iteratively) solving the rigid-body dynamics followed by the fluid. The rigid-body dynamics are first solved using the prevailing values of hydrodynamic force. The mesh motion in the CFD is updated and the fluid equations are then solved, yielding updated hydrodynamic forces. The algorithm then iterates within one time step to solve again for the dynamics using updated hydrodynamic forces.

To enhance the stability of this segregated fluid-structure coupling, inertial under-relaxation is introduced into the equations governing the rigid-body dynamics (Piro, 2013, p. 29). Inertial under-relaxation factors m_a and $\overline{\overline{\mathcal{I}}}_a$ are added to the translational and rotational equations respectively. In this work the mass and rotational inertia factors are taken as their physical values, i.e. $m_a = m$ and $\overline{\overline{\mathcal{I}}}_a = \overline{\overline{\mathcal{I}}}$. The inertial under-relaxation operates by boosting the diagonal of the system proportionally to the under-relaxation factor. The under-relaxation acting the right-hand-side of the system is updated after the solution to the system, and thus lags the instantaneous acceleration in iteration index, m. Upon convergence, $\ddot{\mathbf{X}}_E^{m\text{-}1} = \ddot{\mathbf{X}}_E^m$ and $\dot{\boldsymbol{\omega}}_M^{m\text{-}1} = \dot{\boldsymbol{\omega}}_M^m$. In relation to the solution of the fluid, the equations of motion are solved once per every fluid solve and the iteration index, m, is synonymous with a PISO loop which is familiar to any CFD solver enforcing pressure-velocity coupling through a segregated algorithm. The under-relaxed equations of motion are given in Equation 2.5.

$$\begin{aligned}
(m + m_a)\, \ddot{\mathbf{X}}_E^m &= \mathbf{F}_E + m_a \ddot{\mathbf{X}}_E^{m\text{-}1} \\
\left(\overline{\overline{\mathcal{I}}} + \overline{\overline{\mathcal{I}}}_a\right) \dot{\boldsymbol{\omega}}_M^m &= \mathbf{M}_M - \boldsymbol{\omega}_M^{m\text{-}1} \times \left(\overline{\overline{\mathcal{I}}} \boldsymbol{\omega}_M^{m\text{-}1}\right) + \overline{\overline{\mathcal{I}}}_a \dot{\boldsymbol{\omega}}_M^{m\text{-}1}
\end{aligned} \tag{2.5}$$

The system of Equations 2.5 is evolved in time using an implicit second-order backward difference scheme. The solution to the rotational equations in Equation 2.5 yields an angular acceleration, $\dot{\boldsymbol{\omega}}_M$, which must be integrated once for updated angular velocities and then integrated again for updated orientation of the vessel. However, the orientation update is accomplished by integrating the Euler angle rates native to the parameterization that is selected. The Euler angle rates are obtained through the solution of Equation 2.7 (Greenwood, 2003, p. 144) and integrated again with the backwards difference formula to yield the new orientation.

$$\boldsymbol{\omega}_M \equiv \begin{Bmatrix} p \\ q \\ r \end{Bmatrix} = \begin{bmatrix} 1 & 0 & -s(\Theta) \\ 0 & c(\Phi) & s(\Phi)c(\Theta) \\ 0 & -s(\Phi) & c(\Phi)c(\Theta) \end{bmatrix} \begin{Bmatrix} \dot{\Phi} \\ \dot{\Theta} \\ \dot{\Psi} \end{Bmatrix} \tag{2.6}$$

$$\begin{Bmatrix} \dot{\Phi} \\ \dot{\Theta} \\ \dot{\Psi} \end{Bmatrix} = \begin{bmatrix} 1 & 0 & -s(\Theta) \\ 0 & c(\Phi) & s(\Phi)c(\Theta) \\ 0 & -s(\Phi) & c(\Phi)c(\Theta) \end{bmatrix}^{-1} \begin{Bmatrix} p \\ q \\ r \end{Bmatrix} \tag{2.7}$$

The equations of motion governing the maneuvering degrees of freedom and (separately) the equations governing the wave-induced seakeeping motions are now derived as specializations of the fully nonlinear equations of motion (Equation 2.4).

2.2.2 Three Degree of Freedom Maneuvering Equations of Motion

The equations of motion for the slowly varying time-scale govern the horizontal plane maneuvering degrees of freedom. The hybrid method restricts the maneuver, which has large length and time scales relative to wave-induced motions, to the horizontal plane. The ship's center of gravity is tracked in the horizontal plane by $\mathbf{X}_E = (X_E, Y_E, 0)$ and shown in Figure 2.3.

The maneuvering equations in this work do not model the pitch and roll degrees

of freedom (pitch and roll are captured by seakeeping equations of motion), an assumption that is evaluated in subsequent sections of this work. As a result, the maneuvering and Earth-fixed coordinate systems share a common vertical axis and the orientation of the ship is completely described by its heading, Ψ.

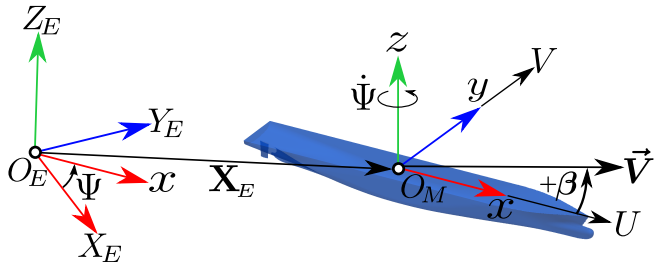

Figure 2.3: Coordinate systems used in the three degree of freedom maneuvering equations of motion

Under these simplifying assumptions, the resulting equations of motion for maneuvering trajectory reduce to a three degree of freedom system, Equation 2.8, describing the ship's position and orientation in the horizontal plane.

$$\begin{aligned} m\ddot{\mathbf{X}}_E &= \mathbf{F}_{DB} + \mathbf{F}_P + \overline{\mathbf{F}^{(2)}} + \mathbf{R} \\ I_z\ddot{\Psi} &= M_{DB_z} + M_{P_z} + \overline{M_z^{(2)}} \end{aligned} \tag{2.8}$$

These assumptions facilitate the use of a single-phase RANS solution, which is a key factor in reducing the cost of simulations in waves. The three degree of freedom maneuvering equations are forced by the total hydrodynamic force (and moment) from the viscous double-body RANS solution, $\mathbf{F}_{DB}$, the propulsion force, $\mathbf{F}_P$, the first-order steady wave resistance from the BEM, $\mathbf{R}$, and the time-averaged second-order wave force from the BEM, $\overline{\mathbf{F}^{(2)}}$, for simulations in waves. This force decomposition neglects the component of the hydrodynamic moment arising from the steady first-order wave for a ship at a drift angle. The total moment is assumed to be composed of the the double-body RANS stresses acting on the hull and rudder, M_{DB_z}, the propeller moment which arises from oblique inflow into the propeller, M_{P_z}, and the time-averaged second-order wave drift moment, $\overline{M_z^{(2)}}$.

The single-phase RANS CFD computation solves a viscous double-body (DB) flow where the fluid is bounded at the calm-water level; this amounts to using a symmetry plane boundary condition on $z = 0$ for all field quantities in the CFD. This simplification is equivalent to a zero Froude number approximation to the free surface and greatly reduces mesh resolution requirements in the far-field necessary for accurate propagation of incident waves using the VOF method. The forces from the viscous double-body RANS solution are computed as integrals of pressure and viscous stress over the exact horizontal plane position of the hull but only below the calm-water plane.

The propulsion force, $\mathbf{F}_P$, and propulsion moment, M_{DB_z}, are predicted by a surrogate model that was trained on CFD data that was generated before the maneuvering simulations. A brief description of the propeller models (Knight and Maki, 2020) used in this work is provided in Section 2.5.

The wave resistance is included as steady forcing to the maneuvering three degree of freedom system due to the double-body approximation used in the RANS computations. In this work, the wave resistance is precomputed using a linearized BEM for each ship model at zero drift angle and at the initial speed before each maneuver is executed. The time dependent wave resistance is linearly interpolated between the computed value and zero wave resistance at zero speed. The wave resistance acts only in the ship-fixed x-direction but is transformed into the Earth-fixed frame to populate the right-hand-side of Equation 2.8. Appendix B presents a study into the validity of neglecting the steady wave sway force and yaw moment for a ship advancing at constant speed but nonzero drift angle.

The final remaining component of the total low-frequency maneuvering force vector is the contribution from higher-order wave loads. The wave forces computed in this work arise from second-order terms in a perturbation expansion of the seakeeping Boundary Value Problem (BVP)'s. To be strictly compatible with the separation

of time-scales presented in Section 2.2, the second-order wave loads should not contain fluctuations at the wave-encounter frequency. The time-averaging procedure for the second-order wave loads is described in Section 2.4.2. However, in practice, the averaging procedure is shown to be unnecessary as is demonstrated in Section 3.4.

The maneuvering equations of motion are presented as a specialization of the more general nonlinear six degree of freedom set of motions. Each component of the total hydrodynamic force vector is described. Now, before presenting the numerics behind the tools used to derive each component of the total hydrodynamic force, the high-frequency seakeeping equations are presented.

2.2.3 Six Degree of Freedom Linear Seakeeping Equations of Motion

The seakeeping equations of motion represent the small-amplitude rapidly varying problem within the two-time-scale assumption. This assumption is fitting given that length scales governing the overall maneuver are on the order of ship length, L, whereas seakeeping motions in small waves typically are much smaller than L. Moreover, a time scale for the overall maneuver, a turning circle for example, can be estimated from a length scale, L, divided by a velocity scale, say the forward speed, U. The time scale in the seakeeping problem is the wave encounter period, T_e. Practical considerations generally yield $L/U \gg T_e$.

The linear six degree of freedom equations governing the small-amplitude, wave-induced motions are derived readily from the linearization of Equation 2.4. The six degree of freedom seakeeping motions are computed in maneuvering frame $O_M(x, y, z)$. If the translational equations in Equation 2.4 are transformed into the body-fixed axes, velocities are assumed to be $\mathcal{O}(\epsilon)$, and terms $\mathcal{O}(\epsilon^2)$ and greater are discarded, Equation 2.9 results.

$$\overline{\overline{M}}\ddot{\boldsymbol{\xi}} = \mathbf{F}_1 \tag{2.9}$$

Under the linearization, the nomenclature that is adopted here is $\dot{U}, \dot{V}, \dot{W} \rightarrow$

$\dot{\xi}_1, \dot{\xi}_2, \dot{\xi}_3$ and $\dot{\Phi}, \dot{\Theta}, \dot{\Psi} \rightarrow \dot{\xi}_4, \dot{\xi}_5, \dot{\xi}_6$, and the linear state vector, $\boldsymbol{\xi}$, is defined as $\boldsymbol{\xi} \equiv (\xi_1, \xi_2, \xi_3, \xi_4, \xi_5, \xi_6)$. Moreover, after the linearization, the distinction between Euler angle sequence becomes ambiguous and unnecessary. The linear six degree of freedom system is forced by the first order hydrodynamic force, $\mathbf{F}_1$, which consists of hydrostatic force, Froude-Krylov force, and the wave radiation and diffraction forces, all computed using a BEM potential flow solution.

2.2.4 Coupling of Maneuvering and Seakeeping Problems

The formulation of the maneuvering dynamics is outlined in Section 2.2.2 and the formulation for the small-amplitude seakeeping motions, which are linearized about the exact horizontal plane position of the ship, is given in Section 2.2.3. This section outlines the algorithm design and coupling strategy for the maneuvering and seakeeping problems.

The two major pieces of machinery within this modular framework are the RANS solver and the Boundary Element Method (BEM). The open source C++ toolkit OpenFOAM (version 2.4.0) is selected as the CFD solver in this work. A high-order Non-Uniform Rational B-Spline (NURBS)-based time-domain BEM solver, named Aegir, is selected to solve the seakeeping motions and second-order wave forces. The equation of motion solver for the horizontal plane maneuvering degrees of freedom is incorporated within the RANS solver and the linear six degree of freedom seakeeping motions solver is grouped with the BEM. The horizontal plane maneuvering equations of motion require a component from the second-order wave forces as shown in Equation 2.8. The BEM solves several BVP's which are formulated in the maneuvering frame and require information from the maneuvering state vector. Thus, several packets of information must be communicated from one program to another. Figure 2.4 depicts the high-level structure of the overall algorithm along with the information passed between programs.

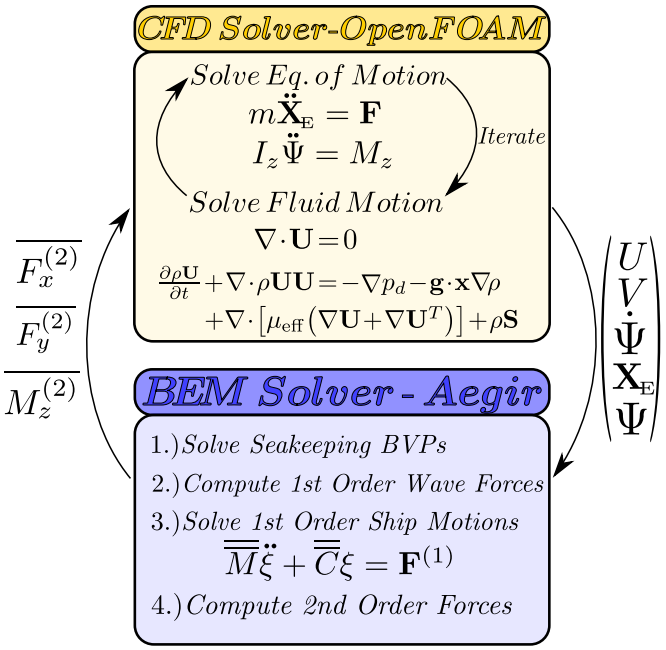

Figure 2.4: Algorithm for coupling of maneuvering and seakeeping problems

The algorithm in Figure 2.4 displays the state vector being provided by the RANS CFD solver (OpenFOAM) to the BEM solver (Aegir). The horizontal plane velocities and yaw rate factor into each BVP solved within Aegir. The position vector of the ship's center of gravity and the velocities and yaw rate are utilized by Aegir to transform the analytic incident wave into the maneuvering frame. Aegir solves for the first-order BVP's for the first-order potentials, computes the first-order wave forces, and solves for the linear six degree of freedom seakeeping motions. As a postprocessing step, Aegir computes the second-order forces which are functions of first-order quantities. The second-order wave forces are time-averaged and passed from Aegir to the equation of motion solver within OpenFOAM.

Currently, the BEM solver is written in Fortran while the CFD solver is written in C++. The exchange of information and time-stepping is orchestrated by a driver program written in python. The CFD computations have a stricter time step requirement for the stability and accuracy of the coupled rigid-body and fluid system of equations. As such, Aegir is called one time every four to sixteen time steps within

OpenFOAM. Because the equations must be evolved concurrently, this sets the required ratio between a time step in Aegir and a time step in OpenFOAM. At this stage of the research, constant time steps are utilized to facilitate the benchmarking of this method, though adaptive time stepping could in principle be implemented.

This concludes the introduction to the hybrid method. The governing equations for the rigid-body ship dynamics have been derived and the various components of the hydrodynamic force vectors have been described. The following sections present the theory and numerics behind the computation of each of the force components. The RANS and VOF numerics are presented first. Next, the BEM solver is described followed by Section 2.4.2 devoted to describing computation of the second-order wave loads within the BEM. Lastly, the surrogate propeller model is outlined and the rudder force computation is described.

2.3 Incompressible Reynolds-averaged Navier-Stokes Solver

The physical processes governing multi-phase flow in ship hydrodynamics applications are modeled by the incompressible Navier-Stokes equations. In this work the air and water phases are primarily separated as opposed to interpenetrating (dispersed flow), and thus a single-field representation is utilized to model the two-phase flow. The single-field representation for a two-phase, incompressible, immiscible fluid consists of a conservation equation for mass and a conservation equation for momentum. This work utilizes a Reynolds-averaging process where all field variables are split into a mean and fluctuating component, i.e. Reynolds decomposition, and then ensemble averaged. Reynolds stress closure is accomplished through use of the Boussinesq eddy viscosity hypothesis, where the turbulent stresses (modeled through the turbulent eddy viscosity, μ_t) are assumed proportional to the mean strain rate tensor. The resulting Reynolds-averaged Navier-Stokes (RANS) equations are shown

in differential form in Equations 2.10-2.11.

$$\frac{\partial \rho}{\partial t} + \nabla \cdot \rho \mathbf{U} \quad = 0 \tag{2.10}$$

$$\frac{\partial \rho \mathbf{U}}{\partial t} + \nabla \cdot \rho \mathbf{U}\mathbf{U} = -\nabla p + \nabla \cdot \left[\mu_{\text{eff}} \left(\nabla \mathbf{U} + \nabla \mathbf{U}^T\right)\right] + \rho \mathbf{g} + \rho \mathbf{S} \tag{2.11}$$

In Equation 2.10, ρ is the fluid density, $\mathbf{U}$ is the ensemble-averaged velocity field, p is the ensemble-averaged pressure, μ_{eff} is the sum of dynamic viscosity and turbulent eddy viscosity, $\mathbf{g}$ is the acceleration due to gravity vector, and $\mathbf{S}$ is a generic source term vector.

In this work, the turbulent eddy viscosity, μ_t, is modeled using the Spalart-Allmaras one-equation eddy viscosity model (Spalart and Allmaras, 1994). The implementation used in this work follows the baseline Spalart-Allmaras model with modifications to the $\tilde{S}$ term and the $f_{\nu 2}$ term following the reasoning and implementation found in Ashford (1996). The form of the transport equation for variable $\tilde{\nu} = \nu_t / f_{\nu 1}$ used in this work is given in Equation 2.12.

$$\frac{\partial \tilde{\nu}}{\partial t} + \nabla \cdot \mathbf{U}\tilde{\nu} = \frac{1}{\sigma} \nabla \cdot \left((\nu + \tilde{\nu}) \nabla \tilde{\nu} + C_{b2} |\nabla \tilde{\nu}|^2\right) + C_{b1} \tilde{S} \tilde{\nu} - C_{w1} f_w \left(\frac{\tilde{\nu}}{d}\right)^2$$

$$\chi \equiv \frac{\tilde{\nu}}{\nu}$$

$$f_{\nu 1} = \frac{\chi^3}{\chi^3 + C_{\nu 1}^3}, \quad f_{\nu 2} = \left(1 + \frac{\chi}{C_{\nu 2}}\right)^{-3}, \quad f_{\nu 3} = \frac{1 + \chi f_{\nu 1}}{\chi}$$

$$\tilde{S} = S f_{\nu 3} + \frac{\tilde{\nu}}{\kappa^2 d^2} f_{\nu 2}, \quad S = \sqrt{2\, \overline{\overline{\Omega}} : \overline{\overline{\Omega}}} \tag{2.12}$$

Transport Equation 2.12 includes the familiar temporal and convection terms on the left hand side and features three expressions on the right hand side that model diffusion of $\tilde{\nu}$, production of $\tilde{\nu}$, and destruction of $\tilde{\nu}$. The constants C_{b1}, C_{b2}, $C_{\nu 1}$, $C_{\nu 2}$, C_{w1}, σ, and the functional form of f_w are consistent with those reported in Spalart and Allmaras (1994). It should be noted that for all two-phase simulations in this

work, the form of the Spalart-Allmaras is maintained and the turbulent (dynamic) eddy viscosity is calculated as $\mu_t = \rho\nu_t$.

The Navier-Stokes Equations 2.10-2.11 are already formulated to handle variable density, incompressible flows ($\rho = \rho(\mathbf{x}, t), D\rho/Dt = 0$), but require an extension to capture the fluid interface. Multi-phase modeling is accomplished using a VOF (Hirt and Nichols, 1981) approach where scalar variables of density and molecular viscosity are described by mixture equations and vary in space and time according to the phase-fraction variable, $\alpha(\vec{x}, t)$. The phase fraction is defined in Equation 2.13.

$$\alpha(\mathbf{x}, t) = \begin{cases} 1, & \text{if } \mathbf{x} \text{ in water.} \\ 0 < \alpha < 1, & \text{if } \mathbf{x} \text{ in interface region.} \\ 0, & \text{if } \mathbf{x} \text{ in air.} \end{cases} \tag{2.13}$$

The mixture equations for density and molecular viscosity are written as a function of the phase-fraction. Accordingly, this formulation solves a transport equation for α and computation of ρ and μ follows in a straightforward manner as in Equation 2.14.

$$\begin{aligned} \rho(\mathbf{x}, t) &= \rho_{\text{water}}\alpha(\mathbf{x}, t) + \rho_{\text{air}}(1 - \alpha(\mathbf{x}, t)) \\ \mu(\mathbf{x}, t) &= \mu_{\text{water}}\alpha(\mathbf{x}, t) + \mu_{\text{air}}(1 - \alpha(\mathbf{x}, t)) \end{aligned} \tag{2.14}$$

The transport equation for the phase-fraction is derived by inserting the mixture description of density in Equation 2.14 into the conservation of mass equation (Equation 2.10), with the result shown in Equation 2.15. The multi-phase family of solvers used in this work features an extra term, appearing as the third term in Equation 2.15. The compression velocity, $\mathbf{U}_r$, in the phase-fraction equation acts locally and normal to the two-phase fluid interface. The compression velocity, $\mathbf{U}_r$, though introducing fictitious velocity local to the interface, serves the purpose of preventing excessive diffusion of the air-water interface by retaining sharpness in the gradient

of α.

$$\frac{\partial \alpha}{\partial t} + \nabla \cdot \mathbf{U}\alpha + \nabla \cdot (\mathbf{U}_r \alpha(1-\alpha)) = 0 \tag{2.15}$$

Equation 2.15 is solved as a convection equation for the phase fraction. If the the densities are identical, the governing equations reduce to the single phase, incompressible, Navier-Stokes Equations. The hybrid method formulation detailed in this work uses single-phase RANS, removing all wave modeling from the CFD and instead modeling wave effects with a linear time-domain BEM.

The Open Source C++ tool-kit called OpenFOAM (Field Operation and Manipulation) version 2.4.0 is utilized in this work. OpenFOAM is a collection of libraries created for computational solution of continuum mechanics problems. The Finite Volume Method (FVM) is used for spatial discretization of the RANS equations in this work. A second-order accurate FVM method is formulated where cell-face values are reconstructed from field quantities that are permitted to vary linearly within arbitrary polyhedral finite volumes.

To describe the numerical schemes used in this work, it is adequate to inspect a generic scalar transport equation. The integral form of a generic transport equation for one discrete finite volume, V_P, is given in Equation 2.16. A generic transport equation such as Equation 2.16 is a conservation law for conserved quantity $\rho\phi$ where temporal evolution of the conserved quantity is balanced by convective, diffusive, and source/sink processes.

$$\int_t^{t+\Delta t} \left[\int_{V_P} \frac{\partial(\rho\phi)}{\partial t} dV + \int_{V_P} \nabla \cdot (\rho \mathbf{U}\phi)\, dV \right] dt = \int_t^{t+\Delta t} \left[\int_{V_P} \nabla \cdot \left(\rho \Gamma^{\phi} \nabla \phi\right) dV + \int_{V_P} \mathbf{S}^{\phi} dV \right] dt \tag{2.16}$$

The discretization schemes used for each term will be described in the following order: the convection term, the diffusion term, the source term, and the transient term.

2.3.1 Convection Term Discretization

The convection term is discretized by applying Gauss' theorem to transform the volume integral over a finite volume, V_P, to a sum of fluxes over the bounding cell faces, each with area vector $\mathbf{S}_f$ and face area centroid $\mathbf{x}_f$. The discrete convection operator is given in Equation 2.17, where the first line of Equation 2.17 is exact and the following two equalities are valid given a second-order description of ϕ.

$$\begin{aligned}\int_{V_P} \nabla \cdot (\rho \mathbf{U}\phi)\, dV &= \sum_f \int_{\partial V_P} (\rho \mathbf{U}\phi) \cdot d\mathbf{S} \\ &\cong \sum_f (\rho \mathbf{U}\phi)_f \cdot \mathbf{S}_f \\ &\cong \sum_f \left(\mathbf{S}_f \cdot (\rho \mathbf{U})_f\right) \phi_f\end{aligned} \tag{2.17}$$

In the Navier-Stokes equations, the scalar quantity ϕ is a component of fluid velocity, creating a nonlinear system of equations in $\mathbf{U}$. OpenFOAM addresses the nonlinear convection term by lagging the mass flux, $\left(\mathbf{S}_f \cdot (\rho \mathbf{U})_f\right)$, and iterating one or more times over a single time step, i.e. a Picard iteration approach.

Equation 2.17 also requires interpolation of the scalar quantity ϕ to the face centroid. The methods for approximating ϕ at a face area centroid have occupied researchers for the last 50 years and remain an active research area. The principal challenge in obtaining the face centroid value for the discrete convection operator in hyperbolic equations is stated in Godunov's order barrier theorem (Godunov, 1959) which proved that linear schemes can be at most first-order accurate while remaining monotone solutions.

A way to circumvent this strict limitation is to introduce nonlinear convection differencing schemes. Several early instances of this technique are found in the works by van Leer (1974), van Leer (1979), and in the Flux Corrected Transport (FCT) method of Boris and Book (1973) - a method which has direct applicability to the

solution of Equation 2.15 and will be subsequently discussed. Here, it suffices to say that the FCT method and high-resolution convection schemes share the same core idea, that is, the concept of blending a first order monotone upwind flux with a limited (nonlinear) portion of a higher-order flux. The flux or slope limiter, which is the nonlinear blending function, must be chosen such that existing extrema within the solution remain bounded.

The notion of solution boundedness has two popular approaches, namely the Convection Boundedness Criterion (CBC) of Gaskell and Lau (Gaskell and Lau, 1988) or the alternative Total Variation Diminishing property defined by Harten (1983). The discussion of limiters in OpenFOAM will be revisited in Secion 2.3.5 in the context of solving the hyperbolic equation for the phase fraction. An extensive exposition on the design of high-resolution convection schemes (using the concepts of the CBC and TVD property) can be found in Waterson and Deconinck (2007) and Sweby (1984). The reader is directed to these resources for theory on limiters and the TVD property.

The convection term in the momentum conservation equation (2.11) is discretized using Equation 2.17 and the face-value interpolation is accomplished using a linear upwind second-order scheme, also called Second Order Upwind (SOU). The face-value interpolation using the linear upwind scheme is given in Equation 2.18 (Moukalled et al., 2016, p. 409).

$$\phi_f = \phi_P + \left(2\nabla\phi_P - \nabla\phi_f\right) \cdot \mathbf{d}_{Pf} \tag{2.18}$$

The linear upwind scheme is a second-order, upwind biased scheme. In Equation 2.18 cell P is the upwind cell and the scheme is recognized as the first-order upwind scheme plus a second-order correction. The second-order correction incorporates information from the downwind cell through the cell-center gradient, $\nabla\phi_P$, and the gradient at the downwind face, $\nabla\phi_f$; $\mathbf{d}_{Pf}$ is the vector from the upwind cell center at $\mathbf{x}_P$ to the downwind face center (see Figure 2.5). Diagonal dominance of the linear system of equations is aided by treating the second-order correction part of

Equation 2.18 with the deferred correction approach for implicit methods as proposed by Khosla and Rubin (1974).

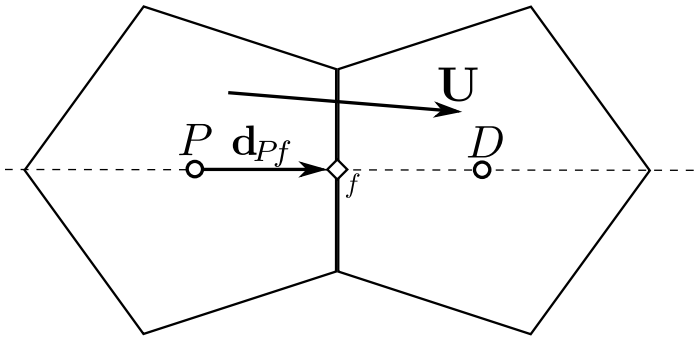

Figure 2.5: Convection discretization

The linear upwind scheme is not strictly bounded, and so the cell-centered gradient is limited in this work to prevent over- or under-shoots when interpolating to the face centroid. The gradients for all quantities are computed using the Green-Gauss gradient with exception of the phase fraction, which utilizes a second-order least squares gradient. The upwind scheme, while only first-order accurate, is monotone (bounded) and is used in discretization of the convection term for $\tilde{\nu}$ in Equation 2.12. Discretization of the convection term for the phase fraction is described in Section 2.3.5.

2.3.2 Diffusion Term Discretization

The treatment of the diffusive flux begins with use of the divergence theorem to transform integrals over the volume of polyhedral cell P into fluxes across the bounding faces as in Equation 2.19.

$$\int_{V_P} \nabla \cdot \left(\rho\Gamma^{\phi}\nabla\phi\right) dV \cong \sum_{f} \left(\rho\Gamma^{\phi}\nabla\phi\right)_f \cdot \mathbf{S}_f \cong \sum_{f} \left(\rho\Gamma^{\phi}\right)_f \left(\nabla\phi_f \cdot \mathbf{S}_f\right) \tag{2.19}$$

The discretization proceeds by splitting the surface normal vector $\mathbf{S}_f$, which is parallel to unit face normal $\hat{\mathbf{n}}$, into an orthogonal part and a nonorthogonal part. Grid "nonorthogonality" arises when grids are constructed such that the face normal

vector, $\hat{\mathbf{n}}$, is not parallel to the line connecting face centroids in neighboring cells, P and N (see Figure 2.6). The surface normal vector is split into the orthogonal component $\boldsymbol{\Delta}$ and the nonorthogonal component $\mathbf{k}$ (parallel to face f) as shown in Figure 2.6 and given in Equation 2.20.

$$\begin{aligned} \mathbf{S}_f &= \boldsymbol{\Delta} + \mathbf{k} \\ \boldsymbol{\Delta} &= \frac{\mathbf{S}_f \cdot \mathbf{S}_f}{\hat{\mathbf{e}} \cdot \mathbf{S}_f} \hat{\mathbf{e}} \\ \mathbf{k} &= \mathbf{S}_f - \frac{|\mathbf{S}_f|}{\cos\theta} \hat{\mathbf{e}} \end{aligned} \tag{2.20}$$

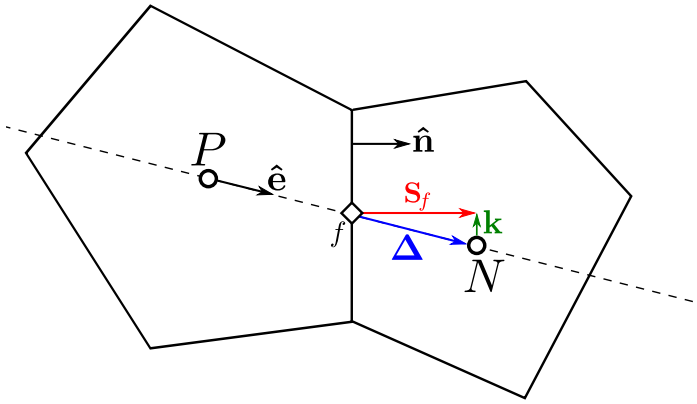

Figure 2.6: Nonorthogonal correction in diffusive flux discretization

With the surface normal vector split, the diffusive flux $\nabla\phi_f \cdot \mathbf{S}_f$ can also be separated into a contribution as would appear on an orthogonal grid plus a nonorthogonal correction as shown in Equation 2.21.

$$(\nabla\phi)_f \cdot \mathbf{S}_f = (\nabla\phi)_f \cdot \boldsymbol{\Delta} + (\nabla\phi)_f \cdot \mathbf{k} \tag{2.21}$$

The orthogonal contribution $(\nabla\phi)_f \cdot \boldsymbol{\Delta}$ can be discretized in terms of cell-centered values of polyhedron P and its surrounding neighbors N. Moreover, the orthogonal contribution can be added to the left-hand-side of the system and treated implicitly. The nonorthogonal contribution is constructed using the prevailing estimate of the

gradient at the face and calculated as in Equation 2.22.

$$(\nabla\phi)_f \cdot \mathbf{k} = (\nabla\phi)_f \cdot \left(\mathbf{S}_f - \frac{|\mathbf{S}_f|}{\cos\theta}\hat{\mathbf{e}}\right) \tag{2.22}$$

2.3.3 Source Term Discretization

The model equation, that is the generic conservation law in Equation 2.16, may contain a source term, $\mathbf{S}^\phi$. The source term for cell P is linearized into an explicit contribution, $\mathbf{S}_u$, and an implicit contribution, $\mathbf{S}_P$. Then, the total source for cell P is given as in Equation 2.23.

$$\mathbf{S}^\phi = \mathbf{S}_u + \mathbf{S}_p\phi_P \tag{2.23}$$

The addition of source terms can be either beneficial or detrimental to solution stability. General practice involves treating as much of the source term implicit as possible, meaning that the implicit contribution should be treated as such (implicitly) only if $\mathbf{S}_p < 0$. Otherwise, if $\mathbf{S}_p > 0$, a strong source term could significantly decrease the diagonal dominance of the linear system. With these considerations, the final discretization of the source term is computed as in Equation 2.24.

$$\int_{V_P} \mathbf{S}^\phi dV = \mathbf{S}_u V_P + \mathbf{S}_p\phi_P V_P \tag{2.24}$$

2.3.4 Temporal Discretization

The discretization of the transient term is treated with a finite difference approach, wherein the temporal variation of cell-centered quantities, ϕ_P, and interpolated face-centered quantities, ϕ_f and $(\nabla\phi)_f$, are disregarded. The transient term is discretized in this work using a second-order (in time) backwards difference formula. The backwards difference formula is derived by taking evaluating ϕ at $t - \Delta t$ and $t - \Delta t - \Delta t^\circ$ in terms of its Taylor series expansion as in Equations 2.25-2.26. Also note that these

Taylor expansions support variable time stepping.

$$\phi(t-\Delta t) = \phi(t) - \Delta t \left.\frac{\partial \phi}{\partial t}\right|_t + \frac{\Delta t^2}{2} \left.\frac{\partial^2 \phi}{\partial t^2}\right|_t + \mathcal{O}(\Delta t^3) \tag{2.25}$$

$$\phi(t-\Delta t-\Delta t^\circ) = \phi(t) - (\Delta t + \Delta t^\circ) \left.\frac{\partial \phi}{\partial t}\right|_t + \frac{(\Delta t + \Delta t^\circ)^2}{2} \left.\frac{\partial^2 \phi}{\partial t^2}\right|_t + \mathcal{O}(\Delta t^3) \tag{2.26}$$

Equations 2.25-2.26 are combined to eliminate the second derivatives and result in the second-order accurate time integration scheme given in Equation 2.27. The following shorthand notation for time level is employed: $\phi^{n+1} \equiv \phi(t)$, $\phi^n \equiv \phi(t-\Delta t)$, $\phi^{n-1} \equiv \phi(t-\Delta t-\Delta t^\circ)$. Variable time stepping is implemented with the notation that time step Δt° advances time level $t^{n-1} \rightarrow t^n$ and time step Δt advances time level $t^n \rightarrow t^{n+1}$.

$$\begin{aligned} \left.\frac{\partial \phi}{\partial t}\right|_t &= \underbrace{\left(\frac{1}{\Delta t} + \frac{1}{\Delta t + \Delta t^\circ}\right)}_{\equiv a_P^\bullet} \phi^{n+1} - \underbrace{\left(\frac{1}{\Delta t} + \frac{1}{\Delta t^\circ}\right)}_{\equiv a_P^\circ} \phi^n + \underbrace{\frac{\Delta t}{\Delta t^\circ(\Delta t + \Delta t^\circ)}}_{\equiv a_P^{\circ\circ}} \phi^{n-1} \\ &= a_P^\bullet \phi^{n+1} + a_P^\circ \phi^n + a_P^{\circ\circ} \phi^{n-1} \end{aligned} \tag{2.27}$$

With the selected second-order approximation for the first time-derivative of ϕ, the discretization of the transient term is completed as shown in Equation 2.28.

$$\int_t^{t+\Delta t} \left[\int_{V_P} \frac{\partial(\rho\phi)}{\partial t} dV \right] dt = \left(a_P^\bullet \phi^{n+1} + a_P^\circ \phi^n + a_P^{\circ\circ} \phi^{n-1}\right) V_P \tag{2.28}$$

2.3.5 VOF Implementation within OpenFOAM

The OpenFOAM specific implementation of VOF is described in Rusche (2002) and Deshpande et al. (2012). This section describes the aspects of the implementation relevant to solving two-phase ship hydrodynamics problems. The conservation of momentum statement in Equation 2.11 is modified in two ways before the solution algorithm is described. First, the pressure term is expanded into a dynamic pressure

and a hydrostatic-like component, primarily for ease of dealing with the sharp pressure gradient through the interface region and ease of specifying boundary conditions. The expansion of pressure is given in Equation 2.29.

$$p = p_d + \rho \mathbf{g} \cdot \mathbf{x} \tag{2.29}$$

The gradient of pressure given the expansion is given in Equation 2.30.

$$\begin{aligned} \nabla p &= \nabla p_d + (\mathbf{g} \cdot \mathbf{x}) \nabla \rho + \rho \nabla (\mathbf{g} \cdot \mathbf{x}) \\ &= \nabla p_d + (\mathbf{g} \cdot \mathbf{x}) \nabla \rho + \rho \mathbf{g} \end{aligned} \tag{2.30}$$

The final modification to Equation 2.11 involves re-writing the viscous stress term. After a small amount of manipulation, by expanding the divergence operator and applying the chain rule, the viscous stress term is re-written as in Equation 2.31. This form has some advantages related to ease of implementation and convergence benefits; the first term on the right-hand side of Equation 2.31 is treated implicitly with the discretization scheme in Section 2.3.2 while the second term is treated explicitly.

$$\nabla \cdot \left[\mu_{\text{eff}} \left(\nabla \mathbf{U} + \nabla \mathbf{U}^T \right) \right] = \nabla \cdot (\mu_{\text{eff}} \nabla \mathbf{U}) + \nabla \mathbf{U} \cdot \nabla \mu_{\text{eff}} \tag{2.31}$$

Substituting Equations 2.30-2.31 into Equation 2.11, the resulting form of the momentum equation is given in Equation 2.32. Notably, the buoyant force, $\rho \mathbf{g}$, cancels with the weight of the fluid and localizes its effect to the interface region ($\nabla \rho \neq \vec{0}$). The source term, $\mathbf{S}$, is retained and acts as the mechanism to introduce momentum from the propeller model as is described in Section 2.5. The source term also acts as the tool used in this work for wave generation and damping (see Appendix A).

$$\frac{\partial \rho \mathbf{U}}{\partial t} + \nabla \cdot \rho \mathbf{U} \mathbf{U} = -\nabla p_d - \mathbf{g} \cdot \mathbf{x} \nabla \rho + \nabla \cdot (\mu_{\text{eff}} \nabla \mathbf{U}) + \nabla \mathbf{U} \cdot \nabla \mu_{\text{eff}} + \rho \mathbf{S} \tag{2.32}$$

The equations are now in a form consistent with the implementation in OpenFOAM and the discretization process and algorithm are outlined. The algorithm follows a segregated approach where momentum and pressure (continuity) are solved separately. Pressure-velocity coupling is enforced through a PISO-type algorithm (Issa, 1986). The algorithm first solves the transport equation for phase fraction (Equation 2.15). Next a predictor step is taken where the momentum equation is solved using values from the prevailing field values. One or more pressure corrector steps are then solved to enforce continuity. Finally, the Spalart-Allmaras transport equation for eddy-viscosity is solved and turbulence quantities are updated.

The solution of the phase fraction equation plays a critical role in the ability to accurately propagate a wave within the Finite Volume Method (FVM). Obtaining an accurate and bounded solution for the phase fraction α proves to be one of the more challenging aspects of the entire solution procedure. The difficulties arise in maintaining boundedness while retaining the sharpness of the discontinuity in the α field without excessive smearing of the interface. The addition of a fictitious term that acts locally and compresses the fluid interface has already been described and listed in Equation 2.15. The following description outlines the numerical discretization and solution algorithm.

The algorithm for the solution of the phase fraction utilizes the Flux Corrected Transport (FCT) method that was originated by Boris and Book (1973), with extension to three dimensions and further improvements by Zalesak (1979). The FCT method consists of the following steps:

1. Compute a low order convective flux, $\mathbf{F}^L$, using a monotone scheme. Advance the solution in time to obtain a low-order, bounded estimate of α and $\mathbf{F}^L$.

2. Compute a time-advanced, high order convective flux, $\mathbf{F}^H$, using a high-resolution scheme.

3. Compute the anti-diffusive flux, $\mathbf{A} = \mathbf{F}^H - \mathbf{F}^L$.

4. Compute the corrected flux, $\mathbf{F}^C = \mathbf{F}^L + \Lambda\mathbf{A}$ where $0 \leq \Lambda \leq 1$.

5. Advance the phase-fraction, α, in time using the corrected fluxes; $\frac{\partial \alpha}{\partial t} V_P + \sum_f \left(\mathbf{F}^C \cdot \mathbf{S}\right)_f = 0$.

Step 1 is achieved using an implicit Euler time integration scheme with convective fluxes discretized with the first order upwind scheme. The construction of time-advanced, high-order convective flux in Step 2 is accomplished using a van Leer limiter (van Leer, 1979). The anti-diffusive flux, $\mathbf{A}$, is algebraically computed in Step 3. In Step 4, the corrected flux, $\mathbf{F}^C$, forms a blend of the low-order and high-order flux through the limiter, Λ; the corrected flux tends towards the high-order flux for $\Lambda = 1$ and towards the low-order flux for $\Lambda = 0$. In OpenFOAM, the Multidimensional Universal Limiter with Explicit Solution (*MULES*) algorithm computes the limiters. The *MULES* algorithm also computes the time-advanced solution for the phase-fraction, α, using the corrected flux. Within the *MULES* algorithm, steps 2-5 are treated iteratively *nAlphaCorr* times. The key to the FCT procedure is Step 4 where the proper amount of anti-diffusive flux is added to the low order flux to guarantee boundedness of the solution while using as much of the high order flux as possible.

The two-phase algorithm solves a predictor step for momentum after the phase fraction has been updated. The momentum equation is integrated over each cell volume to yield the integral form in Equation 2.33.

$$\begin{aligned} \int_V \left[\frac{\partial \rho \mathbf{U}}{\partial t} + \nabla \cdot \rho \mathbf{U}\mathbf{U}\right] dV = &\int_V \left[\nabla \cdot (\mu_{\text{eff}} \nabla \mathbf{U}) + \nabla \mathbf{U} \cdot \nabla \mu_{\text{eff}} + \rho \mathbf{S}\right] dV \\ &+ \int_V \left[-\nabla p_d - \mathbf{g} \cdot \mathbf{x} \nabla \rho\right] dV \end{aligned} \tag{2.33}$$

After application of the aforementioned discretization schemes, the discrete form of the momentum equation for cell P is assembled in Equation 2.34. The operator,

$\mathcal{R}$, represents a reconstruction operation where the cell-center values of ∇p_d and $(\mathbf{g}\cdot\mathbf{x})\nabla\rho$ are reconstructed from a weighted average of fluxes through faces bounding cell P. The reconstruction operator, $\mathcal{R}$, aids in preventing spurious currents through the fluid interface. Spurious currents are prone to occur due to source terms with sharp gradients through the interface, as are found in terms ∇p_d and $(\mathbf{g}\cdot\mathbf{x})\nabla\rho$.

$$\begin{aligned}\Big(a_P^{\bullet}(\rho\mathbf{U})^{n+1} + a_P^{\circ}(\rho\mathbf{U})^{n} + a_P^{\circ\circ}(\rho\mathbf{U})^{n-1}\Big)V_P + \sum_f \Big(\mathbf{S}_f\cdot(\rho\mathbf{U})_f\Big)\mathbf{U}_f = \\ \sum_f (\mu_{\text{eff}})_f\,(\nabla\mathbf{U})_f\cdot\mathbf{S}_f + \Big(\nabla\mathbf{U}\cdot\nabla\mu_{\text{eff}}\Big)V_P + (\rho\mathbf{f}_b)\,V_P \\ + \mathcal{R}\Big\{\Big[-(\nabla p_d)_f - (\mathbf{g}\cdot\mathbf{x})_f\,(\nabla\rho)_f\Big]\,|\mathbf{S}_f|\Big\}\end{aligned} \tag{2.34}$$

The momentum predictor given in Equation 2.34 is solved for a velocity estimate, $\mathbf{U}^*$. At this stage in the algorithm, $\mathbf{U}^*$ is not divergence-free and does not satisfy the continuity equation. To enforce conservation of mass, the pressure is updated through the semi-discrete momentum equation. The coefficients arising from the various discretization schemes employed in discretizing Equation 2.34 are assembled for cell P into the semi-discrete form given in Equation 2.35. In the semi-discrete form the pressure and buoyancy terms are not yet discretized.

$$a_P\mathbf{U}_P = \mathbf{H}(\mathbf{U}) - \nabla p_d - (\mathbf{g}\cdot\mathbf{x})\nabla\rho \tag{2.35}$$

The $\mathbf{H}(\mathbf{U})$ term includes the discretization coefficients proportional to all neighboring cell-center values and a contribution from the transient term. The velocity from the momentum predictor is then interpolated to the bounding cell faces, where the flux $\Phi_u \equiv \mathbf{U}_f\cdot\mathbf{S}_f$ is formed, as shown in Equation 2.36. The first two terms on the right hand side of Equation 2.36 are grouped into a flux from the momentum predictor, Φ^*. The remaining "pressure flux" serves as a flux correction to the momentum flux predictor, where Equation 2.36 uses the notation $\nabla_f^{\perp} p_d$ for the surface normal

gradient of pressure.

$$\begin{aligned}\Phi_u = \mathbf{U}_f \cdot \mathbf{S}_f &= \left(\frac{\mathbf{H}(\mathbf{U})}{a_P}\right)_f \cdot \mathbf{S}_f - \left(\frac{1}{a_P}\right)_f \Big((\mathbf{g}\cdot\mathbf{x})\nabla\rho\Big)_f \cdot \mathbf{S}_f - \left(\frac{1}{a_P}\right)_f (\nabla p_d)_f \cdot \mathbf{S}_f \\ &= \Phi^* - \left(\frac{1}{a_P}\right)_f (\nabla_f^{\perp} p_d)|\mathbf{S}_f|\end{aligned} \tag{2.36}$$

The semi-discrete form of the momentum equation is inserted into the discrete continuity equation, $\sum_f \Phi_u = 0$. This leads to the final discretized form of the pressure equation for cell P given in Equation 2.37.

$$\sum_f \left(\frac{1}{a_P}\right)_f (\nabla_f^{\perp} p_d)|\mathbf{S}_f| = \sum_f \Phi^* \tag{2.37}$$

The flux from the momentum predictor, Φ^*, is corrected, making it a conservative flux, using Equation 2.36 and using the updated pressure flux from the solution of Equation 2.37. Recalling that the velocity field, $\mathbf{U}^*$, from the momentum predictor is not a divergence-free field, a correction is also made to the velocity field, U_P. Equation 2.38 shows the correction to the cell-centered velocity field, where reconstruction operator $\mathcal{R}$ is used to reconstruct cell-center values from cell-face values.

$$\mathbf{U}_P = \frac{\mathbf{H}(\mathbf{U})}{a_P} + \frac{1}{a_P}\mathcal{R}\left\{(-\mathbf{g}\cdot\mathbf{x})_f \nabla_f^{\perp}\rho|\mathbf{S}_f| - \nabla_f^{\perp} p_d|\mathbf{S}_f|\right\} \tag{2.38}$$

Following the solution for the mean velocity field, $\mathbf{U}$, the mean dynamic pressure field, p_d, and the turbulent stresses, the hydrodynamic forces are readily computed over the instantaneous hull and rudder surfaces ($S_B \cup S_R$) using Equation 2.39.

$$\begin{aligned}\mathbf{F} &= \iint_{S_B \cup S_R} \left[-p\hat{\mathbf{n}} + \mu_{\text{eff}}\left(\nabla\mathbf{U} + \nabla\mathbf{U}^T\right)\cdot\hat{\mathbf{n}}\right] dS \\ \mathbf{M} &= \iint_{S_B \cup S_R} \mathbf{x} \times \left[-p\hat{\mathbf{n}} + \mu_{\text{eff}}\left(\nabla\mathbf{U} + \nabla\mathbf{U}^T\right)\cdot\hat{\mathbf{n}}\right] dS\end{aligned} \tag{2.39}$$

The governing equations are solved on a moving grid using an Arbitrary Lagrangian Eulerian (ALE) approach. OpenFOAM version 2.4.0 offers a diverse selection of solvers including multiple multi-phase solvers. In this work, a modified version of the *waveDyMFoam* (Jacobsen et al., 2012) solver is used. The solver builds on top of the native OpenFOAM solver, *interDyMFoam*, with the addition of wave generation and damping relaxation zone capabilities (Filip et al., 2017).

2.3.6 Boundary Conditions

The governing equations and algorithm for the OpenFOAM implementation of VOF are described in Section 2.3.5. In the described implementation, using the Spalart-Allmaras turbulence model, boundary conditions are required for the following quantities: α, $\mathbf{U}$, p_d, $\tilde{\nu}$, and ν_t. This section describes boundary conditions for all field quantities for both the VOF method and the hybrid method.

As a point of emphasis, the same two-phase solver (described in Section 2.3.5) is used for both the single-phase RANS component of the hybrid method and for nonlinear VOF computations with free-surface capturing. The two-phase solver is utilized for the CFD component of the hybrid method even though the free-surface is approximated as a flat surface and only the water phase is modeled. The two-phase solver is utilized within the hybrid method in order to allow for an equal comparison between the hybrid method and VOF results. This measure attempts to eliminate any differences in results due to differences in the solver algorithm. However, some differences in boundary conditions are unavoidable due to wave generation within the VOF method with free-surface capturing.

The boundary conditions for α, $\mathbf{U}$, p_d, $\tilde{\nu}$, and ν_t are specific to the type of boundary patch. To facilitate this description, the names and locations of each boundary patch are shown in Figure 2.7. The "Top" (yellow) patch is located above the ship hull in the $z = 0.6L$ plane in the VOF method, where L is the length of ship between

perpendiculars. Alternatively, the "Top" patch in the hybrid method is located in the calm-water $z = 0$ plane and intersects the "Hull and Rudder" patch. The "Bottom" (red) patch is located in the $z = -L$ plane in all meshes, for both hybrid method and VOF with free-surface capturing, in this thesis. The "Inlet" (blue) patch is formed as the cylindrical surface bounded by the "Top" and "Bottom" patches. According to this description, the "Hull and Rudder" and "Inlet" patches are truncated for the hybrid method domains above $z = 0$, which is the "Top" boundary.

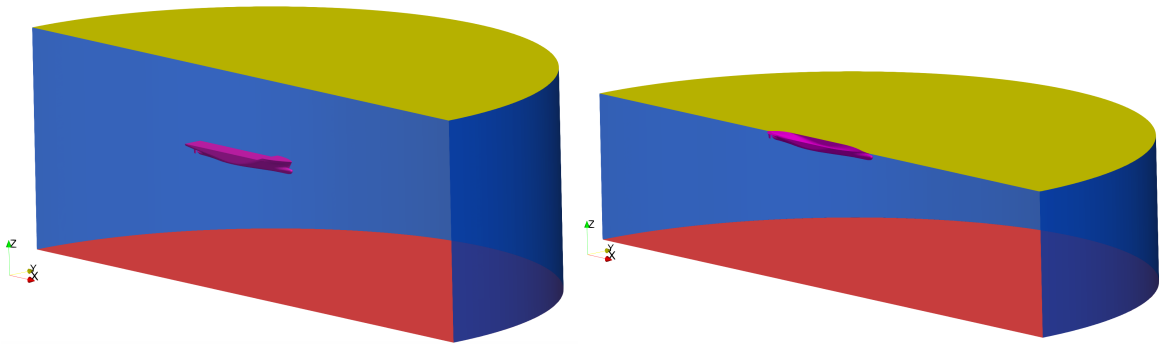

(a) (b)

Figure 2.7: (a) Boundary patches ($y > 0$) and hull and rudder patches for VOF mesh (b) Boundary patches ($y > 0$) and hull and rudder patches for hybrid method mesh. Boundary patches shown are Top (yellow), Inlet (blue), Bottom (red), and Hull and Rudder (magenta).

First, a description is given for boundary conditions that are used in both the VOF method and in the hybrid method. In OpenFOAM, the Dirichlet boundary condition is titled *fixedValue* and may be applied to scalar or vector fields. A Neumann boundary condition for zero normal gradient at the boundary patch is called *zeroGradient*. The last general type of boundary condition is *inletOutlet* which is a mixed-type boundary condition. On a patch using the *inletOutlet* boundary condition, *fixedValue* is applied for cell faces with flux into the domain and *zeroGradient* is applied for cell faces with flux out of the domain.

Table 2.1 lists the boundary conditions applied on the patches for simulations using the VOF method with free-surface capturing and wave generation. The "Top"

patch features a velocity-pressure combination of *pressureInletOutletVelocity* and *totalPressure* respectively. These two conditions work together to model a boundary where some inflow occurs such as the atmosphere on the "Top" patch. The *pressureInletOutletVelocity* applies a *zeroGradient* condition to each velocity component for all cases except for inflow, where the velocity normal to the patch is derived from the flux into the domain. The *totalPressure* produces a corresponding response the the velocity by applying the dynamic pressure $p_d = -1/2\rho|\mathbf{U}|^2$ for inward flux and $p_d = 0$ for outward flux. In this manner, an inward flux permitted by *pressureInletOutletVelocity* is met with a pressure gradient provided by the *totalPressure* condition on p_d; for outward flux this combination of velocity-pressure conditions reduces to a standard outflow condition.

The "Inlet" and "Bottom" patches are combined in Table 2.1 because they share identical conditions in the VOF method. The *waveAlpha* and *waveVelocity* boundary conditions are custom to the *waves2Foam* (Jacobsen et al., 2012) library. Both *waveAlpha* and *waveVelocity* are Dirichlet conditions where time-varying wave amplitude and kinematics are prescribed as boundary values (see Appendix A).

Table 2.1: Boundary conditions for VOF simulations

Field \ Patch	Top	Inlet & Bottom	Hull and Rudder
α	*inletOutlet*	*waveAlpha*	*zeroGradient*
$\mathbf{U}$	*pressureInletOutletVelocity*	*waveVelocity*	*movingWallVelocity*
p_d	*totalPressure*	*fixedFluxPressure*	*fixedFluxPressure*
$\tilde{\nu}$	*zeroGradient*	*inletOutlet*	*fixedValue*
ν_t	*zeroGradient*	*inletOutlet*	*nutUSpaldingWallFunction*

The *fixedFluxPressure* boundary condition on dynamic pressure, p_d, is a derived boundary condition. The normal gradient of pressure is derived by re-arranging the semi-discrete momentum equation (Equation 2.36) as follows:

$$\nabla_f^{\perp} p_d = \left[\left(\frac{\mathbf{H}(\mathbf{U})}{a_P} \right)_f \cdot \mathbf{S}_f - \mathbf{U}_f \cdot \mathbf{S}_f - \left(\frac{1}{a_P} \right)_f \Big((\mathbf{g} \cdot \mathbf{x}) \nabla \rho \Big)_f \cdot \mathbf{S}_f \right] \frac{(a_P)_f}{|\mathbf{S}_f|} \tag{2.40}$$

For the turbulence quantities, $\tilde{\nu}$ and ν_t, the *inletOutlet* condition is applied on both "Inlet" and "Bottom" patches and the *zeroGradient* condition is applied on the "Top" patch. The wall function *nutUSpaldingWallFunction* (Spalding, 1961) is used on the "Hull and Rudder" patch. The *movingWallVelocity* boundary condition for **U** receives the velocity on each cell face of the "Hull and Rudder" boundary patch from the equation of motion solver, thus enforcing a no-slip condition on the wall.

Table 2.2 lists the boundary conditions applied on the patches for the RANS component of the hybrid method. The boundary conditions on the "Hull and Rudder" patch are identical to the VOF boundary conditions except for use of a *zeroGradient* condition on p_d rather than *fixedFluxPressure*. The "Top" patch is treated with a *symmetryPlane* boundary condition for all field quantities. The *symmetryPlane* boundary condition acts as a slip-wall where a *zeroGradient* condition is applied to vector components parallel to the wall and a zero-flux condition is applied for vector components normal to the wall. For scalar quantities, the *symmetryPlane* condition enforces zero normal gradient.

Table 2.2: Boundary conditions for RANS component of hybrid method

Field \ Patch	Top	Inlet	Bottom	Hull and Rudder
α	*symmetryPlane*	*waveAlpha*	*inletOutlet*	*fixedValue*
U	*symmetryPlane*	*waveVelocity*	*zeroGradient*	*movingWallVelocity*
p_d	*symmetryPlane*	*fixedFluxPressure*	*fixedValue*	*zeroGradient*
$\tilde{\nu}$	*symmetryPlane*	*inletOutlet*	*fixedValue*	*fixedValue*
ν_t	*symmetryPlane*	*inletOutlet*	*fixedValue*	*nutUSpaldingWallFunction*

The "Top" patch no longer acts as a Dirichlet condition, as with the *totalPressure* condition used on the "Top" patch in the VOF simulations, due to application of the *symmetryPlane* boundary condition. Consequently, the "Inlet" and "Bottom" patches are treated separately in the hybrid method to address this issue. A *fixedValue* of zero dynamic pressure is applied on the "Bottom" patch which equates to specifying the hydrostatic pressure as the total pressure on the "Bottom" patch. The velocity

is treated as *zeroGradient* on the "Bottom" patch, meaning the combined velocity-pressure boundary conditions is a standard outflow condition.

The *waveAlpha* and *waveVelocity* conditions are applied on the "Inlet" boundary in the hybrid method. However, because the ship advances into calm-water using the Arbitrary Lagrangian Eulerian formulation, these conditions amount to Dirichlet conditions of $\alpha = 1$ and $\mathbf{U} = \vec{0}$ on the "Inlet". The relaxation zone technique, described in Appendix A, is used to gradually force the ship's wake velocity back to its freestream value of $\mathbf{U} = \vec{0}$.

The description of the two different types of CFD used in this work is now complete. A fully-nonlinear VOF method is outlined for use in generating high-fidelity comparison data for benchmarking the performance of the hybrid method. A simplified version of CFD is described for use in the hybrid method, where the free-surface is approximated as the flat calm-water plane. The algorithm for the fluid solver used to solve each of these types of CFD is identical to allow for consistent comparison. The main difference between the methods is the omission of a free-surface in the CFD done for the hybrid method. Section 2.4 describes the theory and numerics for computation of wave forces that are not resolved in the simplified CFD for the hybrid method.

2.4 Time-domain High-Order Boundary Element Method

Ship seakeeping computations are routinely modeled assuming incompressible, inviscid, and irrotational flow. The supporting argument behind these assumptions is that inertia and gravitational forces dominate the physics of water wave propagation in a variety of problems. Thus, a mature theory exists for solving wave-body interactions when the floating structure is at zero speed. These methods have been extended to forward speed theories, generally under the restriction that the ship is advancing with constant speed and heading. The assumptions of constant speed and heading

can be relaxed, as will be discussed subsequently in this section.

The time-domain BEM is the numerical framework used in the hybrid method to solve the incompressible, inviscid, and irrotational flow. The governing equation is Laplace's equation which solves for a velocity potential rather than directly for the velocity field. The total perturbation velocity potential, ψ, is a scalar function and $\nabla\psi$ yields the velocity field in the Earth-fixed inertial frame.

A boundary integral equation that satisfies the Laplace's equation for ψ is formed through an application of Green's third identity. This technique transforms the problem from a solution to $\nabla^2\psi = 0$ in the entire fluid domain to a solution over the bounding surfaces of the fluid domain, effectively reducing the dimension of the problem. The boundary integral equation for $\psi(\mathbf{x})$, where $\mathbf{x}$ is a field point on the body surface or free surface ($S_B \cup S_F$), is given in Equation 2.41.

$$2\pi\psi(\mathbf{x}) - \iint\limits_{S_B \cup S_F} \frac{\partial\psi(\mathbf{x}')}{\partial n} G(\mathbf{x}';\mathbf{x}) d\mathbf{x}' + \iint\limits_{S_B \cup S_F} \psi(\mathbf{x}') \frac{\partial G(\mathbf{x}';\mathbf{x})}{\partial n} d\mathbf{x}' = 0 \tag{2.41}$$

In this work the relevant bounding surfaces are the submerged portion of the surface of the floating body, S_B, and the free surface, S_F. The dynamics of the body provide a boundary condition for the normal gradient of ψ on S_B and the physics governing propagation of inviscid gravity waves provides a boundary condition for ψ on S_F. Placing known terms on the right-hand side of Equation 2.41, it is re-written as Equation 2.42.

$$2\pi\psi(\mathbf{x}) + \iint\limits_{S_B} \psi \frac{\partial G}{\partial n} d\mathbf{x}' - \iint\limits_{S_F} \frac{\partial\psi}{\partial n} G d\mathbf{x}' = \iint\limits_{S_B} \frac{\partial\psi}{\partial n} G d\mathbf{x}' - \iint\limits_{S_F} \psi \frac{\partial G}{\partial n} d\mathbf{x}' \tag{2.42}$$

The boundary integral Equation 2.42 holds, in general, when modeling fully nonlinear wave-body interaction. However, in a nonlinear formulation the surfaces S_B and S_F vary nonlinearly in time and so the integrals must be computed at every time

step. Furthermore, the Green's function, G, varies in time if the source point, $\mathbf{x}'$, varies its position in time.

A wide variety of wave conditions exist that can be modeled with a linear approach. The linearization of the problem significantly benefits the computational efficiency of the problem because the integrals in Equation 2.42 can be precomputed and stored before time-integration of the free surface profile and body motion. The hybrid method proposed in this work is designed for efficiency and utilizes a linearized formulation. The next section provides mathematical formulation of the seakeeping BVP's.

2.4.1 Seakeeping Flow Linearization

The formulation of the seakeeping BVP's involves linearization of the kinematics of the body and resulting body boundary condition as well a linearization of boundary conditions on the free surface. The BVP's are linearized about a maneuvering frame that moves steadily with the ship in the horizontal plane. The velocity of a point in the domain that is described in the maneuvering (x, y, z) coordinates is $\mathbf{W} = (U - \dot{\Psi}y, V + \dot{\Psi}x, 0)^T$ with respect to the maneuvering frame of reference. Time derivatives in the Earth-fixed frame, denoted d/dt, are related to time derivatives in the maneuvering frame, denoted $\partial/\partial t$, through the Galilean transformation in Equation 2.43. The ship maneuvering frame (middle frame depicted in Figure 2.8) translates in the horizontal plane away from the Earth-fixed origin, O_E, according to displacement vector $\mathbf{X}_E$ and changes heading relative to the Earth-fixed frame with heading angle Ψ.

$$\frac{d}{dt} = \frac{\partial}{\partial t} - \mathbf{W} \cdot \nabla \tag{2.43}$$

A consistent linearization is more readily performed by splitting the total perturbation potential into a summation of a basis flow potential, Φ, and a a first order disturbance potential, $\phi^{(1)}$. The first-order potential, $\phi^{(1)}$, is composed of the follow-

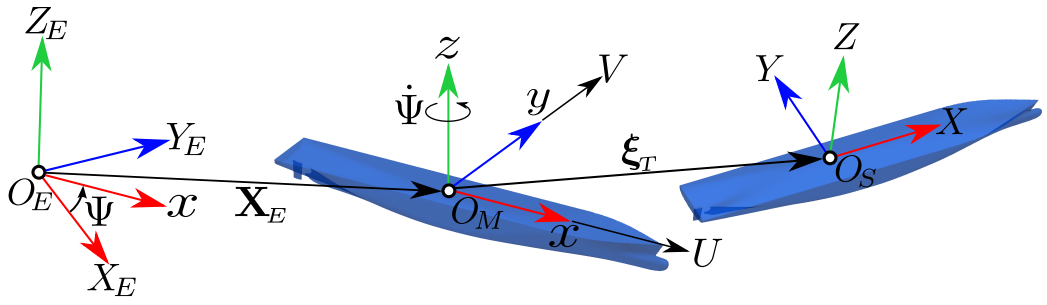

Figure 2.8: Coordinate systems used in the hybrid method

ing potentials: a local potential, ϕ, a wave-disturbance potential, φ, and an incident wave potential, φ_i. The basis flow potential, Φ, is assumed to be an $\mathcal{O}(1)$ contribution to the total perturbation potential, where the local and wave potentials are assumed to be $\mathcal{O}(\epsilon)$ where $\epsilon \ll 1$.

$$\begin{aligned} \psi(\mathbf{x},t) &= \Phi(\mathbf{x}) + \phi^{(1)} \\ &= \underbrace{\Phi(\mathbf{x})}_{\mathcal{O}(1)} + \underbrace{\phi(\mathbf{x},t) + \varphi(\mathbf{x},t) + \varphi_i(\mathbf{x},t)}_{\mathcal{O}(\epsilon)} \end{aligned} \tag{2.44}$$

The double-body potential, $\Phi(\mathbf{x})$, is an optional basis flow first proposed by Dawson (1977). The flow serves as an $\mathcal{O}(1)$ "basis" about which the perturbation expansion for the flow field is made. Unlike the Neumann-Kelvin linearization which takes the undisturbed free stream as the basis flow, the double-body basis potential, $\Phi(\mathbf{x})$, satisfies the boundary value problem in Equation 2.45.

$$2\pi\Phi(\mathbf{x}) + \iint\limits_{S_B} \Phi \frac{\partial G}{\partial n} d\mathbf{x}' - \iint\limits_{S_F} \frac{\partial \Phi}{\partial n} G d\mathbf{x}' = \iint\limits_{S_B} \frac{\partial \Phi}{\partial n} G d\mathbf{x}' - \iint\limits_{S_F} \Phi \frac{\partial G}{\partial n} d\mathbf{x}' \tag{2.45}$$

$$\frac{\partial \Phi}{\partial n} = \frac{\partial \Phi}{\partial z} = 0 \text{ on } z = 0 \tag{2.46}$$

$$\frac{\partial \Phi}{\partial n} = \mathbf{W} \cdot \hat{\mathbf{n}} \text{ on } S_{\overline{B}} \tag{2.47}$$

In the following linearization process all body boundary conditions are expanded about the exact horizontal-plane position of the hull, $S_{\overline{B}}$, and all boundary condi-

tions on the free surface are expanded about the $z = 0$ calm water plane. The hull surface in the horizontal plane, $S_{\overline{B}}$, corresponds to the portion of the hull below the $z = 0$ calm-water plane in the absence of any seakeeping displacements. The double-body potential then satisfies the following Boundary Integral Equation (BIE) in Equation 2.48.

$$2\pi\Phi(\mathbf{x}) + \iint\limits_{S_{\overline{B}}} \Phi \frac{\partial G}{\partial n} d\mathbf{x}' + \iint\limits_{S_F} \Phi \frac{\partial G}{\partial n} d\mathbf{x}' = \iint\limits_{S_{\overline{B}}} (\mathbf{W} \cdot \hat{\mathbf{n}})\, G d\mathbf{x}' \tag{2.48}$$

In this work, the simpler Neumann-Kelvin linearization is utilized, which amounts to setting $\Phi = 0$ and $\nabla\Phi = \vec{0}$ and taking the basis flow to be the free stream velocity field. However, the hybrid method formulation does not rely on one particular linearization and the double-body linearization serves as a point of extension, and perhaps improvement, for the hybrid method. For this purpose, the double-body potential is included in the following linearization process.

Now that options for the basis flow have been established, the linearization proceeds by addressing the BVP's governing the local flow potential, ϕ, and wave flow potential, φ. The local flow BVP satisfies a body boundary condition that includes all unsteady effects due to the wave-induced ship motions. The local potential, ϕ, satisfies a homogenous condition $\phi = 0$ on $z = 0$ which represents an infinite Froude number approximation to the free surface boundary condition. The radiated waves are accounted for in the wave flow BVP where the flux from ϕ is a forcing term on the free surface. To establish a linear body boundary condition on the mean position of the hull, the starting point is the exact body boundary condition in Equation 2.49. The exact body-boundary is enforced through a zero-flux condition on the exact hull surface, S_B. The flux from ψ must cancel the sum of fluxes due to steady motion, $\mathbf{W}$, and wave-induced unsteady motion, $\dot{\boldsymbol{\delta}}$.

$$\frac{\partial \psi}{\partial n} = \mathbf{W} \cdot \hat{\mathbf{N}} + \dot{\boldsymbol{\delta}} \cdot \hat{\mathbf{N}} \text{ on } S_B \tag{2.49}$$

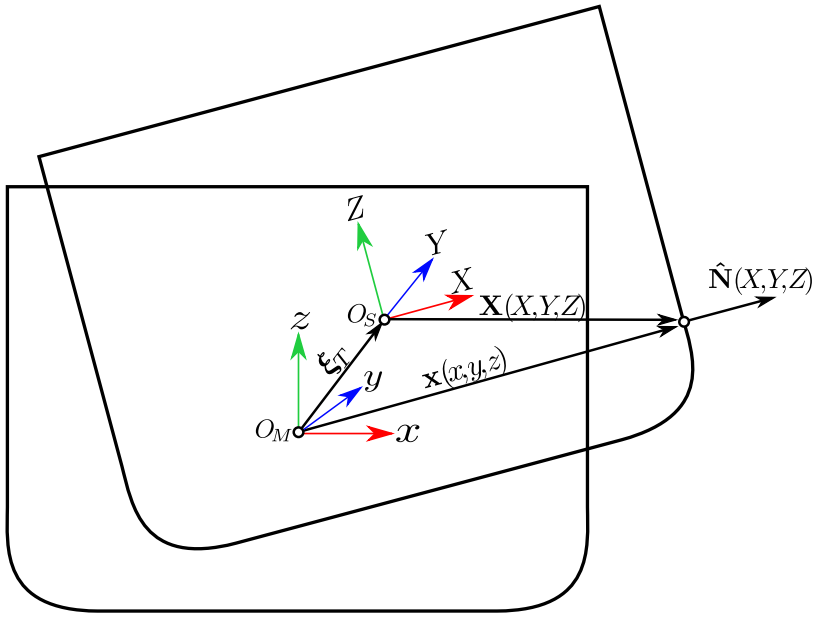

Figure 2.9: Body-fixed system $O_S(X, Y, Z)$ and maneuvering system $O_M(x, y, z)$

To obtain a boundary condition linearized about the mean position of the hull on surface $S_{\overline{B}}$, a Taylor expansion is made for small displacements of the hull. The displacement vector, $\boldsymbol{\xi} \equiv \mathbf{x} - \mathbf{X}$, of a point $\mathbf{X}(X, Y, Z)$ on the instantaneous hull surface relative to the same point on the hull in its mean position is given to $\mathcal{O}(\epsilon)$ in Equation 2.50. A similar expansion is made for the unit normal vector on the hull, also listed in Equation 2.50.

$$\begin{aligned} \mathbf{x} - \mathbf{X} &= \epsilon \left(\boldsymbol{\xi}_T + \boldsymbol{\xi}_R \times \mathbf{X} \right) \\ \hat{\mathbf{n}} &= \hat{\mathbf{N}} + \epsilon \left(\boldsymbol{\xi}_R \times \hat{\mathbf{N}} \right) \end{aligned} \tag{2.50}$$

When the expansions in Equation 2.50 are inserted into the exact body boundary condition and terms up to $\mathcal{O}(\epsilon)$ are retained, as first done in the work of Timman and Newman (1962), the linearized body boundary condition - using the notation of

Ogilvie and Tuck (1969) - is given in Equation 2.51.

$$\frac{\partial \phi}{\partial n} = \sum_{j=1}^{6} \left(\frac{\partial \xi_j}{\partial t} n_j + \xi_j m_j \right) \quad \text{on } S_{\overline{B}} \tag{2.51}$$

The so-called n_j and m_j terms are calculated as in Equation 2.52.

$$\begin{aligned} (n_1, n_2, n_3) &= \hat{\mathbf{n}} \\ (n_4, n_5, n_6) &= \mathbf{x} \times \hat{\mathbf{n}} \\ (m_1, m_2, m_3) &= (\hat{\mathbf{n}} \cdot \nabla) \left(\mathbf{W} - \nabla \Phi \right) \\ (m_4, m_5, m_6) &= (\hat{\mathbf{n}} \cdot \nabla) \left(\mathbf{x} \times (\mathbf{W} - \nabla \Phi) \right) \end{aligned} \tag{2.52}$$

The local potential is split again, following the index notation of Ogilvie (1964), into six potentials. The potential, ϕ_k, for the k^{th} generalized degree of freedom is a linear combination of two canonical potentials, $\mathcal{N}_k$ and $\mathcal{M}_k$, where $\mathcal{N}_k$ is proportional to the velocity in the k^{th} mode and $\mathcal{M}_k$ is proportional to the displacement in the k^{th} mode. Given the decomposition according to Ogilvie (1964), the local potential then satisfies a BIE and is subject to the boundary conditions in Equation 2.53 for $k = 1, ..., 6$.

$$\begin{aligned} \mathcal{N}_k = 0, \quad \mathcal{M}_k = 0 \quad &\text{on } z = 0 \\ \frac{\partial \mathcal{N}_k}{\partial n} = n_k, \; \frac{\partial \mathcal{M}_k}{\partial n} = m_k \quad &\text{on } S_{\overline{B}} \end{aligned} \tag{2.53}$$

In Equation 2.51, the n- and m-terms are calculated as $(n_1, n_2, n_3, n_4, n_5, n_6) = (\hat{n}, \vec{x} \times \hat{n})$ and $(m_1, m_2, m_3, m_4, m_5, m_6) = (0, 0, 0, 0, Un_3, -Un_2)$ respectively.

The last BVP governs the radiated and diffracted wave flow. The implementation in Aegir solves the linearized kinematic and dynamic boundary conditions separately with an explicit-implicit formulation, rather than solving a combined free surface boundary condition. The linear kinematic and dynamic boundary conditions are

stated in Equations 2.54 and 2.55 respectively.

$$\frac{\partial \zeta}{\partial t} - \Big(\mathbf{W} - \nabla\Phi\Big) \cdot \nabla\zeta = \frac{\partial^2 \Phi}{\partial z^2}\left(\zeta + \zeta_I\right) + \frac{\partial \phi}{\partial z} + \frac{\partial \varphi}{\partial z} - \nabla\Phi \cdot \nabla\zeta_I \tag{2.54}$$

$$\frac{\partial \varphi}{\partial t} - \Big(\mathbf{W} - \nabla\Phi\Big) \cdot \nabla\varphi = -g\zeta + \left[\mathbf{W} \cdot \nabla\Phi - \frac{1}{2}\nabla\Phi \cdot \nabla\Phi\right] - \nabla\Phi \cdot \nabla\varphi_I \tag{2.55}$$

With the wave potential known on the calm-water surface ($z = 0$ plane) from Equation 2.55 and the diffraction problem enforced on the mean hull surface, i.e. $\partial\varphi/\partial n = -\partial\varphi_I/\partial n$, the wave potential BVP is formulated and solved as given in Equation 2.56.

$$2\pi\varphi(\mathbf{x}) + \iint\limits_{S_{\overline{B}}} \varphi \frac{\partial G}{\partial n} d\mathbf{x}' - \iint\limits_{S_F} \frac{\partial \varphi}{\partial n} G d\mathbf{x}' = \iint\limits_{S_{\overline{B}}} -\frac{\partial \varphi_I}{\partial n} G d\mathbf{x}' - \iint\limits_{S_F} \varphi \frac{\partial G}{\partial n} d\mathbf{x}' \tag{2.56}$$

The total perturbation potential at the current time step can now be computed as the sum of the double-body potential from the solution of Equation 2.48, the local potential, the disturbance wave potential from the solution to Equation 2.56, and the analytic incident potential given in Equation 2.57.

$$\varphi_I = \frac{g\zeta_I}{\omega_0} e^{kz} \sin\left(k\left(x\cos\left(\chi - \Psi(t)\right) + y\sin\left(\chi - \Psi(t)\right) + X_{_E}(t)\cos\chi + Y_{_E}(t)\sin\chi\right) - \omega_0 t\right) \tag{2.57}$$

The incident wave potential, heading, and encounter frequency are time dependent in this implementation. The incident wave heading is fixed relative to Earth-fixed coordinates, with wave heading direction given by the angle, χ, as shown in Figure 2.10. The mechanism for turning the wave relative to the maneuvering frame is the maneuvering state vector, composed of the time dependent position of the ship in Earth-fixed coordinates, $\mathbf{X}_{_E}(t)$ and heading, $\Psi(t)$.

With the solution to the BVP's complete, the solution for the total perturbation potential, ψ, is complete. The first-order unsteady hydrodynamic forces may now be

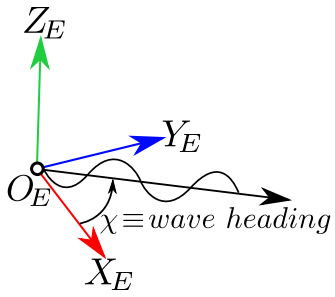

Figure 2.10: Incident wave heading relative to Earth-fixed frame of reference

computed as a function of the first-order potential, $\phi^{(1)}$, using Bernoulli's equation as in Equation 2.58; the $\mathcal{O}(1)$ basis potential, Φ, makes no contribution to first-order unsteady wave forces.

$$\mathbf{F^{(1)}} = -\rho \iint\limits_{S_{\overline{B}}} \left(\frac{\partial \phi^{(1)}}{\partial t} - (\mathbf{W} - \nabla\Phi) \cdot \nabla\phi^{(1)} \right) \begin{Bmatrix} \hat{\mathbf{n}} \\ \mathbf{x} \times \hat{\mathbf{n}} \end{Bmatrix} dS \tag{2.58}$$

2.4.2 Second-order Force Calculation

A direct pressure integration method is implemented in Aegir and used to calculate second-order wave forces in this work. The direct pressure integration method is a so-called near field technique because it only requires fluid velocity directly on the hull surface, rather than on the free surface or over a control surface, as in a momentum conservation method. The formulation implemented in Aegir was developed by Joncquez (2009) and incorporates interactions between the steady double-body basis flow (if selected as the basis potential) and the unsteady waves, as well and changes in flare angle at the waterline.

The total hydrodynamic force and moment on the body in the maneuvering frame is calculated by Equation 2.59. Equation 2.59 provides an exact, nonlinear expression for the total nonlinear hydrodynamic force and moment about O_M in the maneuvering frame of reference. As such, the surface integral is performed over the instantaneous wetted hull surface.

$$\begin{Bmatrix} \mathbf{F} \\ \mathbf{M} \end{Bmatrix} = -\iint_{S_B} p(\mathbf{x}) \begin{Bmatrix} \hat{\mathbf{n}} \\ \mathbf{x} \times \hat{\mathbf{n}} \end{Bmatrix} dS \tag{2.59}$$

The BVP's for the seakeeping problem are linearized about the maneuvering coordinate system and all field quantities are described in (x, y, z) coordinates. To obtain an expression for pressure on the hull surface (displaced from mean position in the maneuvering system by first-order seakeeping displacements), the pressure is expanded to second-order about the mean position of the hull. Retaining terms up to $\mathcal{O}(\epsilon^2)$, the expansion of the pressure about the hull in its mean position is given in Equation 2.60.

$$p(\mathbf{x}) = p(\mathbf{x}) + (\mathbf{x} - \mathbf{X}) \cdot \nabla p(\mathbf{x}) \tag{2.60}$$

The Taylor expansion of the fluid pressure also requires expansions of the hull surface, described in the displaced position by vector, $\mathbf{x}$, and unit outward normal vector, $\hat{\mathbf{n}}$. The displacement vector, $\mathbf{x}-\mathbf{X}$, from a point fixed on the mean hull surface, $S_{\overline{B}}$, described in frame (x, y, z) and the same point displaced by seakeeping translation and rotation (now located at position $\mathbf{x}$) is given to second order in Equation 2.61. The matrix $\overline{\overline{\mathcal{H}}}$ is a rotation matrix comprised of entries that are quadratic in the linear rotational generalized degrees of freedom, i.e. ξ_4, ξ_5, and ξ_6.

$$\mathbf{x} - \mathbf{X} = \epsilon \left(\boldsymbol{\xi}_T + \boldsymbol{\xi}_R \times \mathbf{X} \right) + \epsilon^2 \overline{\overline{\mathcal{H}}} \mathbf{X} \tag{2.61}$$

$$\overline{\overline{\mathcal{H}}} = \frac{1}{2} \begin{bmatrix} -(\xi_5^2 + \xi_6^2) & 0 & 0 \\ 2\xi_4\xi_5 & -(\xi_4^2 + \xi_6^2) & 0 \\ 2\xi_4\xi_6 & 2\xi_5\xi_6 & -(\xi_4^2 + \xi_5^2) \end{bmatrix} \tag{2.62}$$

In expansion Equation 2.61 it is assumed that the wave-induced seakeeping motions are $\mathcal{O}(\epsilon)$ ($\epsilon \ll 1$) consistent with perturbation expansions used in the hydrodynamic BVP. A similar expansion is made for the unit outward normal vector on the

body, shown in Equation 2.63.

$$\hat{\mathbf{n}} = \hat{\mathbf{N}} + \epsilon \left(\boldsymbol{\xi}_R \times \hat{\mathbf{N}} \right) + \epsilon^2 \overline{\overline{\mathcal{H}}} \hat{\mathbf{N}} \tag{2.63}$$

The term $\mathbf{x} \times \hat{\mathbf{n}}$ is needed on the displaced position of the hull and using Equations 2.61 and 2.63 it is written as:

$$\mathbf{x} \times \hat{\mathbf{n}} = \mathbf{x} \times \hat{\mathbf{N}} + \epsilon \left(\boldsymbol{\xi}_T \times \hat{\mathbf{N}} + \boldsymbol{\xi}_R \times \mathbf{x} \times \hat{\mathbf{N}} \right) + \epsilon^2 \left(\overline{\overline{\mathcal{H}}} \left(\mathbf{x} \times \hat{\mathbf{N}} \right) + \boldsymbol{\xi}_T \times \boldsymbol{\xi}_R \times \hat{\mathbf{N}} \right) \tag{2.64}$$

The generalized normal vector of the displaced hull surface, $(\hat{\mathbf{n}}, \mathbf{x} \times \hat{\mathbf{n}})^T$, is now completely described in the maneuvering coordinate system and the following abbreviated notation is used:

$$\begin{aligned} \begin{Bmatrix} \hat{\mathbf{n}} \\ \mathbf{x} \times \hat{\mathbf{n}} \end{Bmatrix} &= \begin{Bmatrix} \hat{\mathbf{N}} \\ \mathbf{X} \times \hat{\mathbf{N}} \end{Bmatrix} + \epsilon \begin{Bmatrix} \boldsymbol{\xi}_R \times \hat{\mathbf{N}} \\ \boldsymbol{\xi}_T \times \hat{\mathbf{N}} + \boldsymbol{\xi}_R \times \left(\mathbf{X} \times \hat{\mathbf{N}} \right) \end{Bmatrix} + \epsilon^2 \begin{Bmatrix} \overline{\overline{\mathcal{H}}} \hat{\mathbf{N}} \\ \overline{\overline{\mathcal{H}}} \left(\mathbf{X} \times \hat{\mathbf{N}} \right) + \boldsymbol{\xi}_T \times \left(\boldsymbol{\xi}_R \times \hat{\mathbf{N}} \right) \end{Bmatrix} \\ &= \mathbf{n}^{(0)} + \epsilon \, \mathbf{n}^{(1)} + \epsilon^2 \, \mathbf{n}^{(2)} \end{aligned} \tag{2.65}$$

With the perturbation expansions carried out to second-order, the forces are ready for computation. The integrals of pressure are now computed below the calm-water plane on the mean hull surface, $S_{\overline{B}}$, producing the second-order force (moment) on the mean body, $\mathbf{F}^{(2)}_{\text{mb}}$, and a waterline integral is added to capture second-order force (moment) near the waterline, $\mathbf{F}^{(2)}_{\text{wl}}$, as shown in Equation 2.66. The waterline integral incorporates flare angle effects through local flare angle, α; $\alpha = 90^\circ$ at waterline is vertical wall.

$$\begin{Bmatrix} \mathbf{F}^{(2)} \\ \mathbf{M}^{(2)} \end{Bmatrix} = \underbrace{- \iint\limits_{S_{\overline{B}}} p(\mathbf{x}) \begin{Bmatrix} \hat{\mathbf{n}} \\ \mathbf{x} \times \hat{\mathbf{n}} \end{Bmatrix} dS}_{\equiv \mathbf{F}^{(2)}_{\text{mb}}} + \underbrace{\oint\limits_{WL} \int\limits_0^{\zeta} p(\mathbf{x}) \frac{1}{\sin(\alpha)} \begin{Bmatrix} \hat{\mathbf{n}} \\ \mathbf{x} \times \hat{\mathbf{n}} \end{Bmatrix} dz dl}_{\equiv \mathbf{F}^{(2)}_{\text{wl}}} \tag{2.66}$$

The expansions for pressure and position of the hull surface (and unit normal vector) displaced, due to seakeeping motions, about its mean position are inserted into Equation 2.66. The final expression for pressure on the mean body surface is given in Equation 2.67.

$$\begin{aligned}
\frac{\mathbf{F}^{(2)}_{\text{mb}}}{\rho} = &-\iint\limits_{S_{\overline{B}}} \left(\overline{\overline{\mathcal{H}}}\mathbf{x}\cdot\nabla\left(gz - \mathbf{W}\cdot\nabla\Phi + \frac{1}{2}\nabla\Phi\cdot\nabla\Phi\right)\right)\mathbf{n}^{(0)}dS \\
&-\iint\limits_{S_{\overline{B}}} \left((\boldsymbol{\xi}_T + \boldsymbol{\xi}_R\times\mathbf{x})\cdot\nabla\left(\frac{\partial\phi^{(1)}}{\partial t} - \left(\vec{W} - \nabla\Phi\right)\cdot\nabla\phi^{(1)}\right)\right)\mathbf{n}^{(0)}dS \\
&-\iint\limits_{S_{\overline{B}}} \left(\frac{1}{2}\nabla\phi^{(1)}\cdot\nabla\phi^{(1)}\right)\mathbf{n}^{(0)}dS \\
&-\iint\limits_{S_{\overline{B}}} \left((\boldsymbol{\xi}_T + \boldsymbol{\xi}_R\times\mathbf{x})\cdot\nabla\left(gz - \mathbf{W}\cdot\nabla\Phi + \frac{1}{2}\nabla\Phi\cdot\nabla\Phi\right)\right)\mathbf{n}^{(1)}dS \\
&-\iint\limits_{S_{\overline{B}}} \left(\frac{\partial\phi^{(1)}}{\partial t} - (\mathbf{W} - \nabla\Phi)\cdot\nabla\phi^{(1)}\right)\mathbf{n}^{(1)}dS \\
&-\iint\limits_{S_{\overline{B}}} \left(gz - \mathbf{W}\cdot\nabla\Phi + \frac{1}{2}\nabla\Phi\cdot\nabla\Phi\right)\mathbf{n}^{(2)}dS
\end{aligned} \tag{2.67}$$

The expression for the second-order force due to nonlinearity near the waterline is given in Equation 2.68, where $\zeta_{\text{rel}} = \zeta - (\xi_3 + y\xi_4 - x\xi_5)$ is the signed vertical distance between the maximum wetted point on the hull and the calm-water line.

$$\frac{\mathbf{F}^{(2)}_{\text{wl}}}{\rho} = \oint\limits_{WL} \frac{1}{2} g \frac{\zeta^2_{\text{rel}}}{\sin(\alpha)}\mathbf{n}^{(0)}dl - \oint\limits_{WL}\left(-\mathbf{W}\cdot\nabla\Phi + \frac{1}{2}\nabla\Phi\cdot\nabla\Phi\right)\frac{\zeta_{\text{rel}}}{\sin(\alpha)}\mathbf{n}^{(1)}dl \tag{2.68}$$

Equations 2.67-2.68 contain second-order terms computed from first-order potentials. Accordingly, for second-order quantities formed from quadratic terms involving a harmonic first-order potential, a time average of the second-order force over one encounter period produces a non-zero mean value. Moreover, a second-order potential (neglected in this work) has a time average of zero. Time-averaging Equations 2.67-

2.68 produces forces and moments valid to second-order without the necessity to solve for the second-order potential.

The force-averaging process used in this work is now detailed. Due to the slowly-varying maneuvering velocities and ship heading change, the first order velocity potential is not harmonic, though it approximately is. Thus the second order forces approximately vary at twice the wave encounter frequency, as would be the result of second-order forces formed from terms quadratic in first-order harmonic potential. Following this reasoning, the second order force is approximated as a harmonic function in a small time window around the time of interest. The functional form of the harmonic representation of the second-order force is given in Equation 2.69.

$$\mathbf{F}^{(2)}(t) = f_1 \sin(2\omega_e t) + f_2 \cos(2\omega_e t) + \overline{\mathbf{F}^{(2)}} \tag{2.69}$$

The coefficients f_1, f_2, and $\overline{\mathbf{F}^{(2)}}$ are determined by a least-squares solution to a system formed by sampling the second-order force over the preceding one-half wave encounter period. The mean value of the functional fit, $\overline{\mathbf{F}^{(2)}}$, is taken as the mean second-order force at the current time step. A demonstration of this technique applied to the second-order surge force is portrayed in Figure 2.11.

This work also explores the possibility of using the entire second-order force without averaging. If successful, this has direct implications to the extension of this method to irregular sea states. Chapter III and Chapter IV demonstrate that the time-averaging of the force works quite well to remove most wave-encounter frequency from the mean force signal even when the potentials are not harmonic. More importantly, the case studies indicate that usage of the full second-order force (neglecting second-order potential) produces a very comparable result. This could be critical in the simulation of irregular seas where a well-defined time window does not exist for force averaging (Kim et al., 2012).

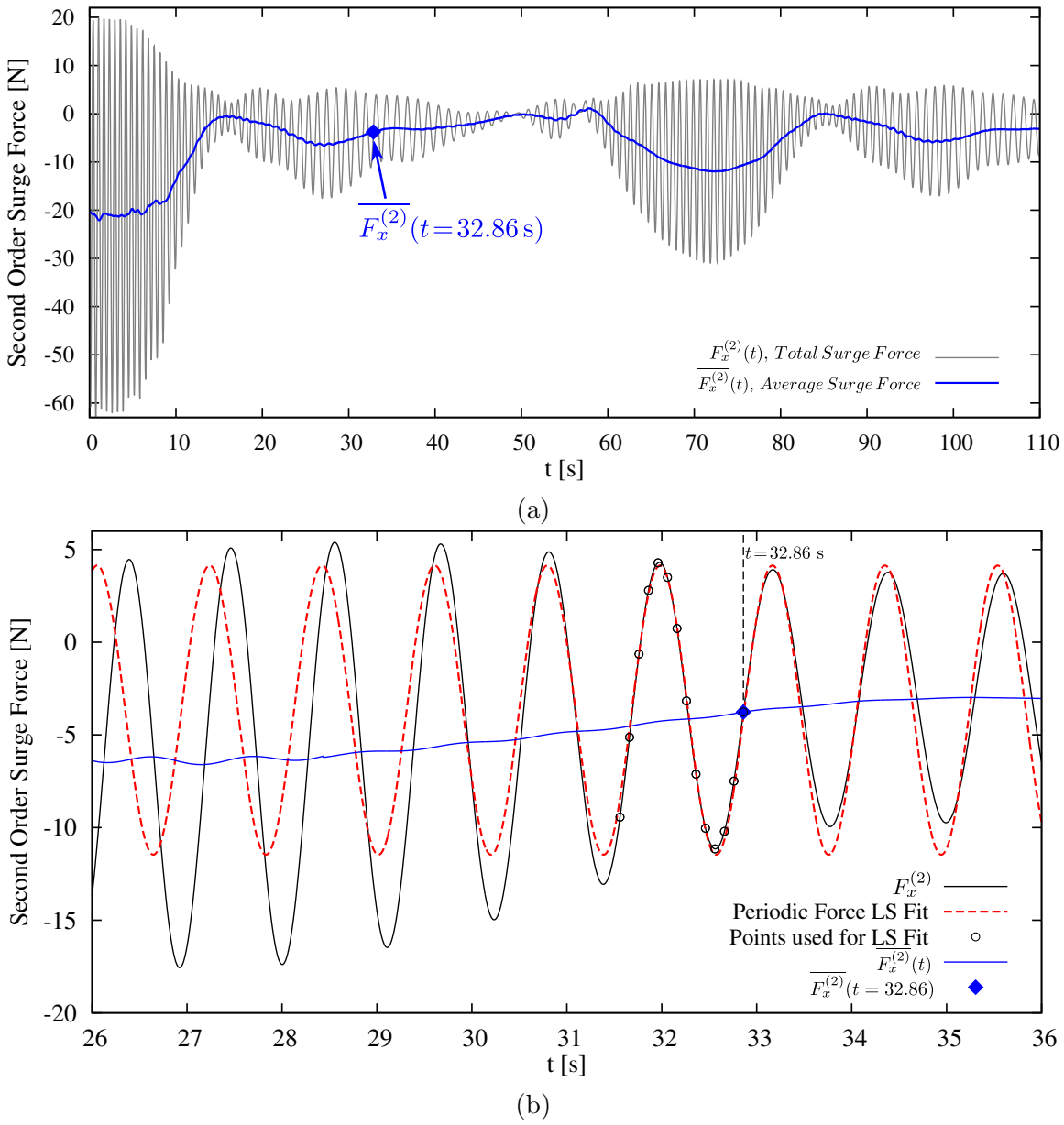

Figure 2.11: (a) Second-order surge force time-series and time-averaged second-order surge force (b) Least-squares fit procedure and resulting time-averaged second-order surge force

2.4.3 Numerical Solution of Boundary Integral Equations

The Boundary Integral Equation (BIE)'s derived in Section 2.4.1 are enforced on a higher-order representation of the geometry. The BEM solver, titled Aegir, is utilized in this work and Aegir interprets geometries in a Non-Uniform Rational B-

Spline (NURBS) format. The ship hull can be represented by one or more NURBS patches. The NURBS surfaces are described in parametric coordinates s, t that have a well-defined one-to-one mapping $(s, t) \rightarrow (x, y, z)$. The velocity potential also utilizes splines as basis functions; in this work third order B-spline basis functions are used to represent the potential. The contributions from B-splines spanning the s and t directions are easily computed as a tensor-product. The velocity potential is represented as in Equation 2.70, where k is the B-spline order and M, N are the number of panels in the s and t directions respectively.

$$\psi(s,t) = \sum_{m=1}^{M+k-1} \sum_{n=1}^{N+k-1} \tilde{\psi}_{mn} S_m(s) T_n(t) \tag{2.70}$$

Despite containing a summation over all panels, the tensor-product representation of the potential requires far fewer summations as the basis functions are chosen to have only local influence. Figure 2.12 shows that a basis function centered on a given panel only has an influence over itself and one neighboring panel to each side; these basis functions are then described as having local support.

This representation of the potential is inserted into the BIE which is enforced at the centroid of each panel, with the unknowns being the spline coefficients, $\tilde{\psi}_{mn}$. This is commonly referred to as a collocation method. Alternatively, the BIE's could be enforced at the geometric centroids of the B-spline basis functions. The B-spline basis functions and the projections of the centroids in s and t are projected onto the panels in Figure 2.12 to demonstrate where the BIE's are enforced.

The BIE's can be satisfied in an integral sense by utilizing a Galerkin approach. The Galerkin approach first performs an "outer" integration at Gauss points across each panel, giving an opportunity to satisfy boundary conditions at the more numerous Gauss-Legendre points. The Galerkin method is utilized in this work and preferred over the collocation method. The size of the linear systems remain the

same in the Galerkin method as in the collocation method.

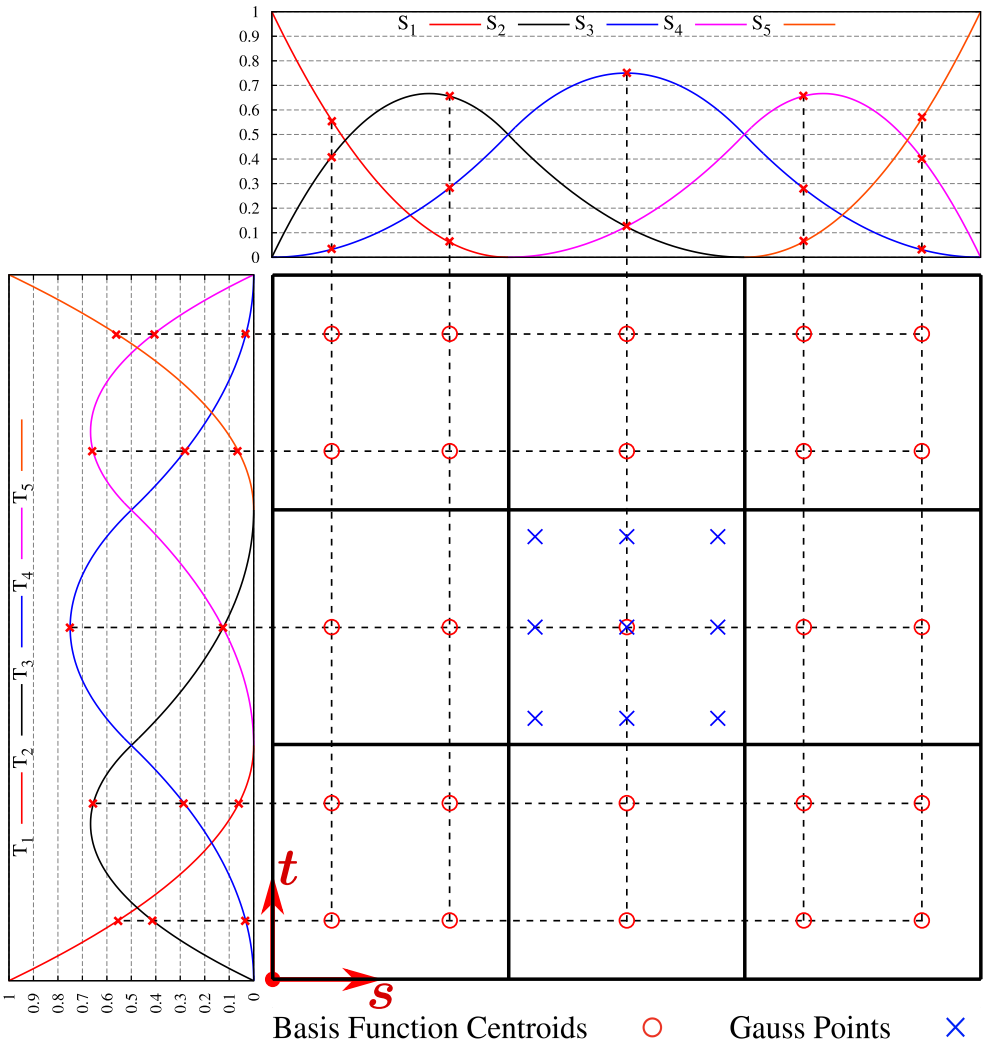

Figure 2.12: A patch subdivided into three panels in parametric s and t directions and supporting basis functions.

2.5 Propulsion Force Model and Rudder Forces

Two propeller models are utilized in this work. The propeller model is a crucial component within the modular hybrid framework. The propeller model allows the discrete propeller and demanding time step requirements to be removed from the CFD. The integral forces are computed as a function of components from the maneuvering state vector. The propeller models built for use in this work predict thrust,

T, side force, S, and torque, Q. Additionally, the side force is assumed to act at the location of the propeller and also produces a moment about the vertical axis in the body-fixed frame. Figure 2.13 displays the modeled forces and conventions.

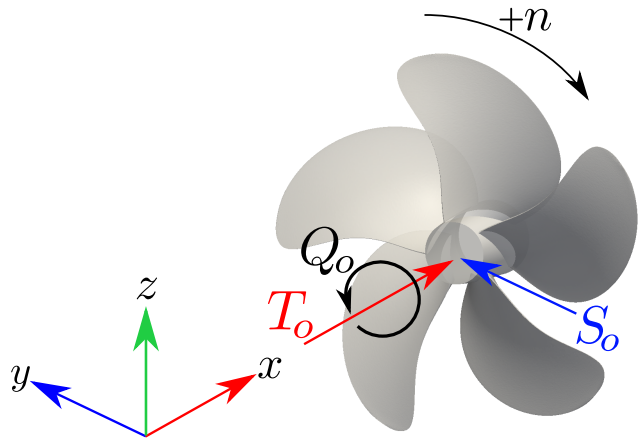

Figure 2.13: Propeller forces predicted by surrogate model

The propeller model takes the maneuvering state vector as input. The model built for use with the DTC hull in Chapter III is constructed using a series of linear least-squares regressions on pre-computed CFD containing a discretized propeller Knight and Maki (2018). The model is extended by Knight to include sway motion and its effects on propeller forces and tested in (White et al., 2019).

The model built for the KCS test case in Chapter IV is constructed using nonlinear regression techniques. The KCS propeller model also uses a larger parameter vector and more complex functional form than the DTC propeller model. The construction of the model is described in Knight and Maki (2020).

The propeller effect on the fluid introduced via a momentum source disk using the distribution found in Hoekstra (2006). The propeller loading in the Hoekstra model is axisymmetric and thus assumes straight inflow. In CFD applications, this model can be used in the wave of a ship but cannot predict effects due to oblique inflow. The propeller loading and momentum imparted to the fluid is considerably different under non-uniform or oblique inflow but is not accounted for in this work.

The discretized rudder is included in the CFD analysis in this work. The rudder

forces are derived from integrals of pressure and viscous stress over the discrete rudder surface. The motion of the rudder is enable through use of an Arbitrary Mesh Interface (AMI) within the OpenFOAM CFD solver. The AMI implementation in OpenFOAM uses the methods found in Farrell and Maddison (2011) for efficient computation of fluxes across non-matching mesh surfaces. The geometry of the stern region of the Duisburg Test Case (DTC) hull is shown in Figure 2.14 with the AMI region shown in its rotated position for a 35° rudder angle.

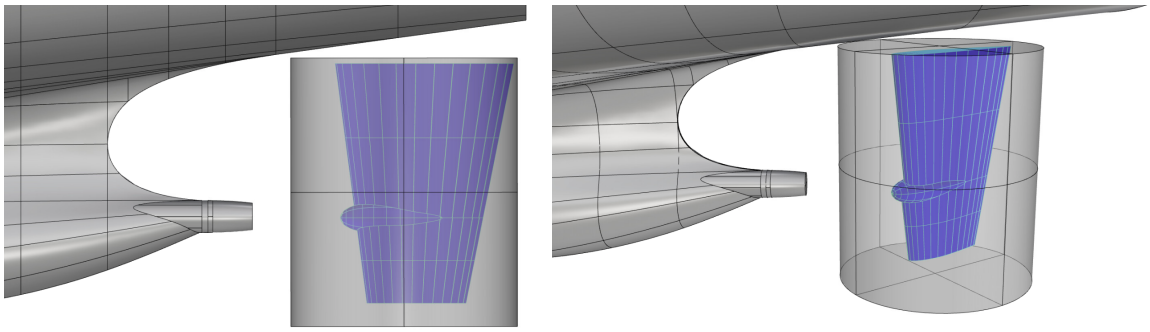

(a) (b)

Figure 2.14: (a) Profile view of DTC stern and spade rudder with Costa bulb ($\delta = 0°$) (b) DTC rudder within Arbitrary Mesh Interface (AMI) zone rotated $\delta = 35°$

CHAPTER III

Numerical Test Case 1: Duisburg Test Case

This chapter presents one of two numerical test cases selected to evaluate the validity and performance of the proposed hybrid method for prediction of combined manuevering and seakeeping motion. Before testing the hybrid method in a combined maneuvering and seakeeping simulation, several less complex problems are first examined. The hybrid method is benchmarked against higher-fidelity results generated with the fully nonlinear Volume-of-Fluid (VOF) method, which are considered to be the target solution for computations where experimental results are not available. First, the performance of the VOF method and the linear time-domain BEM are tested to predict ship seakeeping motions on a fixed course in regular head seas. The next preliminary step is to test the assumptions behind the hybrid method in a maneuvering problem in calm water. Finally, the hybrid method is compared against the results generated with VOF in the simulation of the Duisburg Test Case (DTC) hull turning in regular waves.

3.1 Seakeeping Validation

Seakeeping computations are made to demonstrate the capability of both the VOF method and the BEM to accurately predict ship motions on a fixed course. The seakeeping response of the vessel is an integral component of predicting the motion

of a ship executing a maneuver while being subject to wave-induced loads, and so the wave-induced response is tested in isolation from a maneuver. When using the VOF method to solve for the motions of a ship making a maneuver in waves, the seakeeping motions are implicitly included in the total nonlinear dynamical response of the ship. Moreover, to understand the ability of the VOF method to predict vertical plane motions, it is instructional to simplify the problem to investigate heave and pitch motions at constant speed into regular head waves. This also provides an opportunity to compare predictions made with the linear potential-flow approach.

The test case selected for the following seakeeping computations (and ensuing maneuvering computations) utilizes the Duisburg Test Case (DTC) hull form, pictured in Figure 3.1(a) and whose main particulars are provided in Table 3.1. The design of this Post-Panamax container ship was developed at the University of Duisburg-Essen, Duisburg, Germany for the purpose of creating a benchmark for validation of numerical methods. For more details about the creation of the DTC hull and some of the experimental measurements, refer to the work of el Moctar et al. (2012).

Table 3.1: Main particulars of the DTC hull

Main Particular (Full Scale)	Value
L	355 m
Beam	51 m
T	14.5 m
Displacement	$173,468$ m^3
Wetted Surface Area, S_w	$22,032$ m^2
C_B	0.661
LCG (+ fwd. of AP)	174.3 m
Rudder Area, S_{rud}	255 m^2
Design Speed	24 knots
Propeller Diameter	8.911 m
Number of Blades	5

The finite volume mesh utilized in the seakeeping study are identical to the meshes utilized in all maneuvering simulations. The meshes were designed with resolution requirements in mind to capture converged pressure and viscous forces on the hull

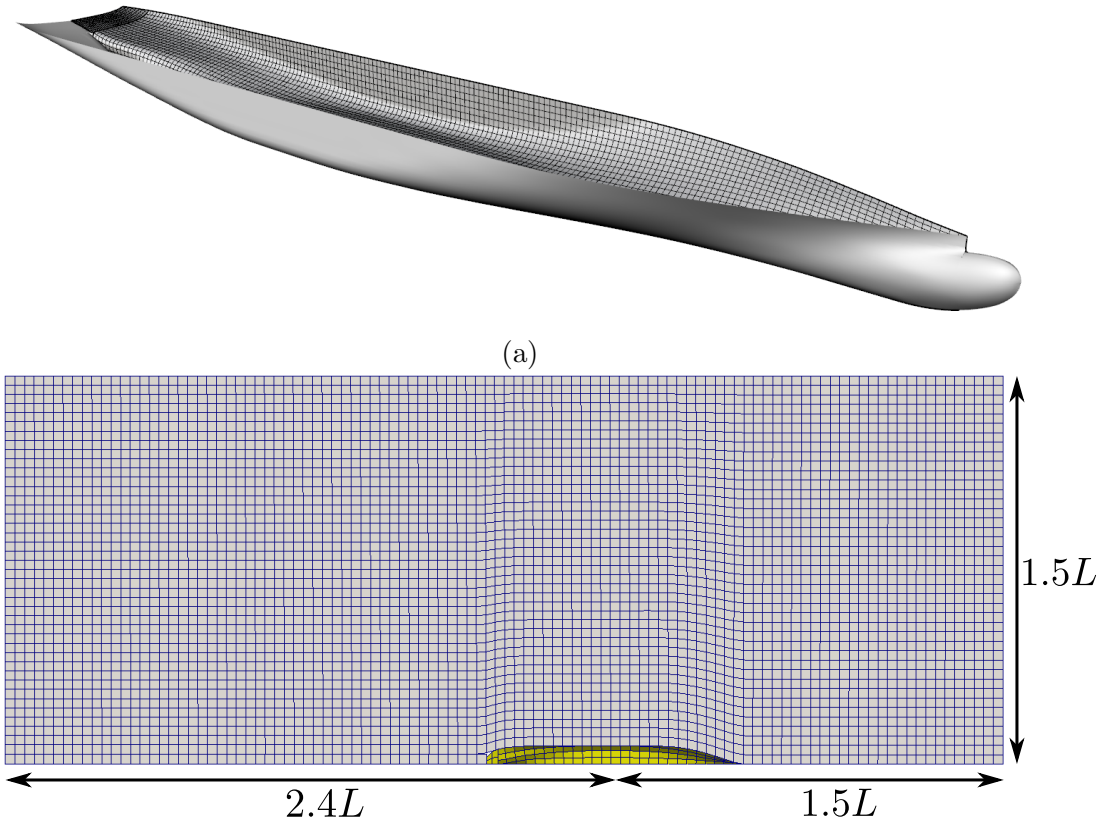

Figure 3.1: (a) Portion of rendered DTC hull surface (starboard side) and NURBS representation (port side) (b) Free surface and hull hydrodynamic panelization of Aegir mesh

and rudder surfaces as well as mesh resolution to accurately propagate a numerical wave across the finite volume domain. Appendix A addresses the mesh topology, the wave generation method, and mesh resolution requirements without the ship and rudder present. Fifth-order Stokes waves (Fenton, 1985) are generated throughout a cylindrical relaxation zone through addition of source terms in the momentum and phase fraction equations.

Seakeeping computations are made on mesh D2 from Appendix A. Due to satisfactory results and limited time and computational resources, no computations were performed on mesh D3. With the ship and rudder discretized, mesh D2 contains 4,125,692 finite volume cells and has an average y^+ value of approximately $y^+ = 50$

in the seakeeping computations. The dimensions of the CFD domain are shown in Figure 3.2. The mesh for all BEM simulations featuring the DTC hull is pictured in Figure 3.1(b) and the BEM mesh parameters are summarized in Table 3.2.

Table 3.2: BEM mesh parameters for DTC simulations

Patch Group:	# of panels
Free Surface	8420
Hull Surface	268

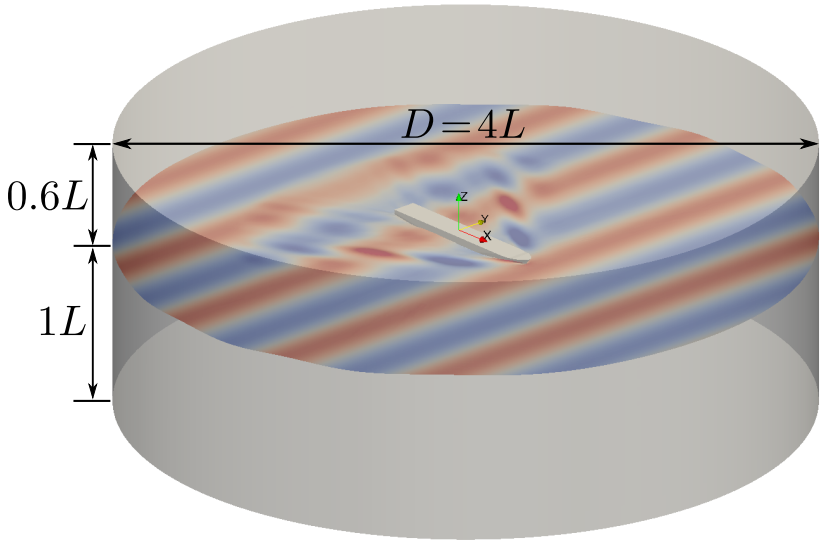

Figure 3.2: Dimensions of CFD domain for DTC simulations

The wave conditions and Froude number ($Fn = 0.14$) for this series of numerical validation tests are selected from a subset of tests completed under the Energy Efficient Safe Ship Operation (SHOPERA) project at MARINTEK. Details of the experimental setup and results can be obtained from Lyu and el Moctar (2017) and el Moctar et al. (2016). The wave conditions that are simulated in this seakeeping assessment are summarized in Table 3.3. In Table 3.3, λ is the wave length, k is the wave number, T is the wave period, $k\zeta_I$ is the wave steepness, H is the wave height, and L is the ship length.

The model is towed by a carriage in the MARINTEK facility and is moored within a diamond-shaped soft-spring arrangement. The mooring apparatus serves

Table 3.3: Wave conditions for DTC seakeeping simulations, ($Fn = 0.14$)

λ/L	λ [m]	H [m]	T [s]	$k\zeta_I$
0.44	2.454	0.049	1.254	0.063
0.80	4.462	0.089	1.691	0.063
0.91	5.057	0.102	1.803	0.063
1.00	5.577	0.112	1.890	0.063
1.09	6.079	0.122	1.974	0.063
1.40	7.808	0.156	2.237	0.063

the purpose of minimizing yaw and roll motions while maintaining target speed and minimally affecting heave and pitch degrees of freedom. The mooring arrangement is also fitted with force transducers to measure forces acting on the model. As a result of the mooring arrangement, the DTC model in the added resistance tests has slightly different inertia properties than in the low-Froude number free-running tests in the SHOPERA program. For the purposes of this study, it is assumed that extra mass and rotational inertia (from the mooring arrangement) are included in the inertia properties listed in Lyu and el Moctar (2017) and el Moctar et al. (2016). The physical properties used in the computations in this section are provided in Table 3.4.

Table 3.4: Inertia properties for DTC model

Property	Value (Model Scale)
m	672.70 kg
r_{xx}	0.32 m
r_{yy}	1.40 m
r_{zz}	1.40 m
LCG (+ fwd. of midship)	-0.05 m
VCG (+ abv. keel)	0.38 m

The motions from the seakeeping simulations are recorded and presented in Figure 3.3 in the form of a Response Amplitude Operator (RAO). The motions computed here with the VOF method and linear time-domain BEM (Aegir) are plotted with the physical model tests and a high-order frequency domain BEM code titled GL

Rankine (Lyu and el Moctar, 2017; Söding et al., 2014).

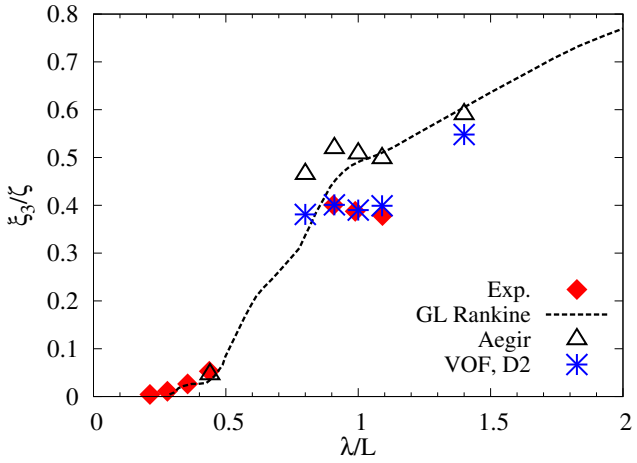

(a)

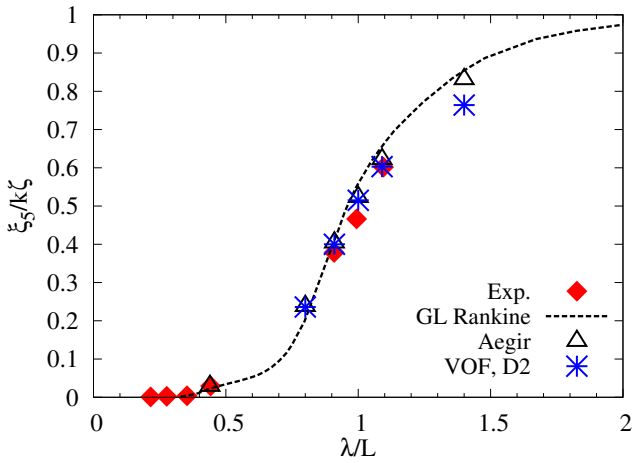

(b)

Figure 3.3: (a) Heave RAO for DTC, $Fn = 0.14$ (b) Pitch RAO for DTC, $Fn = 0.14$. Experimental values and GL Rankine results from Lyu and el Moctar (2017)

The computed VOF results generally agree well with the experimental values. This study did not attempt to compute short wavelengths with the VOF method due to the stringent discretization requirements necessary to resolve very short waves. However, the BEM calculations are computed at one shorter wavelength of $\lambda/L = 0.44$ and heave response agrees well with experiment, though pitch is underpredicted.

Deviations are seen between the results computed with Aegir and the BEM results from Lyu and el Moctar (2017). The shape of the heave RAO is noticeably less peaked

from the frequency domain computation with GL Rankine, whereas the BEM result computed with Aegir takes the same shape as VOF and experiment. The two sets of BEM results do share the common feature of overpredicting heave through the $\lambda/L = 1$ wavelength regime, both overpredicting VOF and experiment by approximately 25%. The pitch response agrees well between all methods and the experimental values for all wavelengths.

The added resistance is computed according to Equation 3.1. The calm-water resistance, R_{cw}, is subtracted from the time-averaged surge force over p encounter periods, T_e. As an example, Figure 3.4 shows the time-averaged surge force over $p = 8$ encounter periods.

$$\begin{aligned} R_{\text{A}} &\equiv \frac{1}{pT_e}\int_{t}^{t+pT_e} F_x dt - R_{\text{cw}} \\ C_x &\equiv \frac{R_{\text{A}}}{\rho g {\zeta_I}^2 B^2/L} \end{aligned} \tag{3.1}$$

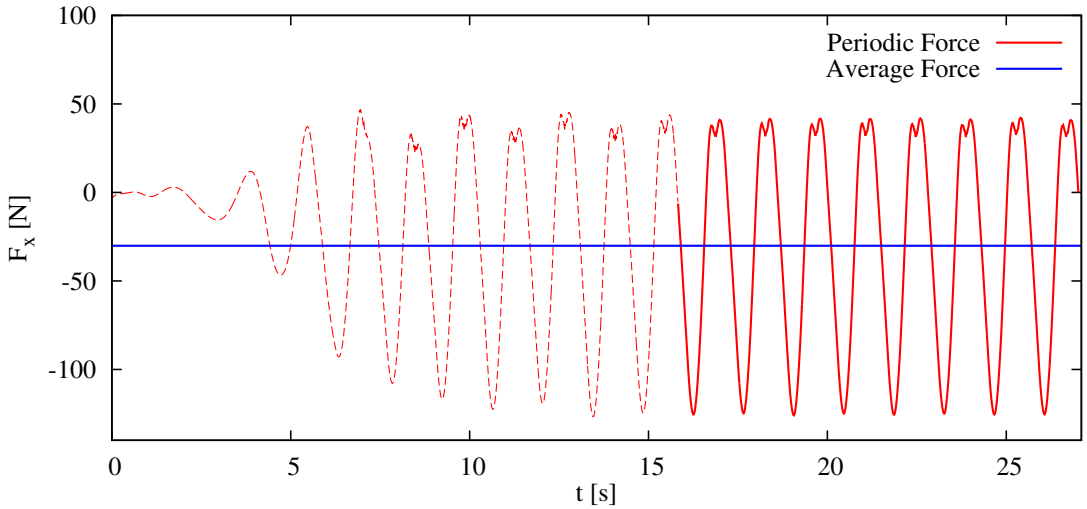

Figure 3.4: Time-averaged surge force on DTC hull from VOF method computations, $\lambda/L = 1.0$

The peaks of the computed added resistance RAO's (featured in Figure 3.5), from both VOF and Aegir, are shifted to a slightly shorter wavelength relative to the peak of the computed added resistance RAO. This result is similar to the results computed

with a RANS VOF method in Chillcce and el Moctar (2018), where the authors also found the peak of the added resistance RAO to be closer to $\lambda/L = 0.9$.

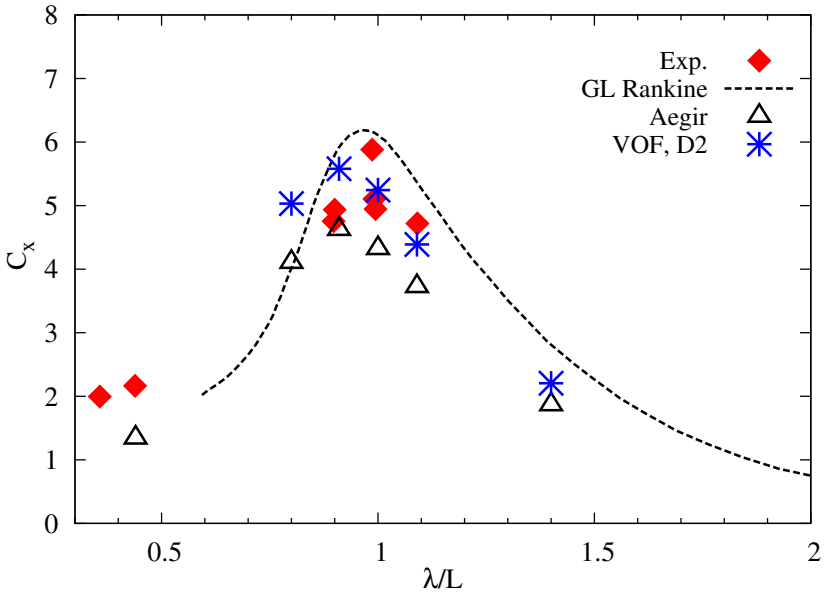

Figure 3.5: Added resistance RAO for DTC, $Fn = 0.14$. Experimental values and GL Rankine results from Lyu and el Moctar (2017)

The maximum added resistance coefficient computed by the VOF agrees with the range of experimental values, which show some variation when repeatability experimental cases were performed. The shape of the added resistance RAO computed with Aegir compares well with the VOF results but underpredicts by approximately 20% in relation to results produced with the VOF method across all wavelengths.

3.2 Calm Water Turning Circle Prediction

A turning circle is predicted in calm water before regular waves are introduced. The details of the maneuver are provided below in Table 3.5. The computational model is ramped to the target speed in rectilinear motion. The velocity is specified as a half-cosine curve over a ramp period of $t_r = 8$ s. The initial ramp period is followed by an additional 4 s over which the forward speed is held at the constant target speed. In total, the surge degree of freedom is held constant for 12 s during

which time the ship is permitted to travel over two ship lengths so that the flow field may develop. Although the surge degree of freedom is prescribed and sway and yaw are restricted during the initial ramp, dynamic sinkage and trim are computed throughout the semi-captive ramp phase in the VOF method.

Table 3.5: Maneuver details for DTC calm-water turning circle prediction

Maneuver Details (Model Scale)	Value
Initial Speed	1.48 m/s
Initial Froude Number	0.2
Rudder Angle, δ	$+35^\circ$
Propeller Model Rev. Rate, n	15.7 rps
Rudder Rate	$18^\circ/s$

Rather than implement a propeller controller, the model self-propulsion point is computed before completing the turning circle tests. A propeller revolution rate of $n = 15.7$ rps allows the propeller model to produce enough thrust in calm water to reach a self-propulsive equilibrium state. The propeller revolution rate in the model is slightly higher than prescribed revolution rate of the discretized propeller in the CFD. However, the revolution rate given to the model was within 2% of the rate used in performing the CFD to train the model.

Table 3.6: Mesh parameters for DTC turning circle simulations

	D1	D2	D2R
# of cells, VOF Domain	1,521,838	4,125,692	7,062,240
# of cells, Hybrid Domain	865,201	2,281,234	N/A
Avg. y^+	45	34	35

This concludes the description of the simulation setup and initial conditions before the maneuver is executed. In the VOF and hybrid method simulations the models were freed at $t = 12$ s, simultaneously with the start of rudder motion. All six degrees of freedom are freed in the VOF method whereas sway and yaw were freed in the hybrid method, continuing to restrict the hybrid method to the horizontal plane. The rudder in each of the simulations begins to rotate to the maximum rudder angle

of $+35^\circ$ at $18^\circ/$ s and the rudder movement is completed in 1.94 s. The rudder motion is handled within the CFD via the sliding mesh technique described in Section 2.5.

Figure 3.6 shows computations using the VOF method on the D1 and D2 meshes as well as the results computed with the hybrid method on the D2 mesh; the D2 mesh for the hybrid method is identical to the D2 VOF mesh but with $z > 0$ truncated. The mesh details and y^+ estimates for each mesh are measured in the quasi-steady phase of the turn (after initial forward speed loss) and are listed in Table 3.6. The hybrid method in calm water reduces to running a three degree of freedom (surge, sway, and yaw) single-phase RANS simulation with a symmetry-plane boundary condition for all field quantities on the $z = 0$ plane. The steady wave resistance is precomputed at $Fn = 0.2$, and the wave resistance is linearly interpolated between Froude numbers of 0 and 0.2. In the calm-water hybrid method, the steady wave resistance is added to the thrust from the propeller model and forces on the hull and rudder derived from double-body RANS to create the total force vector. The numerical test cases in this work are selected, in part, to identify a class of maneuvering problems where sway force and yaw moment due to the steady wave can be neglected. Appendix B summarizes a numerical study that supports the assumption of neglecting steady sway and yaw wave forces in the low-frequency maneuvering equations. Ultimately, the computations comparing the VOF method and the hybrid method seek to further validate this assumption.

The trajectories between the VOF and hybrid method agree very well, with little variation from mesh D1 to D2. The VOF turning diameter on D2 is within 2% of the diameter predicted by the hybrid method. The deviation between the VOF trajectory and the hybrid method trajectory on mesh D2 is always less than $0.09L$.

The forward speed, U, and slip speed, V, are plotted in Figure 3.7. The speeds from the hybrid method are given in the maneuvering frame of reference. The speeds from the VOF method are transformed from the body-fixed frame into the horizontal

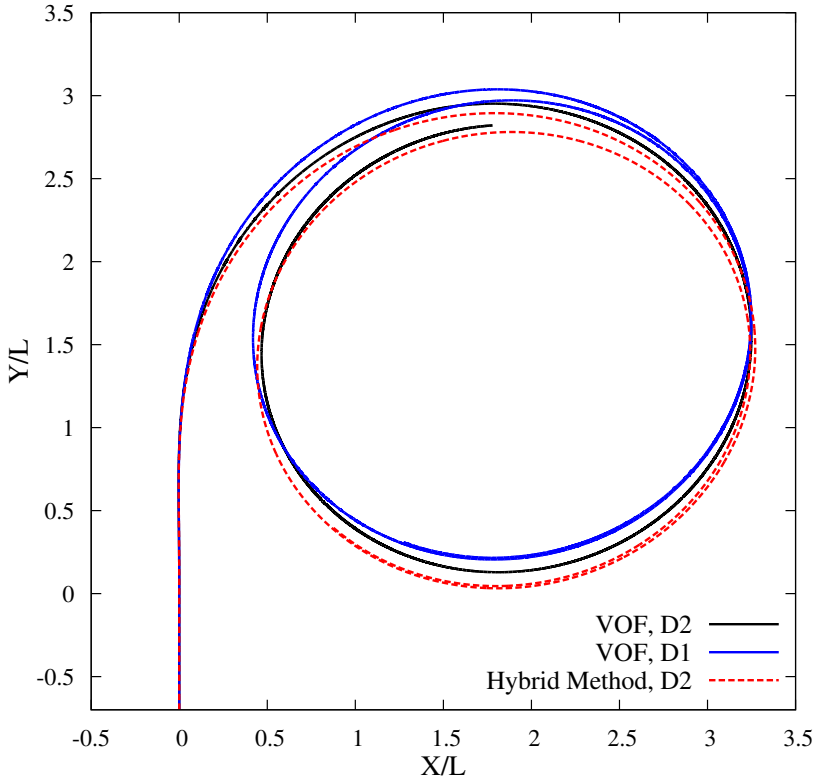

Figure 3.6: DTC calm-water turning circle trajectories computed using nonlinear VOF method and hybrid method

plane. In this way, the speeds presented in Figure 3.7 are all measured in the horizontal plane and a consistent comparison can be made between the two numerical methods.

The velocities of the center of gravity in the horizontal plane are almost indistinguishable between the two methods. The results from the hybrid method show a more rapid forward speed loss than in the VOF results. In addition, the hybrid method has a marginally larger slip speed. These deviations occur due to the simplifying assumptions of neglecting roll and pitch in the hybrid method. However, the results are still satisfactory. This supports the hypotheses that are tested in Appendix B, namely that for this type of hull form and Froude number the hydrodynamic forces are nearly independent of angular rates $\dot{p}$ and $\dot{q}$ and roll and pitch angles Φ and Θ.

The insensitivity to roll and pitch rate and rotation may not hold for all Froude

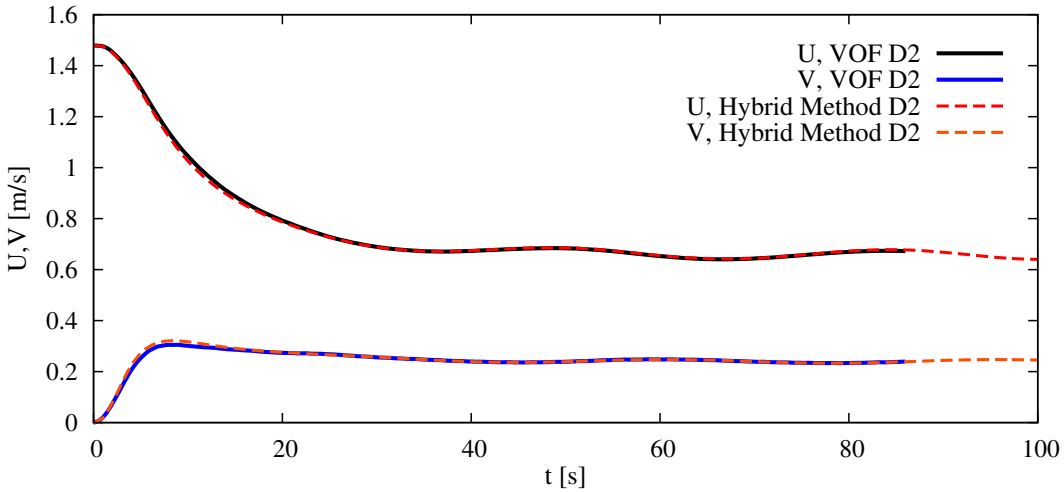

Figure 3.7: VOF and hybrid method forward and slip speed during DTC calm-water turning circle

numbers but a closer look at the roll rotation in Figure 3.8 from the VOF method reveals that a maximum roll of only 2° is reached in the early part of the maneuver. The roll reaches a quasi-steady equilibrium roll angle of around 1°. The DTC hull was originally fitted with bilge keels but none are included in the simulations. Discretizing the bilge keels or increasing near-wall resolution should aid in damping the small roll oscillation that persists throughout the maneuver.

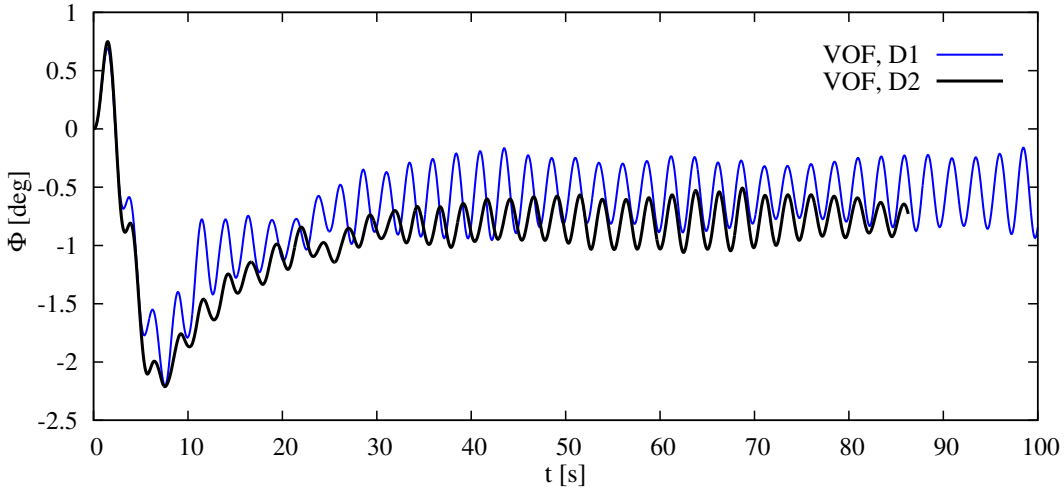

Figure 3.8: Roll predicted by VOF simulations during DTC calm-water turning circle

Investigating the time evolution of heading, the two methods agree well for the

entire maneuver. A small deviation in heading eventually is witnessed after one turning circle is complete, around $t = 80$ s, where the VOF method exhibits a marginally larger yaw rate than the hybrid method.

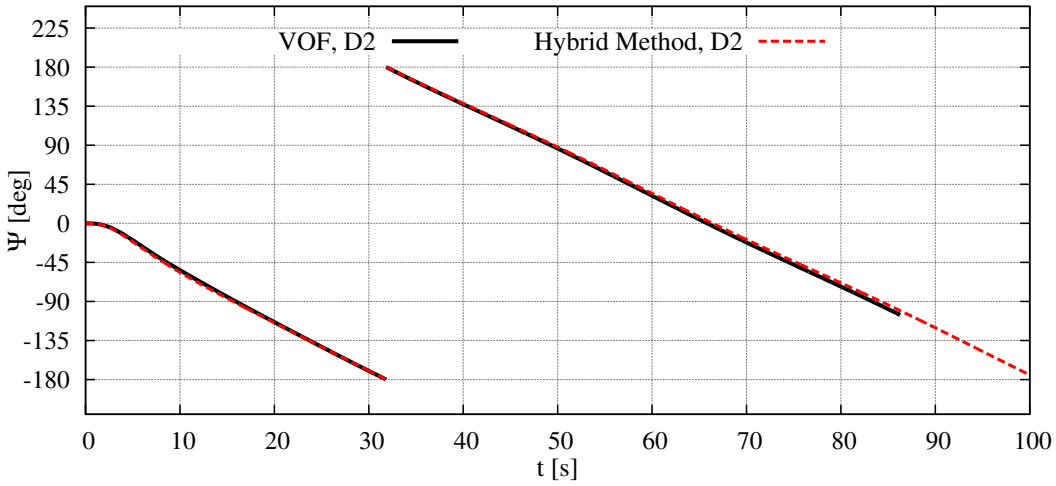

Figure 3.9: Heading angle predicted by VOF and hybrid method during DTC calm-water maneuver

3.3 Turning Circle Prediction In Regular Waves

The computational setup and initial conditions are similar to the setup for the calm-water simulations with some details of the maneuver listed in Table 3.7. One notable difference in all computations in waves is that the vessel is not in a self-propulsive state of equilibrium because the propeller revolution rate from calm-water cases is utilized.

Some inconsistencies arise purely from the challenge of comparing the two numerical approaches on equal grounds. The solution procedure in the following analyses aimed to create as similar of initial conditions as possible for the two methods, even though the computational models were held in a semi-captive state in order to do so. Including a propeller model that offered similar propulsive performance in each of the two methods took precedence over achieving a self-propulsive state in each of the methods.

Table 3.7: Maneuver details for DTC turning circle prediction in waves

Maneuver Details (Model Scale)	Value
Initial Speed	1.48 m/s
Initial Froude Number	0.2
Rudder Angle, δ	$+35°$
Propeller Rev. Rate, n	15.7 rps
Rudder Rate	$18°/s$
Incident Wave Amplitude, ζ_I	0.056 m
λ/L	1.0
ω_0	3.324 rad/s

Two possible choices existed for initial conditions in the VOF and hybrid method setups. The first option is to find the model self-propulsion point in head seas for each of the two different methods individually by adjusting the revolution rate prescribed in the propeller model, meanwhile acknowledging that added resistance predicted by the VOF method and by the BEM are likely different. The second procedure, which is ultimately selected herein, is to utilize the same propeller revolution rate in both methods and release the surge, sway, roll, and yaw degrees of freedom simultaneously with rudder activation. The choice for propeller revolution rate could be selected either from a self-propulsion simulation made with the hybrid method, or from the VOF method. The following analysis took a further simplification of applying the revolution rate derived from the self-propulsion test with propeller model in calm water.

The trajectories computed using each of the two methods on both D1 and D2 meshes are featured in Figure 3.10. As an alternative to simulating on mesh D3, a third mesh titled D2R (mesh details in Table A.1) was created to test convergence with respect to vertical mesh resolution. The D2R mesh contains the same vertical resolution as D3 in Appendix A while having the same lateral distribution of cells as mesh D2. The increase in vertical resolution produced results very similar to those on mesh D2 using the VOF method.

The trajectories computed using the hybrid method in Figure 3.10 utilize different

meshes for the RANS part of the method while using identical boundary element discretizations. The deviations between trajectories using the hybrid method on mesh D1 and mesh D2 then are not purely attributed to discretization error within the RANS but also are a function of the coupling between the higher-order wave forces and the CFD.

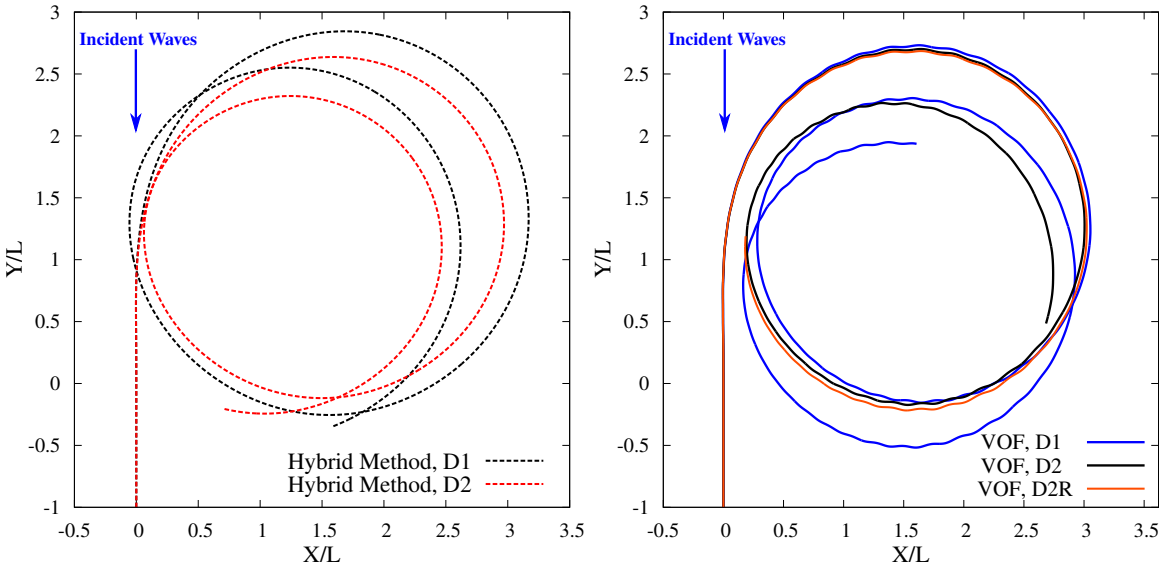

Figure 3.10: (a) Hybrid method turning circle trajectories in waves on D1 and D2 meshes (b) VOF method turning circle trajectories in waves on D1, D2, and D2R meshes

Figure 3.11 displays the computed trajectories using the hybrid method and the VOF method on mesh D2. Figure 3.11 features waypoints at 20 s intervals beginning at $t = 0$ s when the rudder is executed at the origin. The two approaches yield excellent quantitative agreement through the first 270° of the maneuver. After a heading change of 270° the two methods continue to show similar qualitative agreement. The VOF solution is only computed to $t = 111$ s and markers are placed at $t = 110$ s for both methods to compare their endpoints. The endpoints are separated by less than $0.5L$, so while the trajectories are qualitatively similar, small errors compound over the extent of the total simulation time.

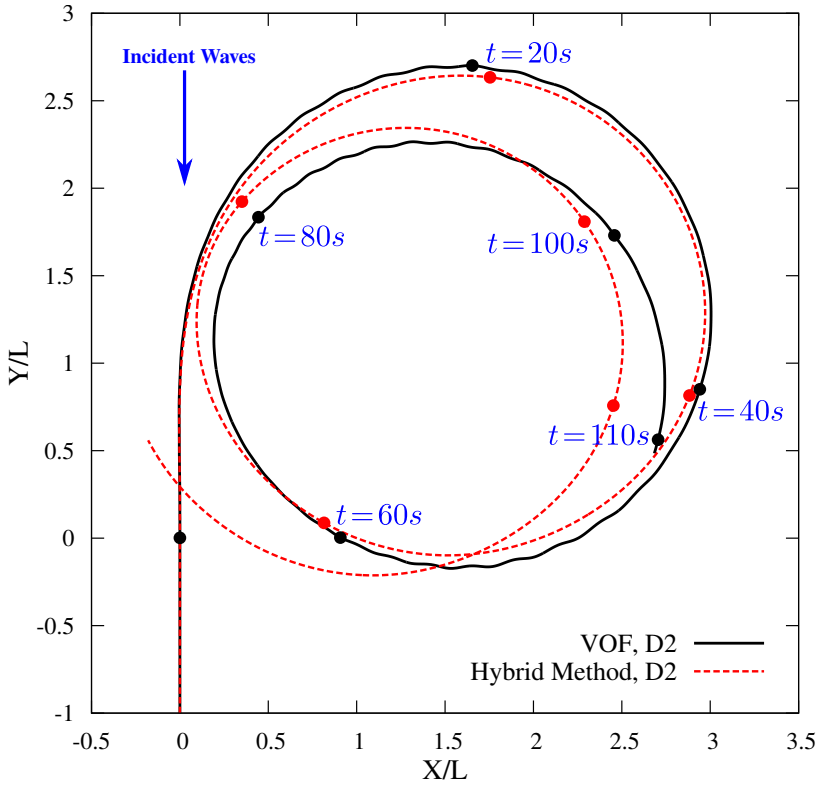

Figure 3.11: DTC turning circle trajectories (Fn = 0.2) in waves computed using nonlinear VOF method and hybrid method

Deviations between trajectories are accompanied by corresponding differences in maneuvering state vectors. Investigation of components of the vessel's state vector offers physical insight into the differences in maneuvering behavior when using the hybrid method versus the VOF method. To compare the VOF results to the hybrid method, the velocities in the ship-fixed frame are transformed back into the horizontal plane, i.e. the maneuvering frame used in the hybrid method. The yaw rate and heading angle are synonymous between both methods as a 3-2-1 Euler angle convention was adopted for the nonlinear dynamics in the VOF method. Furthermore, the VOF results implicitly contain fluctuating velocities at the wave encounter period whereas the maneuvering velocities in the hybrid formulation can be separated from wave induced velocities through the two-time-scale assumption. Thus, to compare the maneuvering velocity from the hybrid method against the VOF, the following VOF data should be interpreted as a mean plus a fluctuation.

The forward speed in the horizontal plane is shown in Figure 3.12. The hybrid method experiences a greater slow down than the VOF. The time windows where the hybrid method underpredicts forward speed relative to the VOF correspond to when the ship is traveling in following seas.

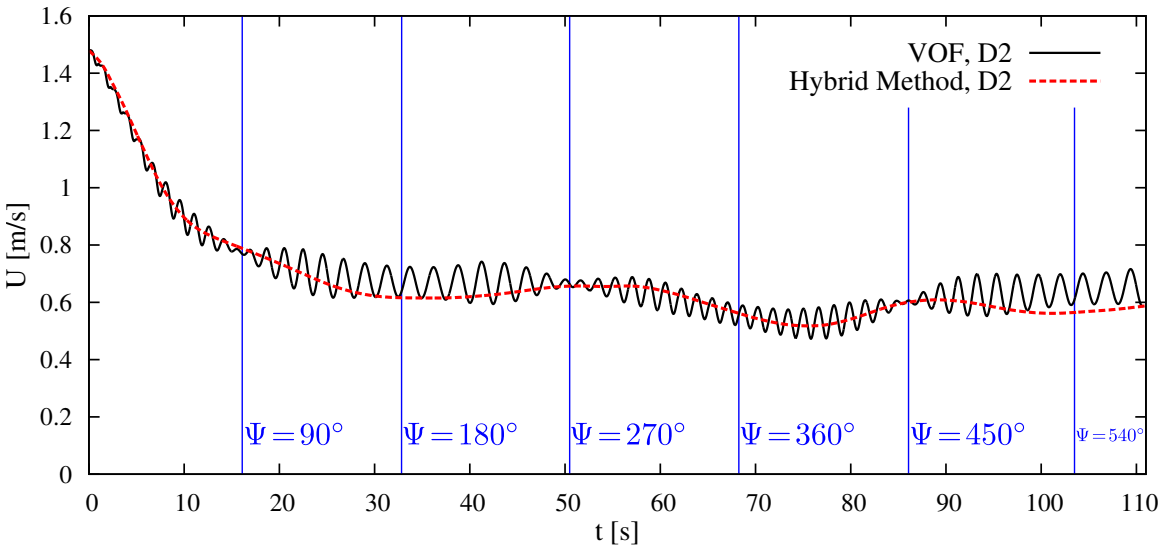

Figure 3.12: VOF and hybrid method forward speed of DTC turning in waves

During the same time windows when the hybrid method underpredicts forward speed relative to VOF, the hybrid method tends to overpredict slip speed (see Figure 3.13). These two effects combined can be summarized together by inspecting the drift angle in Figure 3.14 where the angle is overpredicted by the hybrid method in following seas. The deviation is greatest as the ship turns out of beam seas into stern quartering seas as in the 90° → 180° and 450° → 540° windows. The deviation between the hybrid method drift angle and the mean drift angle from the VOF simulations is at largest a few degrees.

The yaw rates from the two methods are shown in Figure 3.15. The hybrid method predicts a slightly greater yaw rate than VOF when turning out of head seas, through beam quartering sea and into a beam sea condition. The hybrid method shows a marginally slower yaw rate in the following seas through its turn back into head seas (180° → 360°). Overall the differences in yaw rate are small, and the over-

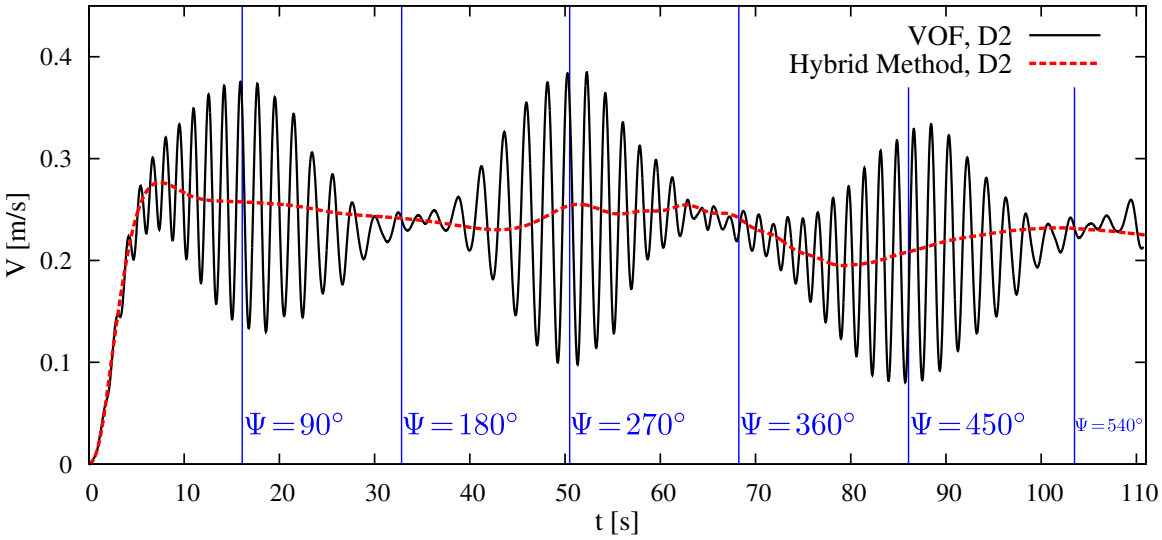

Figure 3.13: VOF and hybrid method sway velocity of DTC turning in waves

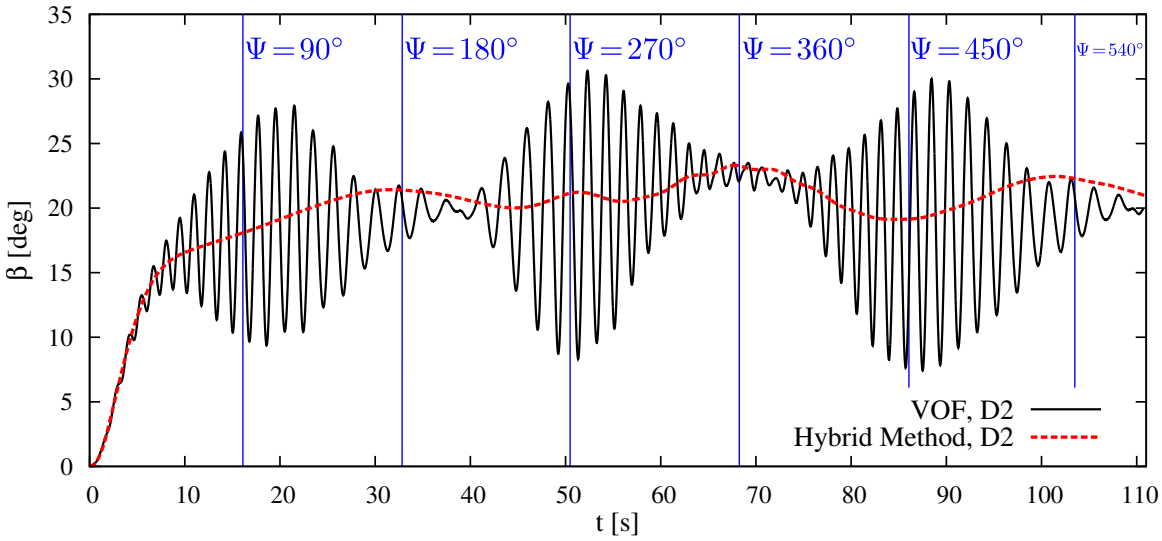

Figure 3.14: VOF and hybrid method drift angle of DTC turning in waves

and under-shoots in the hybrid method relative to VOF balance out when yaw rate is integrated to yield ship heading. Figure 3.16 displays some lead in heading from the hybrid method, but the VOF eventually regains heading to match the hybrid method.

Next, forces are investigated to attempt to gain an explanation for differences in the state vector. The total force is reconstructed in the hybrid method to make an equal comparison with the VOF results. Emphasis is stressed that although the total force is reconstructed for comparison, only the forces with nonzero time-average values

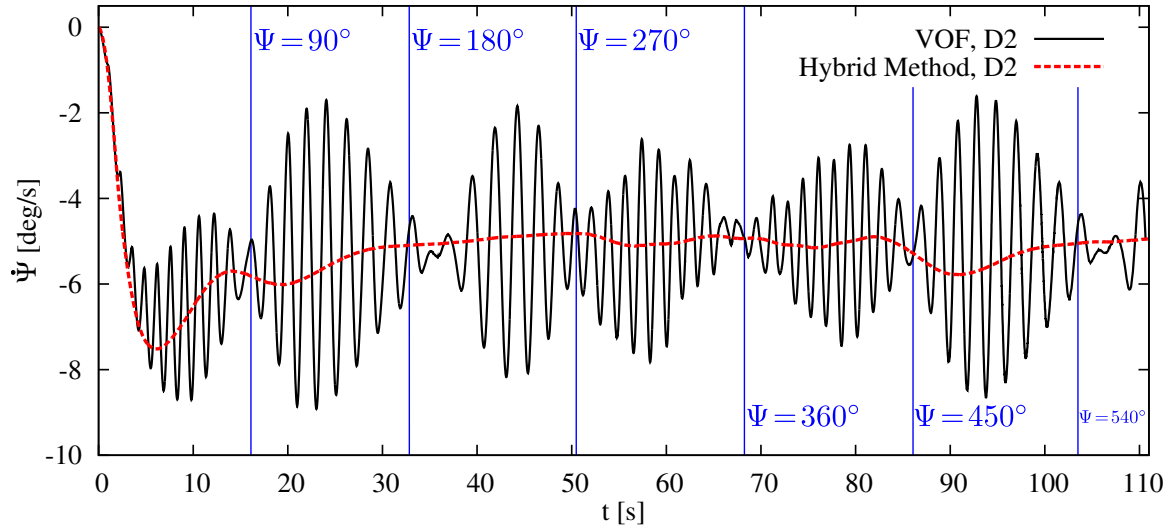

Figure 3.15: VOF and hybrid method yaw rate for DTC turning in waves

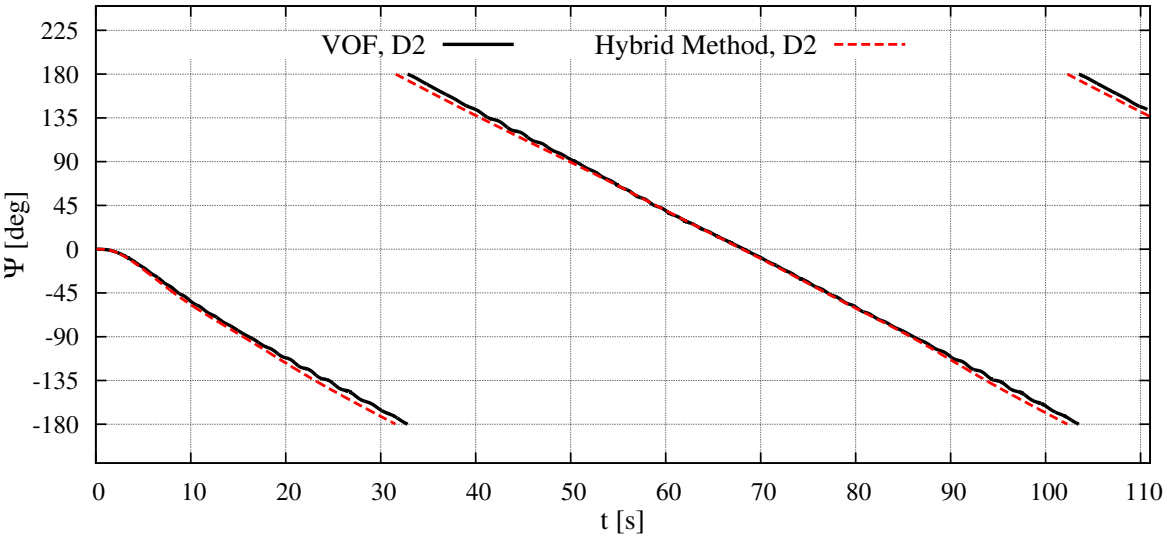

Figure 3.16: Heading angle predicted by VOF and hybrid method for DTC turning in waves

are included in the forcing for the maneuvering equations of motion as described in Section 2.2. Thus, the following discussion relates to the force envelopes, realizing that the first-order wave radiation and diffraction forces produce zero mean value.

Figures 3.17-3.19 display the surge force, sway force, and yaw moment respectively - each plot showing the total force in the VOF method and the hybrid method. The surge force (hydrodynamic force neglecting thrust from propeller model) has a marginally larger (negative) mean value for $t < 5$ s but the surge force envelope is

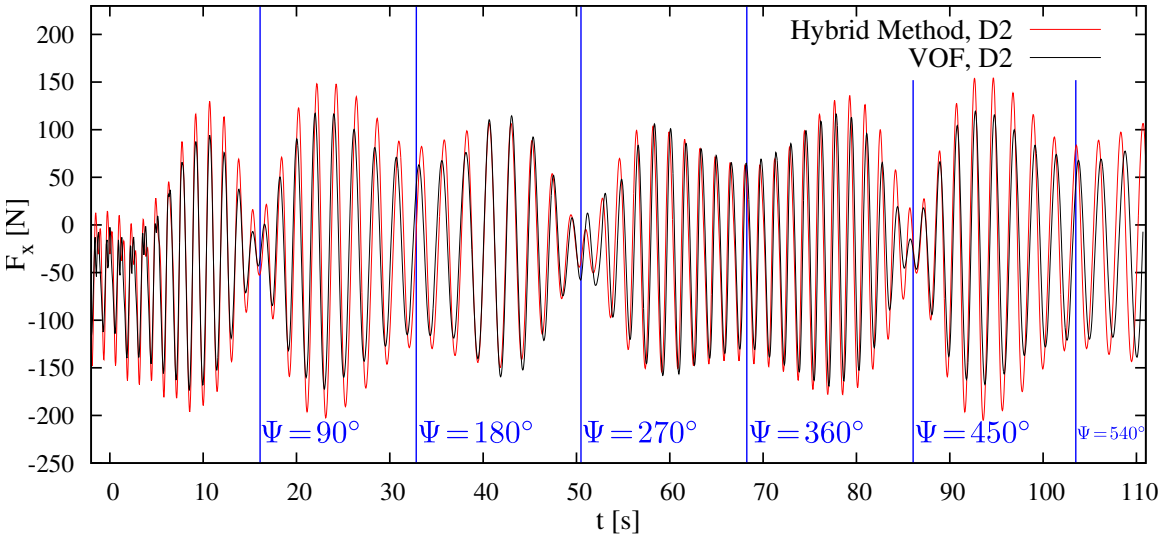

Figure 3.17: VOF and hybrid method surge forces (neglecting thrust) throughout DTC turn in waves

evenly centered on the VOF envelope for the duration of the simulation. The hybrid method force envelope is situated at a slightly larger mean value in head seas, as can be seen clearly in Figure 3.17 for $t < 5$ s and again when the model reaches a heading of $\Psi = 360°$. Overall, the small deviations in surge force cause a deviation in forward speed at a delayed time.

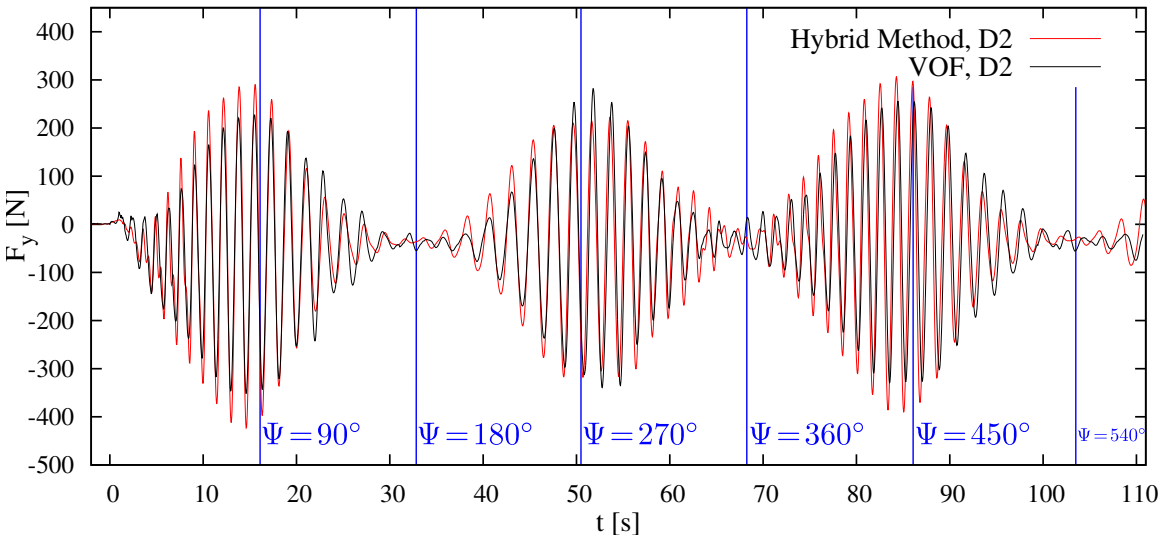

Figure 3.18: VOF and hybrid method sway force throughout DTC turn in waves

Figure 3.18 shows that the sway force envelopes overlap, both with a mean value close to zero. The largest difference in total hydrodynamic force is observed in the

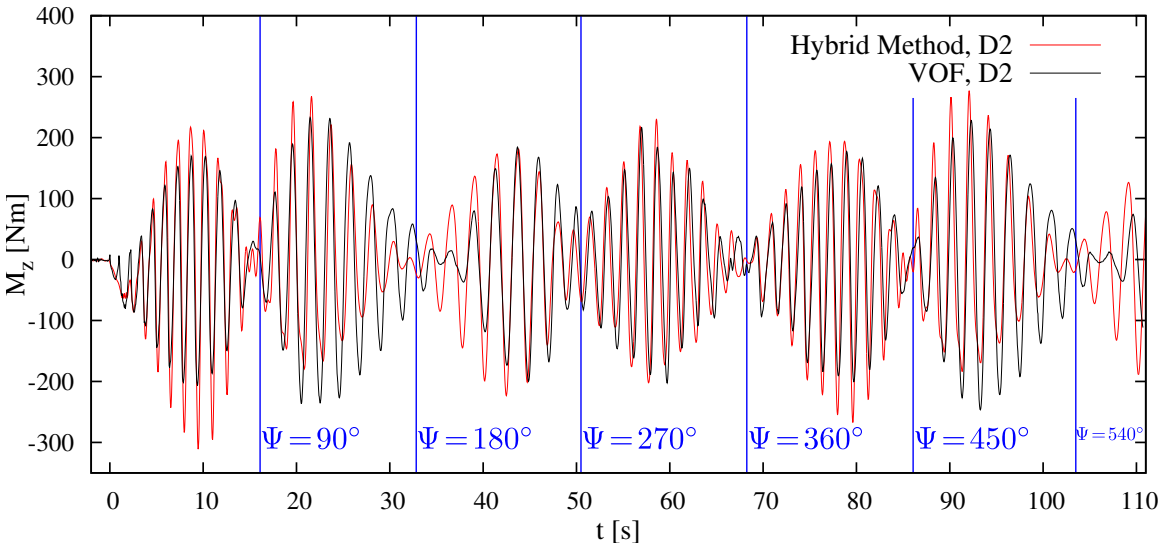

Figure 3.19: VOF and hybrid method yaw moment throughout DTC turn in waves

yaw moment time series plotted in Figure 3.19. The largest deviations between VOF and the hybrid method are found in oblique sea states, with the hybrid method predicting a larger (negative) moment (moment into starboard turn) compared to the VOF from $\Psi = 0° \rightarrow 90°$. The hybrid method again overpredicts moment (into turn) turning out of head seas from $\Psi = 360° \rightarrow 450°$. The over and underpredictions of yaw moment correspond to temporal variations seen in the yaw rate time series (Figure 3.15) in each of the methods. Despite differences in the total hydrodynamic yaw moment between the two methods, the comparison is not as straightforward. For example, the roll, pitch, and yaw degrees of freedom are dynamically coupled in the nonlinear VOF results. Moreover, the yaw rate and state vectors are a better indicator for comparison of the two methods.

One aspect of the hybrid method that benefits the analysis of maneuvering behavior of ships is the ability to separately analyze various components of the force. The modularity of the framework allows for separation and comparison of different force components. By investigating magnitudes of various force components throughout the turn, an assessment can be made of what components play a prominent role. Furthermore, an understanding is gained of how of error in a particular component

is realized in the context of the total hydrodynamic force.

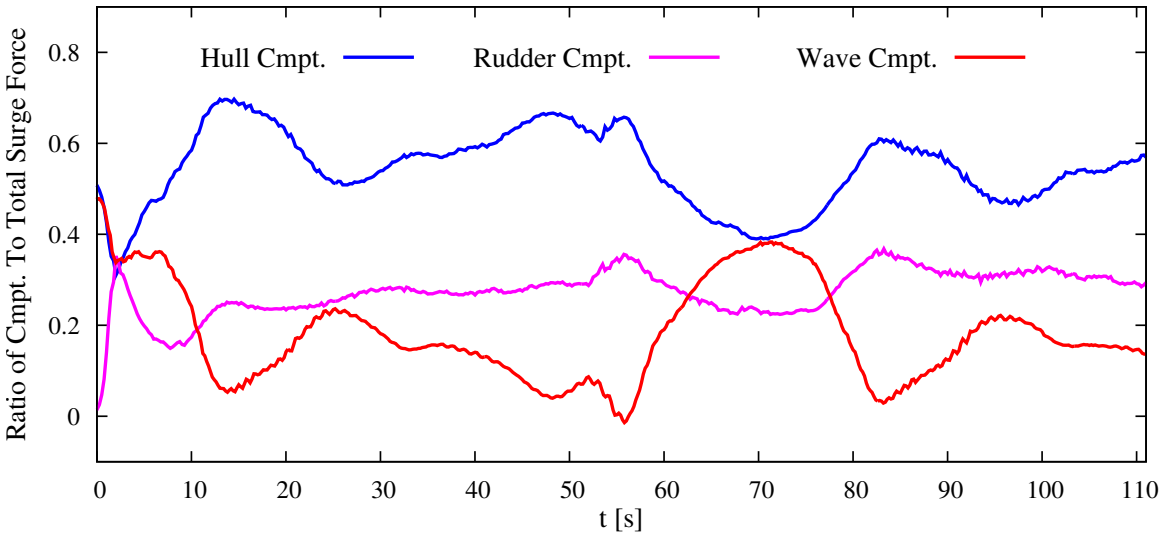

Figure 3.20: Relative contribution towards total surge force from hull component, rudder component, and wave component

Figure 3.20 displays the contribution of the surge force from single-phase RANS on the hull, on the rudder, and the first and second order wave force as a proportion of the total resistance (thrust disregarded). These forces are considered in the maneuvering frame of reference. The figure shows the well-known result that added resistance (added surge force in head seas) can be a significant portion of the overall resistance. In this maneuver, Figure 3.20 indicates that the first order wave resistance and added resistance comprise up to 40% of the total resistance. Another noteworthy trait from this maneuver is that all three components contribute equal portions to the total resistance (not counting inertial force due to deceleration) during the transient phase of the rudder motion. Practically, this indicates that the wave modeling, rudder force prediction, and forces on the hull must all be modeled accurately to capture the initial transient phase of the simulation.

To the compare the sway force, the component from the rudder and from the second-order wave force (first order wave force contributes zero sway force and moment) are computed as percentages of the viscous double-body hull force from the single-phase RANS. The net sway force is relatively small relative to the rudder com-

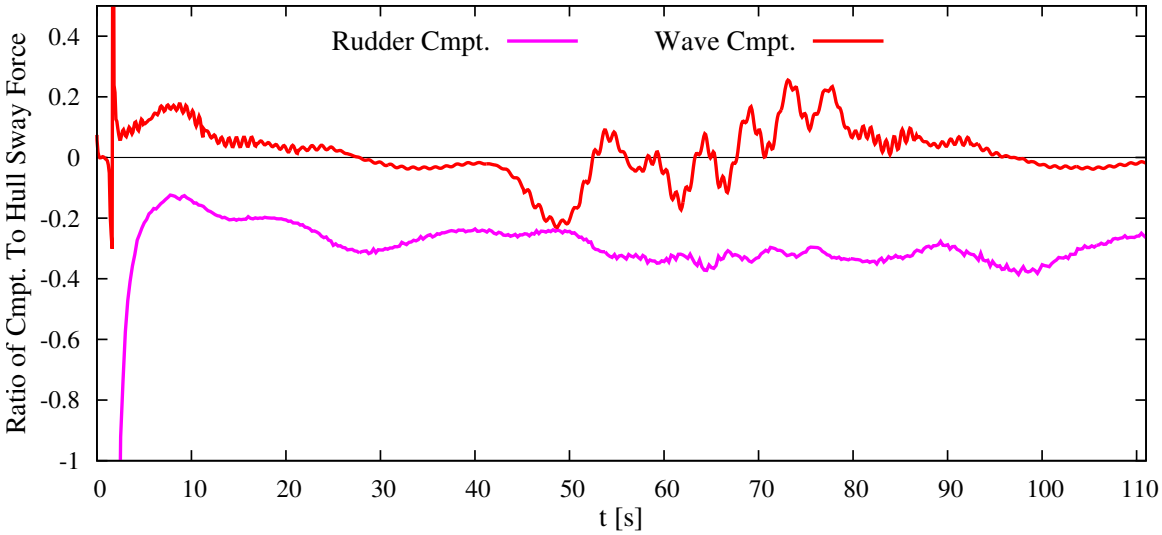

Figure 3.21: Ratio of rudder sway force and wave sway force to hull sway force

ponent and the opposite acting hull component. Therefore, Figure 3.21 presents the wave component and rudder component relative to the hull component. For $t < 10$ s the rudder sway force which develops as soon as the rudder is executed is large in proportion to the hull sway force which has not developed yet. In fact, the model travels $1L$ before deviating from its original course. The model travels roughly $0.5L$ without appreciable drift angle and so cross flow does not produce an appreciable sway force on the hull. The conclusion is again that accurate modeling of rudder force is particularly important in the initial transient phase of the turn. The BEM predicted that the second-order wave forces in the sway direction are of lesser magnitude than rudder force.

The rudder moment and moment on the hull are the two largest hydrodynamic components of the total hydrodynamic moment. Similar to the comparison of sway force, the net yaw moment is small compared to the rudder moment and yaw moment on the hull. Therefore, the hull moment and total moment from wave effects are measured relative to the rudder moment. During the transient phase of the turn ($t < 10$ s) the hull moment is twice the rudder moment when yaw angular acceleration is largest. The wave moment is always less than half of the rudder moment other than

the initial phase of the turn, when the wave moment is of the same magnitude as the rudder moment.

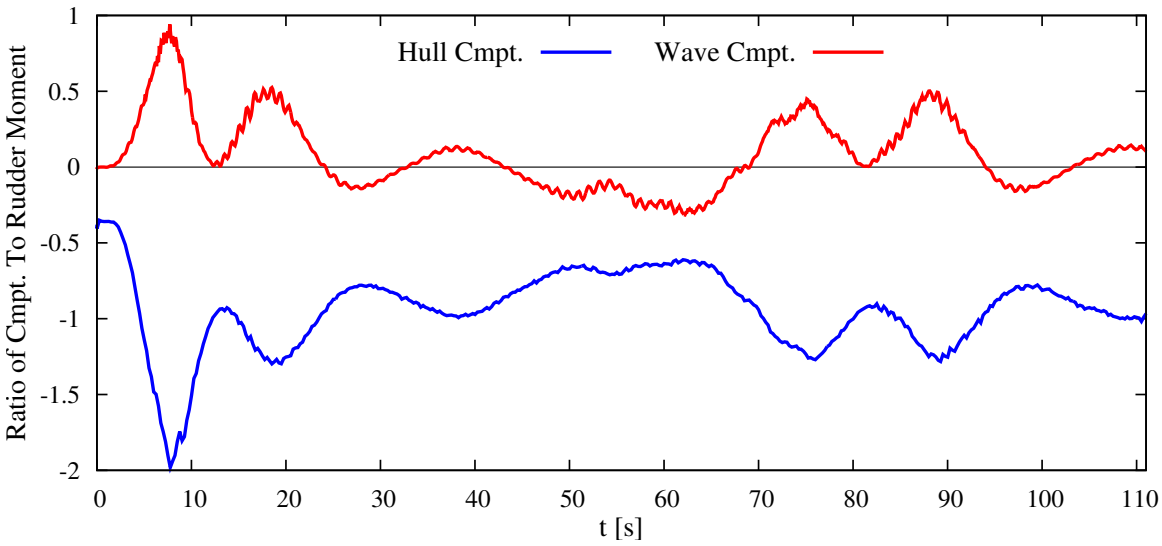

Figure 3.22: Ratio of hull yaw moment and wave yaw moment to rudder yaw moment

3.4 Hybrid Method Summary and Computational Cost Comparison

The performance of the hybrid method has been compared to high-fidelity simulations computed with the nonlinear (rigid body dynamics and hydrodynamics) VOF method in the preceding sections. This section provides a numerical comparison between the cost of computing the high-fidelity VOF results and the hybrid method results. Then, several computational details are outlined which relate to the extension of this method to maneuvering in irregular sea states.

The nonlinear VOF simulations are computed on the United States Navy High Performance Computer (HPC) Gaffney. The Gaffney HPC features just over 700 standard memory compute nodes with 48 cores per node. The processor architecture on the Gaffney HPC is Intel® Xeon® Platinum 8168. Each core possesses a base processor frequency of 2.70 GHz.

The hybrid method simulations for the DTC hull are computed on a Puget Systems custom-built desktop running the Ubuntu 14.04 distribution of Linux. The desktop contains an Intel® Xeon® E5-1660 v3 (Haswell architecture) processor with eight cores, each with base processor frequency of 3.00 GHz. The BEM is run in serial and, as it is only called every eight CFD time steps, it was not allocated a processor of its own; the task of balancing the eight cores devoted to solving the CFD and the occasional extra task of solving the BEM is left to the operating system. Testing revealed that the hybrid method run times are slightly reduced when using the dual-threading technology built into the processors and allowing the operating system to handle the extra load of the BEM solution, as opposed to reserving an entire core for the solution of the BEM. This is certainly not the optimal approach but with the resources on hand, it is shown to to be the most efficient.

The following aspects and simplifications are considered in the computational cost comparison. The numerical comparison here does not attempt to adjust for scalability of the OpenFOAM software as compiled on the Gaffney HPC. Furthermore, although an optimum distribution exists for number of finite volume cells (unknowns) assigned to each processor, this comparison does not consider the efficiency of decomposition of the total number of unknown degrees of freedom. Lastly, when comparing the cost savings of the hybrid method to the VOF method, the 0.30 GHz differential between processor frequencies on each of the systems is disregarded.

The hybrid method running on the desktop machine required 403 core-hours to simulate 100 s of the maneuver on mesh D1. The VOF method required 4,145 core-hours to simulate 100 s of the maneuver on mesh D1. Using the simplifying assumptions above, use of the hybrid method offers a reduction in computing cost by a factor of 10.2.

The hybrid method running on the desktop machine required 1,354 core-hours to simulate 100 s of the maneuver on mesh D2. The VOF method required 26,625 core-

hours to simulate 100 s of the maneuver on mesh D2. On mesh D2, the computational reduction is even greater using the hybrid method, with a reduction in cost by a factor of 19.5. The differences are more pronounced on the mesh D2 which has finer resolution that mesh D1, as the adaptive time step used in the VOF method is largely driven by Courant number restrictions near the fluid interface. In mesh D1, short wavelengths near the ship were likely under-resolved and the VOF method is able to take time steps similar to the constant time step prescribed in the double-body RANS part of the hybrid method. The results are summarized in Table 3.8.

Table 3.8: Cost comparison between hybrid method and VOF in DTC simulations

	Mesh D1	Mesh D2
Cost VOF [cpu-hrs]	4,145	26,625
Cost Hybrid [cpu-hrs]	403	1,354
Cost VOF/Cost Hybrid	10.2	19.5

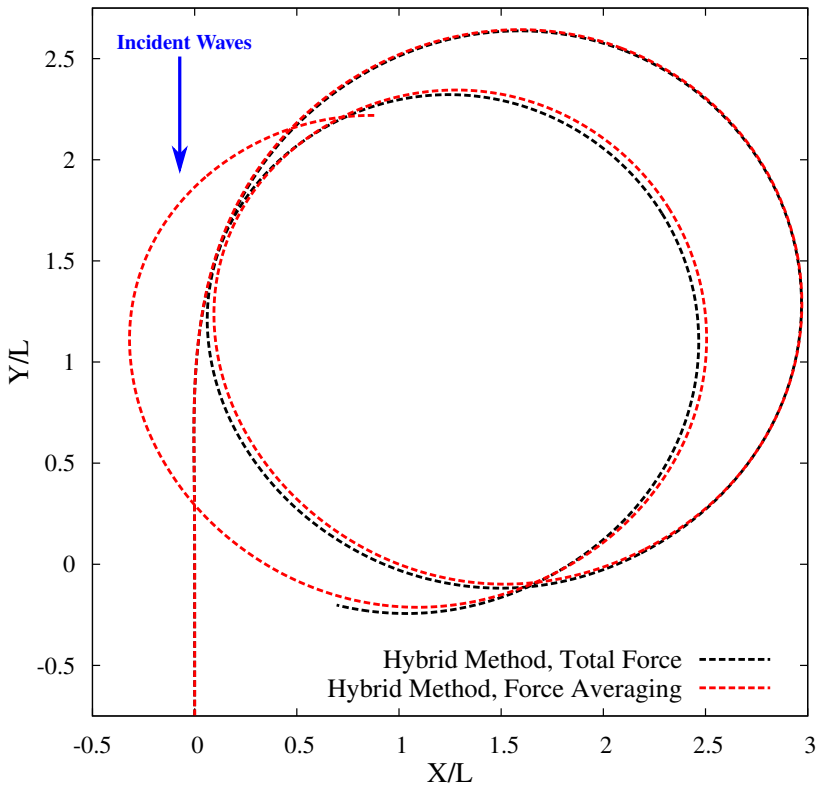

Figure 3.23: Turning circle trajectories in waves as predicted by hybrid method with and without second-order force averaging

In the final discussion in this chapter, the focus shifts back to the topic of time-averaging the second-order wave forces as described in Section 2.4.2. All results computed using the hybrid method in this chapter have utilized the time-averaged second-order wave forces. Now, the the turning circle in waves is computed and compared to the results with force-averaging. The trajectories are nearly indistinguishable as shown in Figure 3.23.

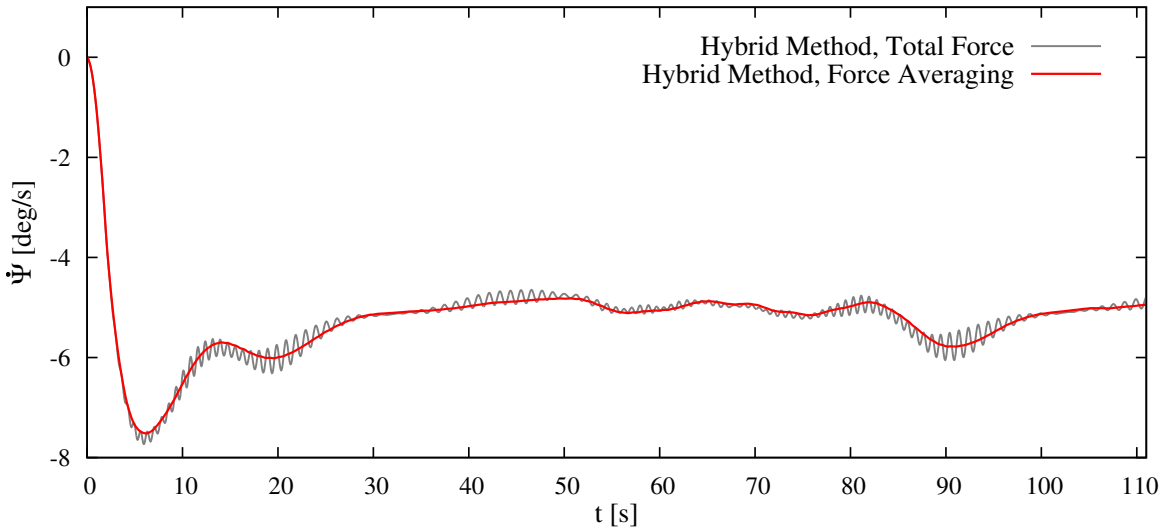

Figure 3.24: Yaw rate predicted by hybrid method with and without second-order force averaging

The yaw rate is investigated to serve as an example of the effects of including forcing at the wave encounter frequency into the low-frequency maneuvering equations. Although the inertia of the body is effective at preventing a large response at the wave frequency, a small oscillation persists in the low-frequency yaw rate. The yaw rate predicted after providing a time-averaged force vector to the maneuvering equations follows the mean value of the case using the total second-order force.

Although the oscillation at the wave frequency is small, the forces clearly show presence of added mass forces occurring at the wave frequency when using the total second-order force. Again, the yaw moment computed in the simulation with force-averaging follows the mean value of the envelope with oscillations at the wave-frequency.

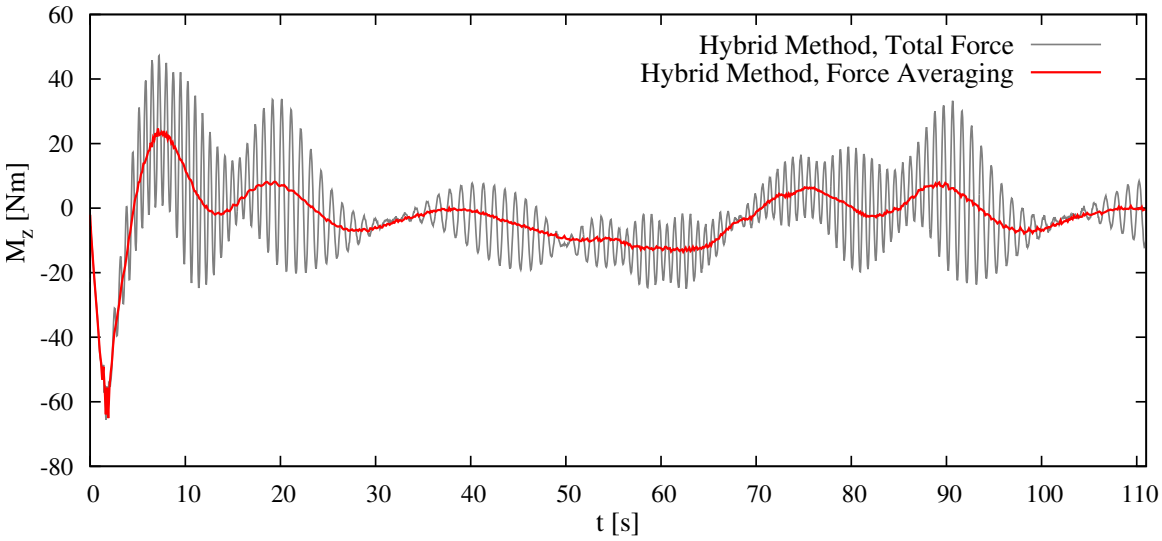

Figure 3.25: Yaw moment predicted by hybrid method with and without second-order force averaging

CHAPTER IV

Numerical Test Case 2: KRISO Container Ship

This chapter presents the second of two numerical test cases selected to assess the performance of the proposed hybrid method for prediction of combined manuevering and seakeeping motion. This numerical experiment largely follows the same scope as with the DTC hull in Chapter III. The study begins by isolating the seakeeping problem and investigating the seakeeping response of the Korea Research Institute of Ships and Ocean Engineering Container Ship (KCS) hull into regular head seas at $Fn = 0.26$. Next, the diffraction problem is isolated; the ship is held captive at constant speed and heading and the wave diffraction forces are computed by the BEM and separately by the VOF method. Next, the maneuvering problem is isolated and the hybrid method is compared to a nonlinear six degree-of-freedom VOF simulation of the KCS hull turning in calm-water with initial Froude number of $Fn = 0.157$. Finally, the hybrid method is compared against the results generated with VOF in the simulation of the KCS hull turning in regular waves.

4.1 Seakeeping Validation

Seakeeping computations are made to demonstrate the capability of both the VOF method and the BEM to accurately predict ship motions on a fixed course. Furthermore, the seakeeping validation of the VOF method serves as a check on mesh

resolution with respect to resolving incident, radiated, and diffracted waves within the VOF method. The accuracy (and resolution) of wave excitation forces is checked by constructing motion RAO's rather than by investigating the forces directly.

Before the test matrix of seakeeping and added resistance computations is outlined, an overview is provided of the computational model and setup. The test case that is selected for the following seakeeping computations (and ensuing maneuvering computations) utilizes the Korea Research Institute of Ships and Ocean Engineering Container Ship (KCS) hull form, pictured in Figure 4.1, and whose main particulars are provided in Table 4.1. The KCS hull form has enjoyed a wide interest as a test bench for numerical validation (Larsson et al., 2013, 2015).

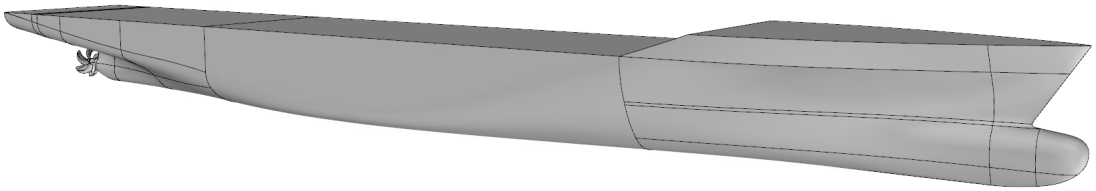

Figure 4.1: Rendered NURBS representation of KCS hulll form

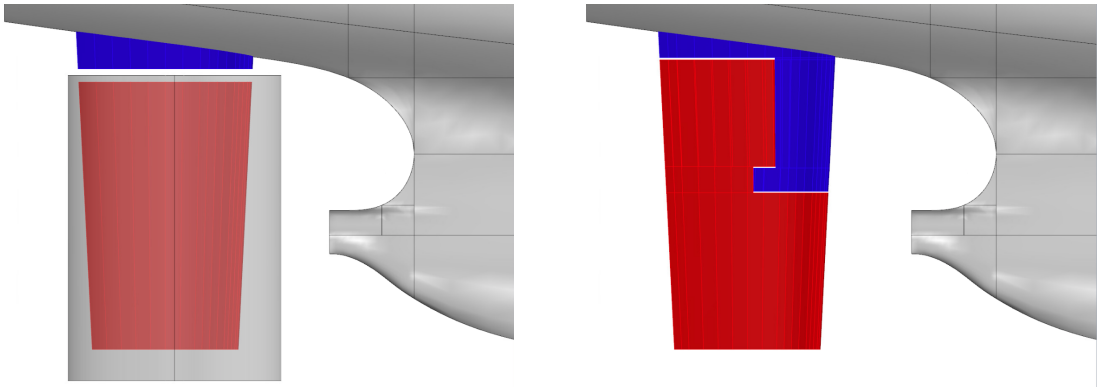

(a) (b)

Figure 4.2: (a) Modified rudder within Arbitrary Mesh Interface zone (b) Original KCS rudder

The rudder geometry for the KCS is simplified in this work as shown in Figure 4.2, primarily to enable the use of a sliding mesh technique to accommodate rudder motion. The rudder rotates about the aft perpendicular of the KCS model within an Arbitrary Mesh Interface (AMI) region shown in Figure 4.2 (a). The original KCS

rudder geometry is classified as a horned rudder; the rudder horn is the blue portion of the rudder in Figure 4.2(b) that remains fixed with respect to the ship. Horned rudders provide several structural and hydrodynamic advantages over traditional spade rudders but also create modeling challenges in CFD. The moveable geometry and interlocking parts of the rudder can be handled by the overset method or the immersed boundary method. For the purposes of testing the hybrid formulation, this work takes the convenient simplification of grouping as much of the rudder horn into the rudder moveable (red) area as possible. Changes to the lateral area through the above rudder modifications are listed in Table 4.1.

Table 4.1: Main particulars of the KCS hull

Main Particulars ($\lambda = 1/75.24$ Scale)	Value
L	3.057 m
B	0.428 m
T	0.144 m
Displacement	0.122 m^3
C_B	0.651
LCG (+ forward from AP)	-0.045 m
KG	0.19 m
r_{xx}	0.171 m
r_{yy}	0.764 m
r_{zz}	0.764 m
Rudder Lateral Area, A_{Lat}	0.0096 m^2
Rudder Moveable Area, A_{R}	0.008 m^2
Simple Rudder Moveable Area, $\tilde{A}_{\text{R}}$	0.0088 m^2
Initial Speed	0.860 m/s
Propeller Diameter	0.105 m
Number of Blades	5

The seakeeping computations are compared to experimental results from Sadat-Hosseini et al. (2015). The experimental data set from Sadat-Hosseini et al. (2015) was also utilized in the Tokyo 2015 CFD Workshop. Here, a subset of wave conditions are tested. The published dataset featured experiments at two model scales ($L = 2.7$ m and $L = 6.1$ m) completed at FORCE Technology and some wave conditions tested at IIHR for the smaller model. The dataset also includes four attempts to compute the

RAO's using two different CFD codes as well as results from a potential-flow code. Here the focus is on validation of the VOF method (and meshes) for seakeeping and computed results for a $L = 3.057$ m model and are compared against experiments from FORCE Technology only. All waves simulated have steepness of $H/\lambda = 1/60$.

Table 4.2: Wave conditions for KCS seakeeping simulations, ($Fn = 0.26$)

λ/L	λ [m]	H [m]	T [s]	$k\zeta_I$
0.71	2.170	0.036	1.179	0.052
0.75	2.293	0.038	1.212	0.052
1.00	3.057	0.051	1.399	0.052
1.15	3.516	0.059	1.501	0.052
1.25	3.821	0.064	1.564	0.052
1.37	4.188	0.070	1.638	0.052
1.50	4.546	0.076	1.714	0.052

The mesh parameters for meshes used in the seakeeping and maneuvering computations are listed in Table 4.3. The finest mesh, K3, is only used for VOF simulations at the peak of the heave RAO to check mesh convergence.

Table 4.3: Mesh parameters for KCS seakeeping computations

	K1	K2	K3
# of cells, VOF Domain	2,198,636	6,169,825	17,032,280
# of cells, Hybrid Domain	1,292,274	2,803,834	N/A
Avg. y^+	57	48	33

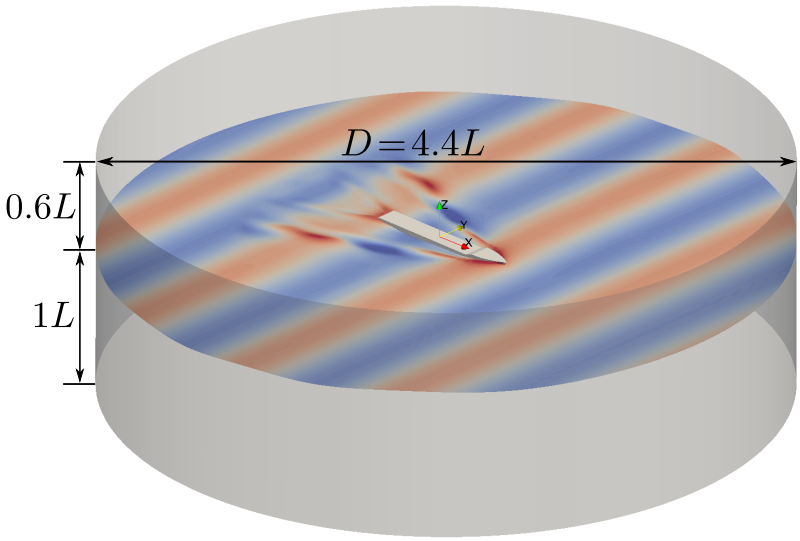

Figure 4.3: Dimensions of CFD domain for KCS simulations

The heave and pitch RAO's in Figures 4.4(a)-(b) show excellent agreement with the experimental motion RAO's, though the finest mesh was required to capture the peak of the heave RAO. Although these tests are completed at $Fn = 0.26$ and the turning circles in waves will be computed at $Fn = 0.157$, the wavelength of $\lambda/L = 1$ appears to be accurately captured at the higher speed; $\lambda/L = 1$ will be simulated in the turning circles in waves.

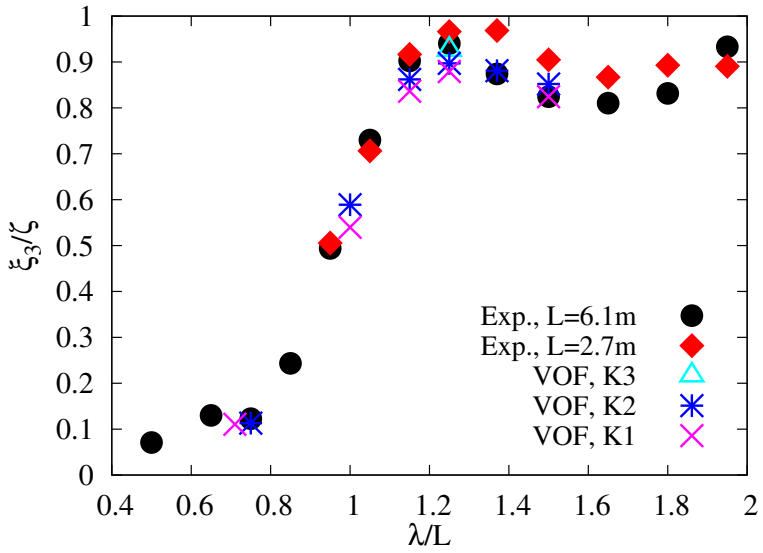

(a)

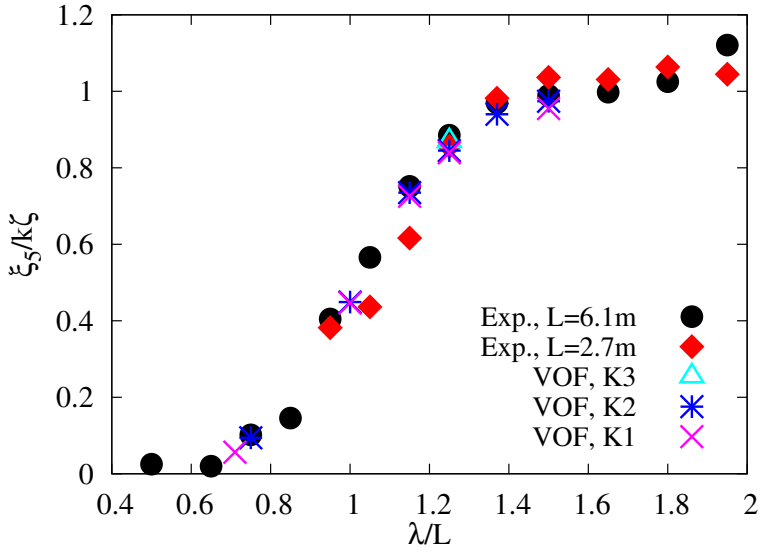

(b)

Figure 4.4: (a) Heave RAO for KCS, $Fn = 0.26$ (b) Pitch RAO for KCS, $Fn = 0.26$

The added resistance in waves is also computed. The added resistance from VOF results required computation of the calm-water resistance. The steady resistance in calm water, R_{cw}, was computed only on the K2 mesh. The model is permitted to sink and trim but prescribed at a constant forward speed. Then, the added resistance, R_{A}, was computed from the cases in head waves by subtracting the calm water resistance from a time-average of surge force over p encounter periods, T_e, as given in Equation 4.1. The number of encounter periods used in computing the time-averaged surge force in waves varies between runs. In general, the postprocessing of added resistance utilized as many encounter periods as possible while a periodic force could be obtained from the force signal. The added resistance coefficient, C_{x}, is derived by nondimensionalizing the added resistance by $\rho g B^2 {\zeta_I}^2 / L$.

$$
\begin{aligned}
R_{\mathrm{A}} &\equiv \frac{1}{pT_e} \int_{t}^{t+pT_e} F_x dt - R_{\mathrm{cw}} \\
C_x &\equiv \frac{R_{\mathrm{A}}}{\rho g {\zeta_I}^2 B^2 / L}
\end{aligned}
\tag{4.1}
$$

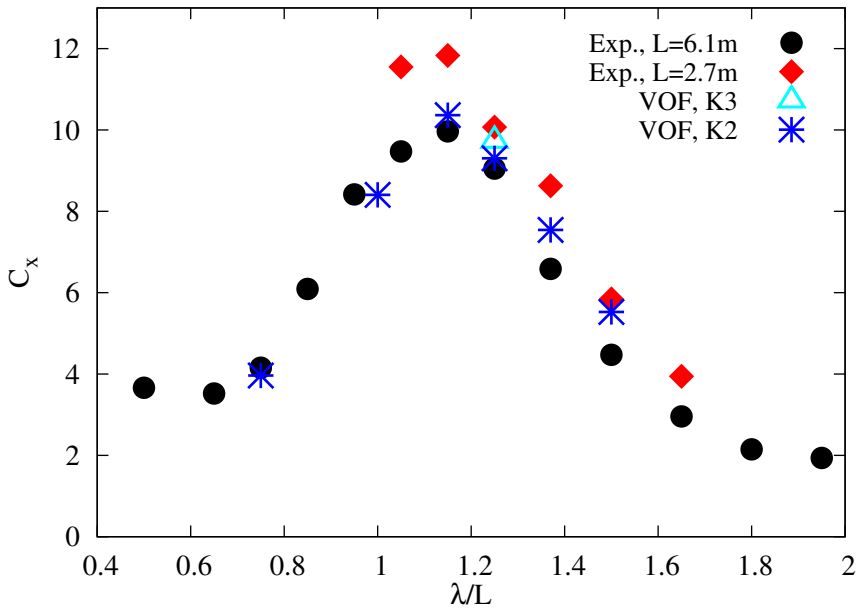

Figure 4.5: Added resistance RAO for KCS, $Fn = 0.26$

The computed added resistance coefficients, shown in Figure 4.5, agree well with measurements. All computed values fall between the two sets of measurements at different model scales. The computation at $\lambda/L = 1$ is marginally below the experimental data for $L = 6.1$ m. No data for the smaller model exists for comparison at $\lambda/L = 1$. Nonetheless, the trend is agreeable with both sets of experimental data.

4.2 Wave Diffraction Problem in Oblique Seas

This section investigates the performance of the linearized BEM in computing unsteady wave diffraction loads in oblique seas. Moreover, this study identifies wave headings where wave loads, as predicted by the BEM, could differ from the nonlinear VOF. The BEM mesh used in the Aegir computations is shown in Figure 4.6.

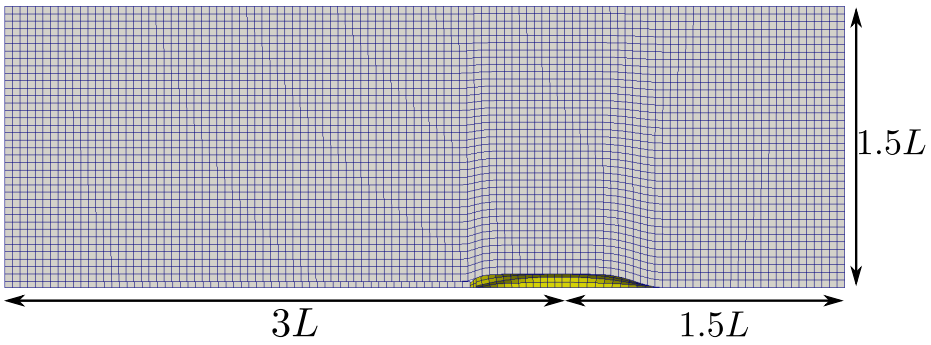

Figure 4.6: Free surface and KCS hull hydrodynamic panelization of Aegir mesh

Table 4.4: BEM mesh parameters for KCS simulations

Patch Group:	# of panels
Free Surface	8042
Hull Surface	236

Five wave headings are selected including bow and stern quartering waves. The forward speed is prescribed as a constant ($Fn = 0.157$) and the ship heading remains aligned with the Earth-fixed X_E-axis. The waves, all of steepness $H/\lambda = 1/60$, are propagated from the model starboard side according to the wave heading convention in Equation 2.10 ($\chi = 180°$ head seas). The time-averaged surge diffraction forces are computed as in Equation 4.1 for all wave headings.

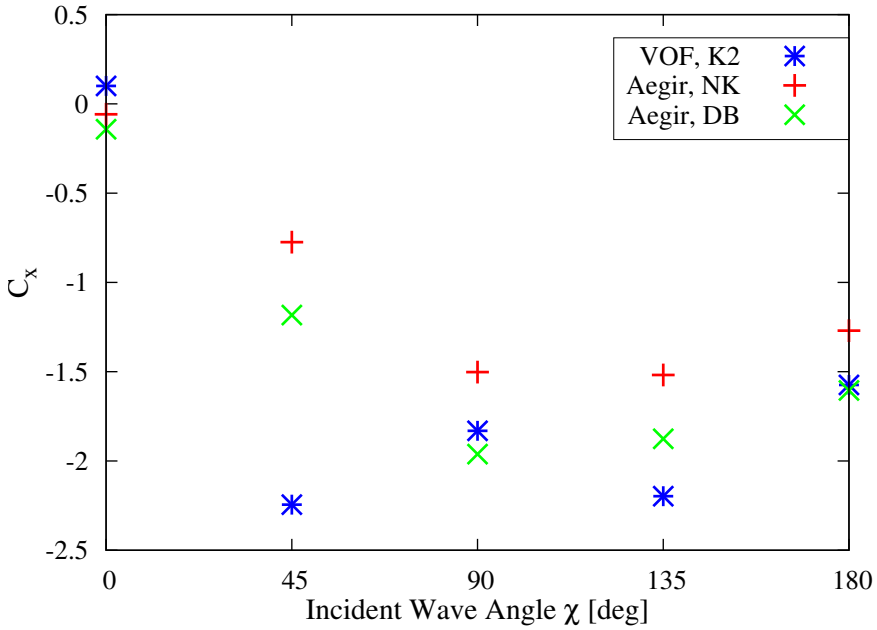

Figure 4.7: Mean surge diffraction force RAO for KCS, $Fn = 0.157$

Figure 4.7 displays the second-order component of surge force for the diffraction problem. Although the double-body (DB) linearization is not utilized in the turning circle computations, it is included here as it presents a future path to improving the prediction of wave loads within the hybrid formulation. The Neumann-Kelvin (NK) linearization consistently underpredicts added resistance for all headings. The DB linearization shows some improvement in head seas and bow quartering seas however struggles in stern quartering seas along with the NK linearization.

Figure 4.8 shows the time-averaged sway force for the wave diffraction problem. The mean sway force is computed and nondimensionalized similarly to the surge force, with the exception that the calm water component of sway force is zero. The predictions using the NK linearization and DB linearization show very little difference in the case of sway diffraction force. Both BEM linearizations agree well with VOF predictions for all wave headings except stern quartering seas.

Figure 4.9 displays the yaw diffraction moment for the five wave headings; the yaw moment was time-averaged and nondimensionalized by $\rho g {\zeta_I}^2 BL$. The NK linearization again underpredicts in oblique and beam seas. The DB linearization shows

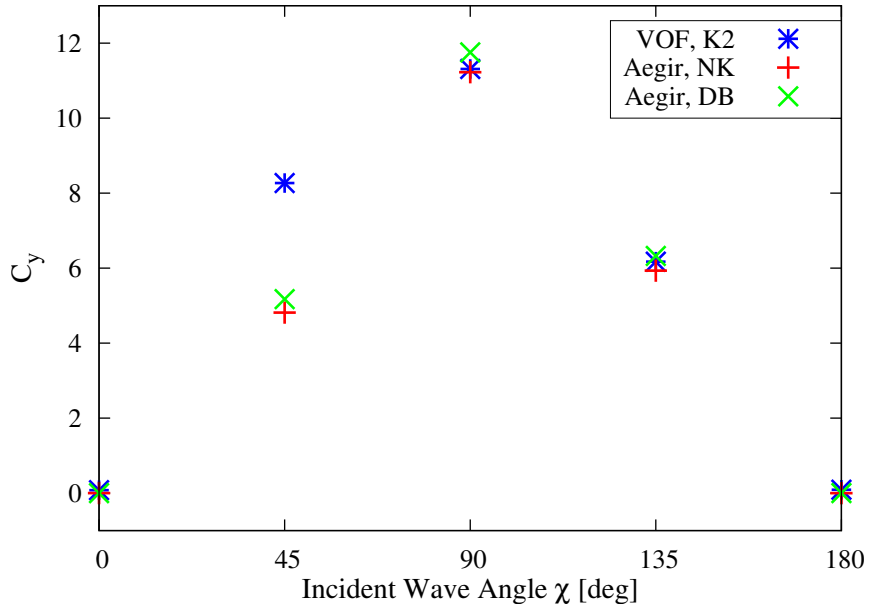

Figure 4.8: Mean sway diffraction force RAO for KCS, $Fn = 0.157$

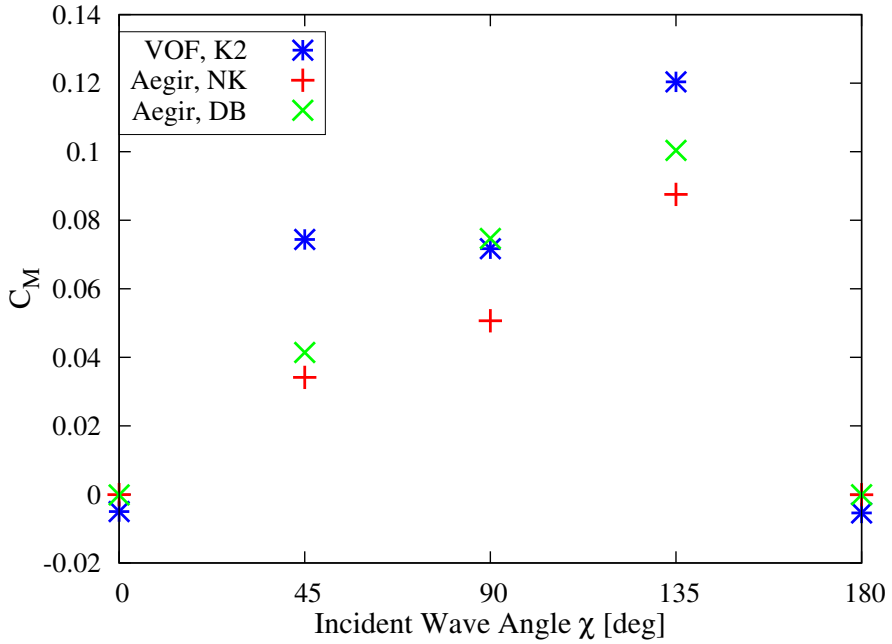

Figure 4.9: Mean yaw diffraction moment RAO for KCS, $Fn = 0.157$

improvement in beam quartering and beam seas but both linearizations show error in stern quartering seas. The BEM shows deviations from the VOF in all three higher-order forces. A computation on a finer mesh, such as mesh K3, should be completed for the stern quartering seas to assess numerical error in the VOF predictions. With these findings, deviations are anticipated in turning circles in waves, particularly dur-

ing time windows where the ship is in stern quartering waves.

4.3 Calm Water Turning Circle Prediction

A turning circle is predicted in calm water before regular waves are introduced. The details of the maneuver are provided in Table 4.5. The computational model is ramped to target speed in rectilinear motion. The velocity is prescribed as a half-cosine curve over a ramp period of $t_r = 8$ s. The initial ramp period is followed by an additional 4 s over which the forward speed is held at the constant target speed. In total, the surge degree of freedom is held constant for 12 s during which time the ship is permitted to travel over two ship lengths so that the flow field may develop.

Following the prescribed ramp in surge velocity with sway and yaw restricted, the model begins the maneuver nearly in a self-propulsive state. A self-propulsion test is performed, with the vessel free to sink and trim, with the propeller model to determine the required revolution rate of $n = 10.4$ rps. The propeller model used to simulate the free-running turning circle maneuvers (in both calm-water and in waves) is built using nonlinear regression (Knight and Maki, 2020) on propeller forces derived from pre-computed CFD simulations including a discretized, rotating propeller.

Table 4.5: Maneuver details for KCS calm-water turning circle prediction

Maneuver Details (Model Scale)	Value
Initial Speed	0.860 m/s
Initial Froude Number	0.157
Rudder Angle, δ	$+35°$
Propeller Model Rev. Rate, n	10.4 rps
Rudder Rate	$20.1°/s$

The turning circles predicted by the VOF method on meshes K1 and K2 and the circle predicted on mesh K2 with the hybrid method are plotted in Figure 4.10. The VOF circle on mesh K2 is roughly 5% smaller than predicted on the coarse K1 mesh. The circle computed using the hybrid method on mesh K2 overpredicts the transfer

by $0.15L$; the transfer is defined as the maximum extent of the ship trajectory in the X/L coordinate. The diameter, measured in distance in the X/L coordinate, predicted by the hybrid method is within 1% despite having a larger transfer.

Time stamps are overlaid on Figure 4.10 for the VOF and hybrid predictions both on the K2 mesh. By nature of taking a larger transfer, the hybrid method position eventually lags the position of the ship center of gravity predicted in the VOF computations. While the circles compare well in overall characteristics, it will be demonstrated that for turns in waves the lag in position increases exposure time to certain wave headings relative to the ship. As the higher order wave loads are not only functions of maneuvering velocity but also of ship position, and more generally time, errors in exposure window to given sea-states are more detrimental to predictions of trajectories in waves.

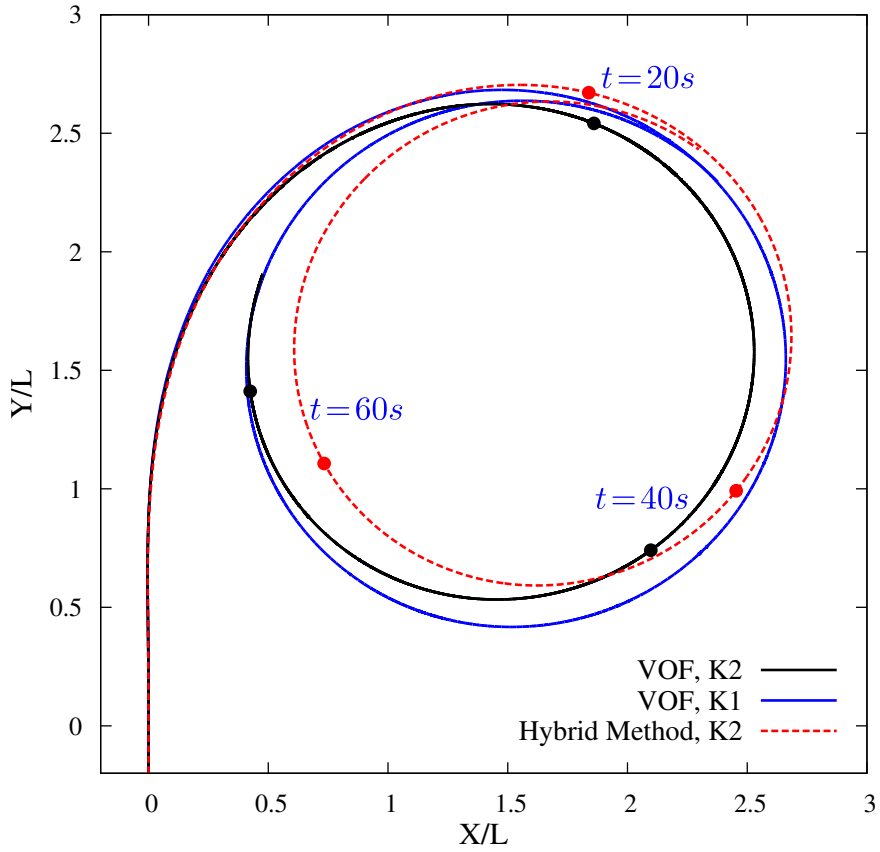

Figure 4.10: KCS calm-water turning circle trajectories ($Fn = 0.157$) computed using nonlinear VOF method and hybrid method

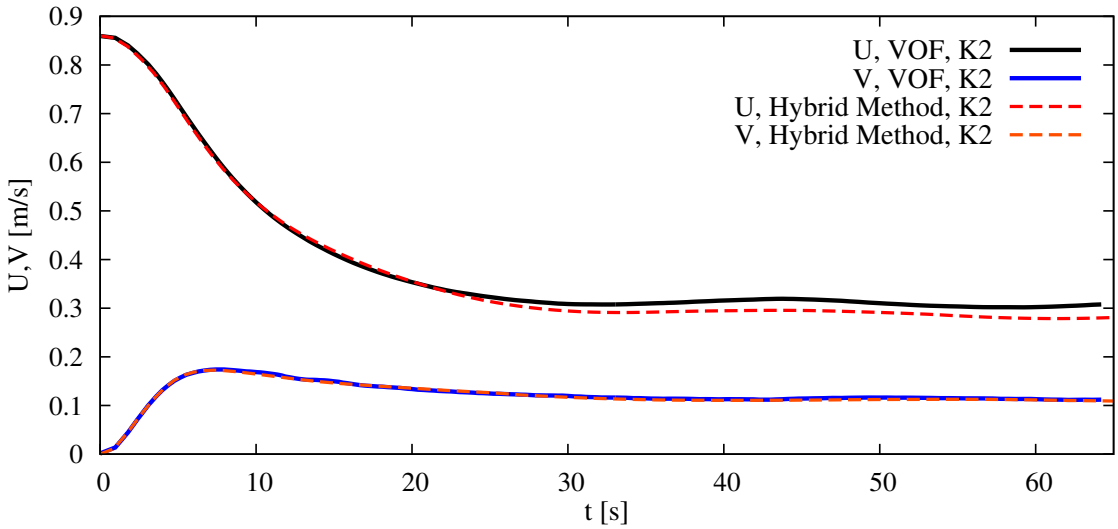

Figure 4.11: VOF and hybrid method forward and slip speed during KCS calm-water turning circle

The components of the predicted state vectors for the vessel are compared between each of the two methods. The forward speed and slip speed are plotted in Figure 4.11. Both methods predict a speed loss of approximately 65% the initial speed. The sway velocity is in excellent agreement but the hybrid method shows a slightly larger loss in forward speed. Figure 4.12 shows that additional forward speed loss is not due to the thrust offered in the propeller model. Rather, the propeller model responds by slightly increasing thrust. The additional forward speed loss then must be attributed either to exclusion of the roll angle in the hybrid simulations or sensitivity in surge force as a function of yaw rate.

The total velocity in the horizontal plane can also be compared together by investigating vessel drift angle as plotted in Figure 4.13. The drift angle predicted by the hybrid method is predicted within 1° of the VOF computation. The hybrid method prediction is initially less than the VOF during the time window when mean roll angle exists in state vector predicted using the VOF method. During the quasi-steady portion of the turn ($t > 30$ s) the hybrid method predicts roughly 1° larger drift angle than the VOF method.

The roll angle computed on the K1 mesh and K2 mesh using the VOF method is

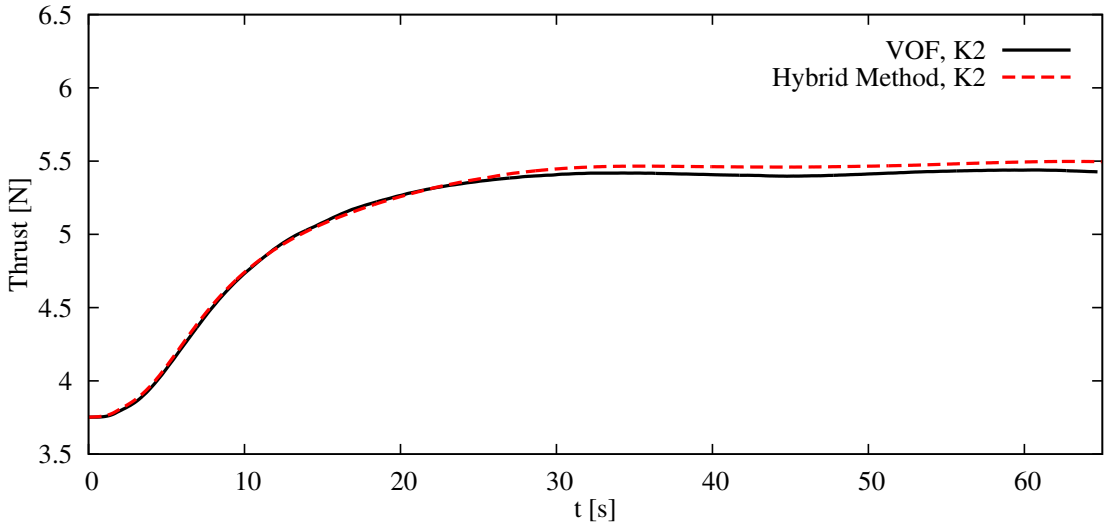

Figure 4.12: Thrust provided by propeller model in VOF and hybrid method calm-water KCS turning circle maneuvers

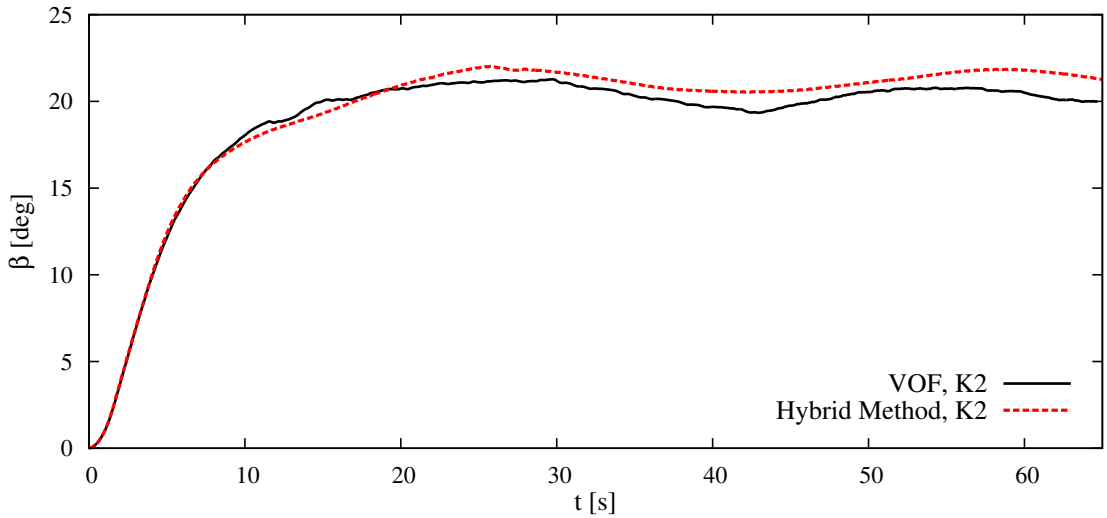

Figure 4.13: Drift angle predicted by VOF and hybrid method simulations during KCS calm-water turning circle

plotted in Figure 4.14. In the initial transient portion of the turn both meshes yield similar results, each with a 3° roll to starboard followed by a 6° roll to port. The mesh with finer resolution (K2) shows a roll response that has more viscous damping. Both meshes show an oscillation about a zero mean roll in the quasi-steady portion of the turn, with the roll oscillation decaying more rapidly on mesh K2. Given the decay of roll angle and zero mean value, this does not suggest exclusion of the roll degree of freedom to be the contributing factor to excess loss of forward speed in the

hybrid method.

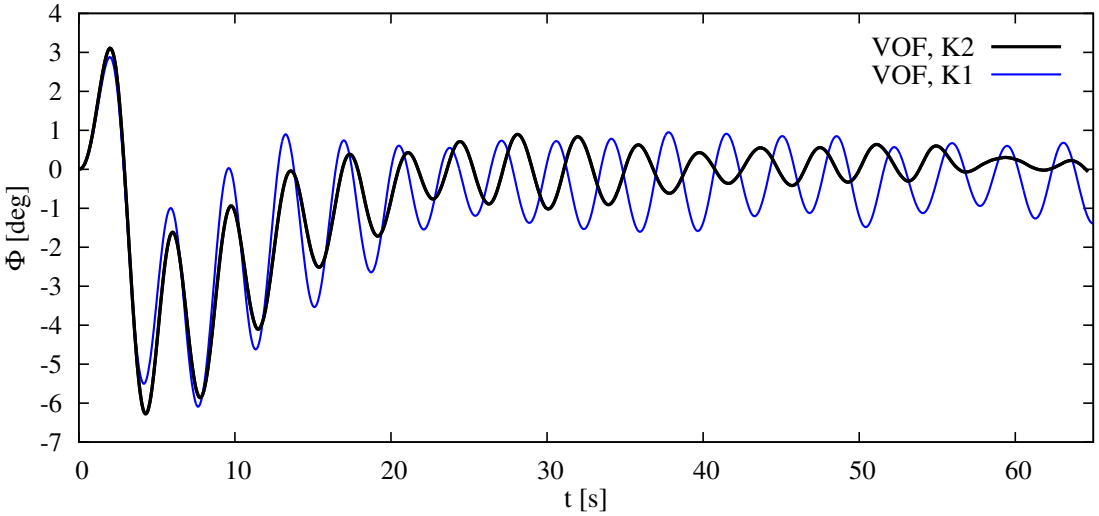

Figure 4.14: Roll predicted by VOF simulations during KCS calm-water turning circle

The hybrid method also underpredicts yaw rate, as shown in Figure 4.15, which is closely related both to excess loss in forward speed and the larger transfer distance. The influence of forward speed loss impacts the yaw rate and diameter of the turn in two counteracting ways. First, a loss of forward speed decreases rudder lift, though the constant rpm propeller model tends to increase thrust and induce larger velocities through the propeller plane and over the rudder. Loss of lift on the rudder results in diminished turning ability and yaw rate, and trajectories would be expected to increase. The second impact of forward speed loss is that the less hydrodynamic steering force is necessary to maintain a circular trajectory of a given radius due to reduction in the centripetal inertial force. These two counteracting affects are delicately balanced and are ultimately resolved through the solution to the nonlinear dynamics of the vessel.

4.4 Turning Circle Prediction In Regular Waves

The computations in this section model the KCS making a starboard turn in waves, with the ship initially advancing into head seas. The computational setup

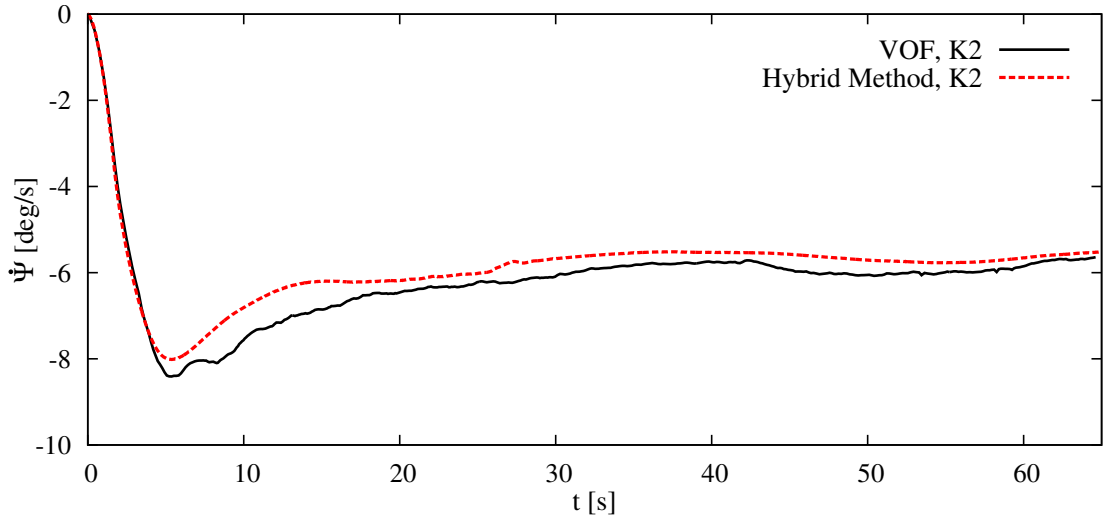

Figure 4.15: Yaw rate predicted by VOF simulations during KCS calm-water turning circle ($Fn = 0.157$)

and initial conditions are similar to the setup for the calm-water simulations with some details of the maneuver listed in Table 4.6. Using the hybrid method, a cursory estimate of propeller revolution rate is determined for the model self-propulsive point in head seas. The propeller model in the following hybrid method computations produces 4% more thrust than the total resistance as measured by the hybrid method. The same model is utilized in both the hybrid method and the VOF method. However, as the hydrodynamic forces and state vectors vary from one method to the other, and the propeller force model depends functionally on the state vector components, the model may behave slightly differently in the free maneuver.

Table 4.6: Maneuver details for KCS turning circle prediction in waves

Maneuver Details (Model Scale)	Value
Initial Speed	0.86 m/s
Initial Froude Number	0.157
Rudder Angle, δ	$+35°$
Propeller Rev. Rate, n	13.2 rps
Rudder Rate	$20.1°/s$
Incident Wave Amplitude, ζ_I	0.024 m
λ/L	1.0
ω_0	4.49 rad/s
T_0	1.4 s

The trajectories in the following analysis are plotted in the first quadrant for convenience. The trajectories are shifted such that the rudder execution occurs at the origin. Furthermore, all time series are shifted such that rudder execution occurs $t = 0$ s. Figures 4.16(a)-(b) display turning circle trajectories computed with both the hybrid method and the VOF method, each on two meshes to check the sensitivity of the predicted trajectory to discretization error. Both the hybrid method and VOF method produce tighter turning circles on mesh K2.

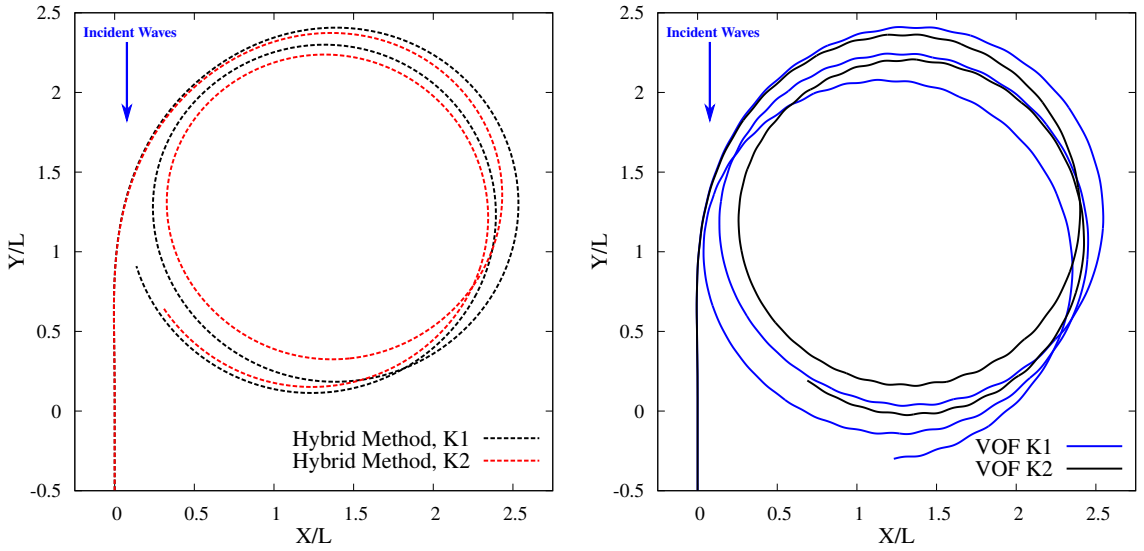

Figure 4.16: (a) Hybrid method trajectories on K1 and K2 meshes plotted for $t <$ 100 s (b) VOF method trajectories on K1 ($t <$ 138 s) and K2 ($t <$ 94 s) meshes

The computed trajectories on mesh K2 using the hybrid method and the VOF method are plotted together in Figure 4.17. The time stamp is overlaid on the trajectories and the comparison shows that the distance between common moments in time between the two methods does not grow uniformly as in the calm-water simulation. The reason behind this phenomenon is because the nominal turning radius of the VOF trajectory is larger than the hybrid trajectory but the drift direction also varies between the two methods. The VOF method appears to be drifting in the direction of wave propagation, though two circles may not be long enough duration to say. The

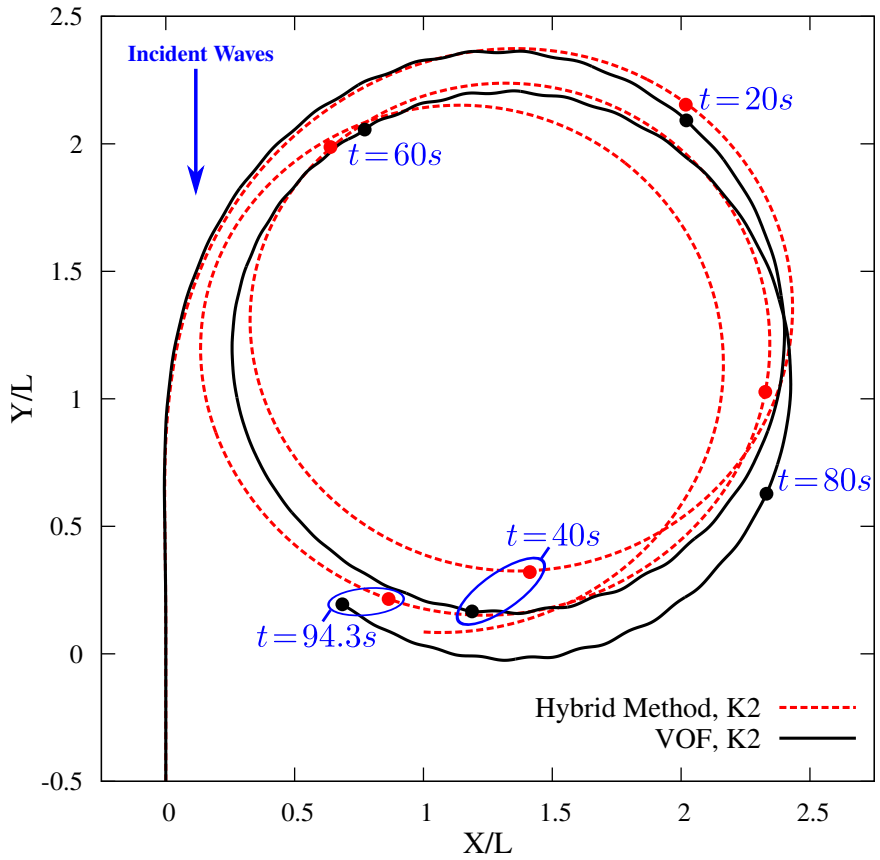

Figure 4.17: KCS turning circle trajectories (Fn = 0.157) in waves computed using nonlinear VOF method and hybrid method

hybrid method clearly has a drift direction at an angle relative to the incident wave field.

The cause behind the change in drift direction can be partly explained by variations in the forward speed predicted in the hybrid method as compared to the VOF method results. The hybrid method underpredicts forward speed for all time, but most severely in following seas. The best agreement between forward speed predicted by VOF and the hybrid method is in forward seas. The variations in forward speed and effects on rudder lift and turning ability change the shape of the hybrid method trajectories relative to the VOF predictions.

The sway velocity is also underpredicted for the longevity of the maneuver, as is shown in Figure 4.19. The drift angle shows reasonable agreement because both forward speed and sway velocity are proportionally underpredicted.

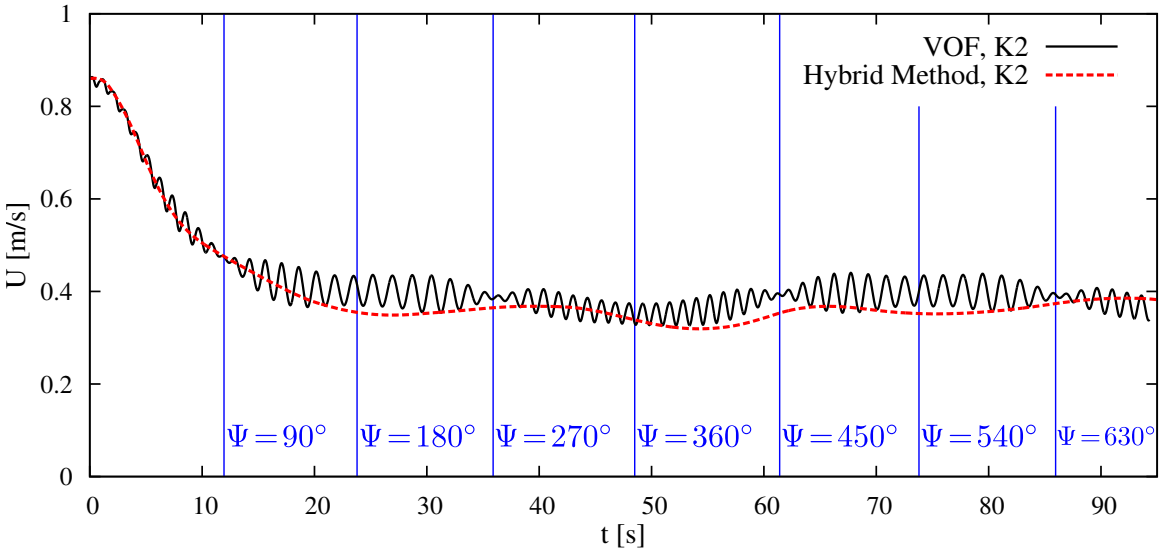

Figure 4.18: VOF and hybrid method forward speed of KCS turning in waves

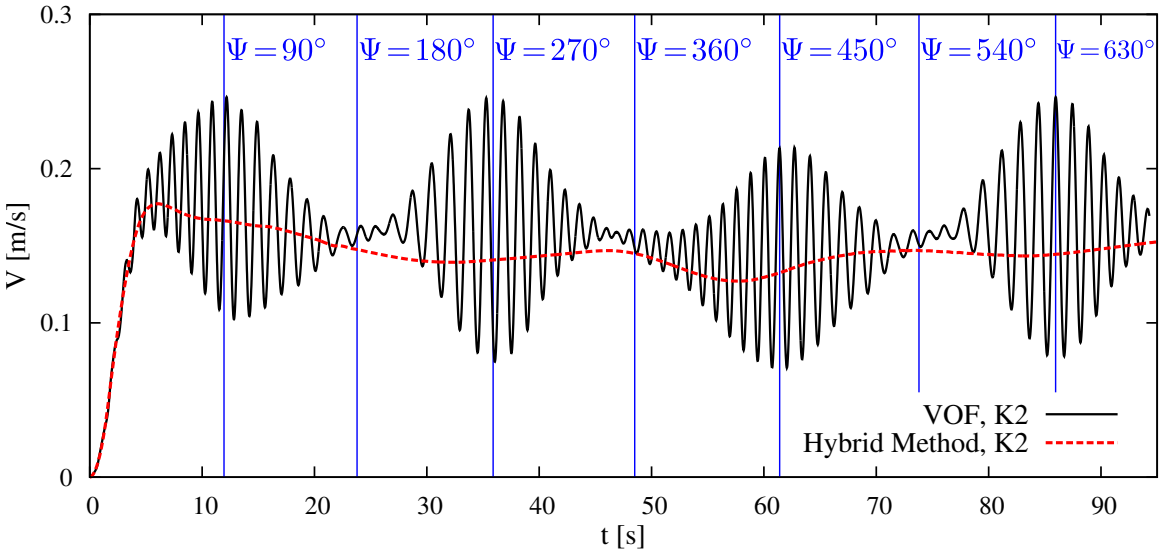

Figure 4.19: VOF and hybrid method sway velocity of KCS turning in waves

Figure 4.21 displays the yaw rate predicted by each of the two methods. Similar to the findings with the DTC hull, the yaw rate is underpredicted by the hybrid method in following seas. One difference from the findings on the DTC hull is that the yaw rate here is underpredicted through the initial turn out of head seas as a result of neglecting roll motion in the hybrid method. However, the prediction by the hybrid method shows a slightly larger yaw rate turning back through head seas ($\Psi = 360°$), consistent with the findings on the DTC hull.

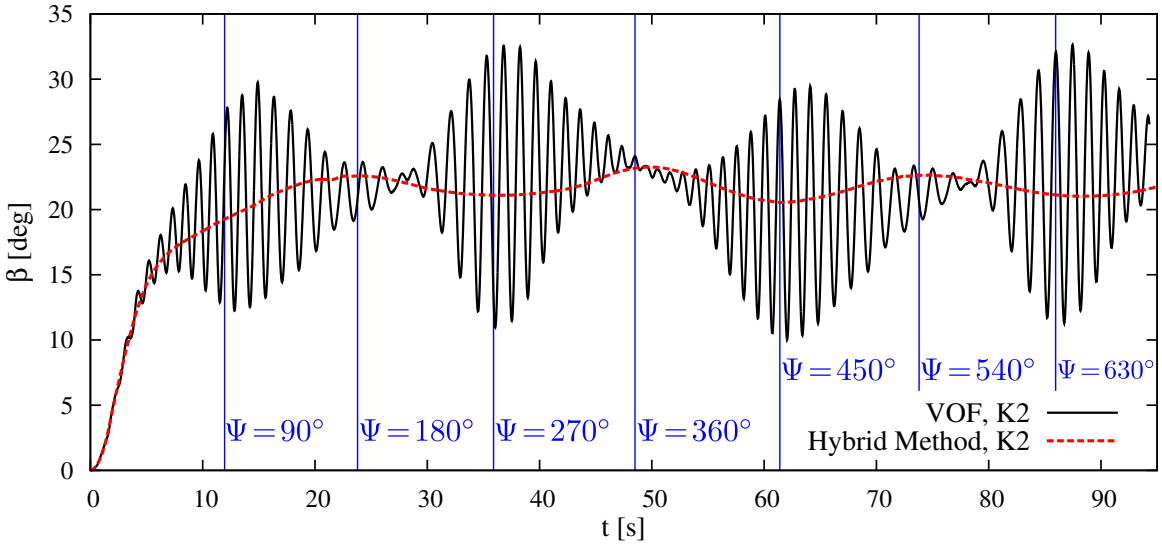

Figure 4.20: VOF and hybrid method drift angle of KCS turning in waves

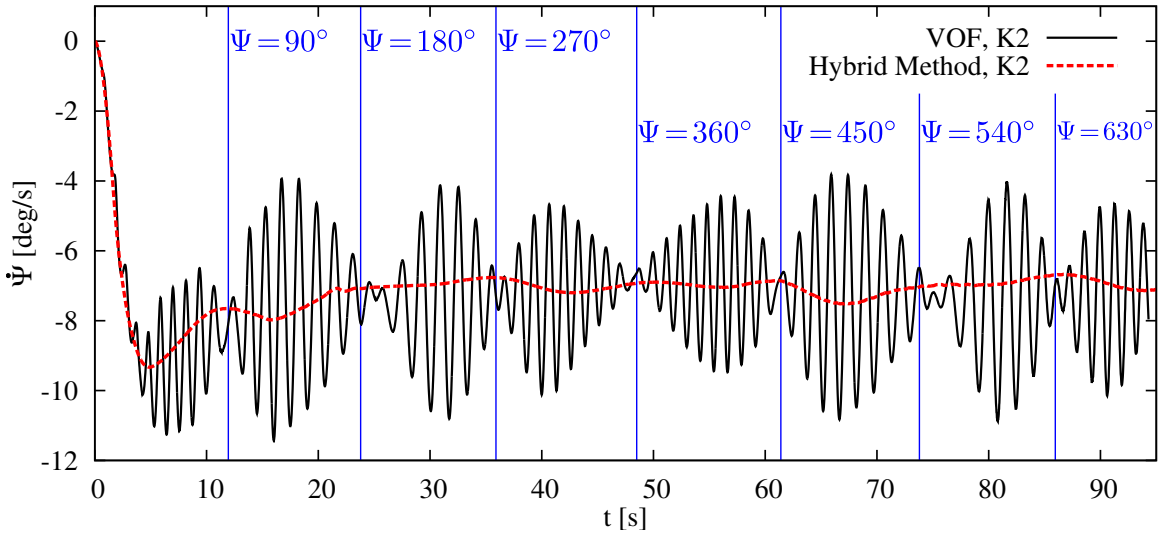

Figure 4.21: VOF and hybrid method yaw rate for KCS turning in waves

Figure 4.22 displays the surge force predicted by the VOF and hybrid methods. The envelopes of surge force agree well with the hybrid method producing slightly larger peak to trough amplitude of surge force. Furthermore, the surge force predicted with the hybrid method is oscillating about a slightly larger mean value of surge force, consistent with the additional speed loss witnessed in the forward speed plot.

The sway force is shown in Figure 4.23. The sway force envelope computed by the hybrid method is well aligned with the VOF results. One point of interest in these

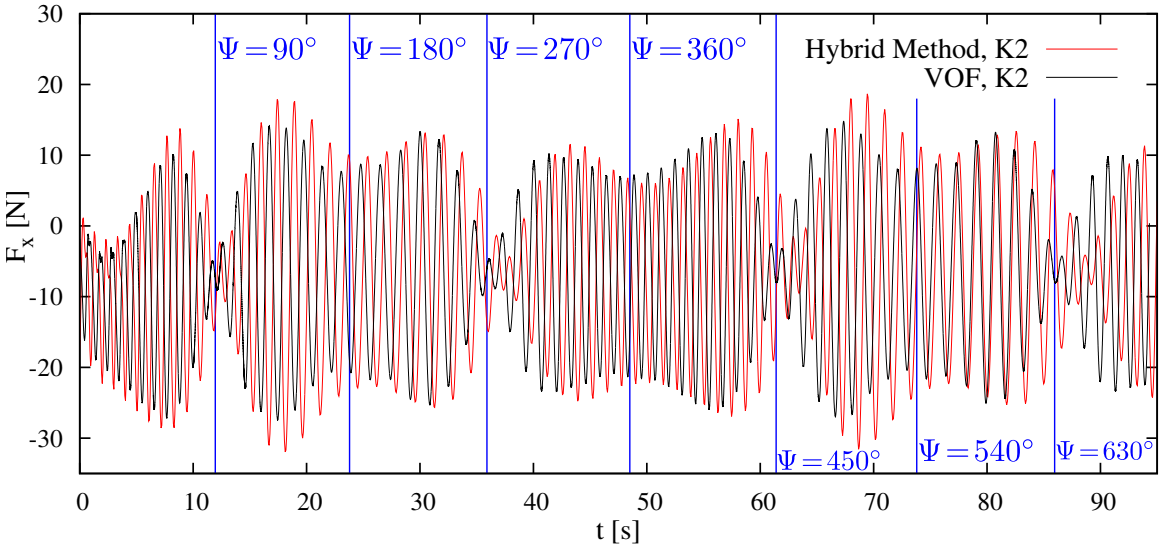

Figure 4.22: VOF and hybrid method surge forces (neglecting thrust) throughout KCS turn in waves

results is that the total sway force reproduced from the hybrid method overpredicts the VOF forcing envelope in beam seas from the port side ($\Psi = 90°$ and $\Psi = 450°$) but slightly underpredicts the peak to trough sway force in beam seas from the starboard side ($\Psi = 270°$ and $\Psi = 630°$).

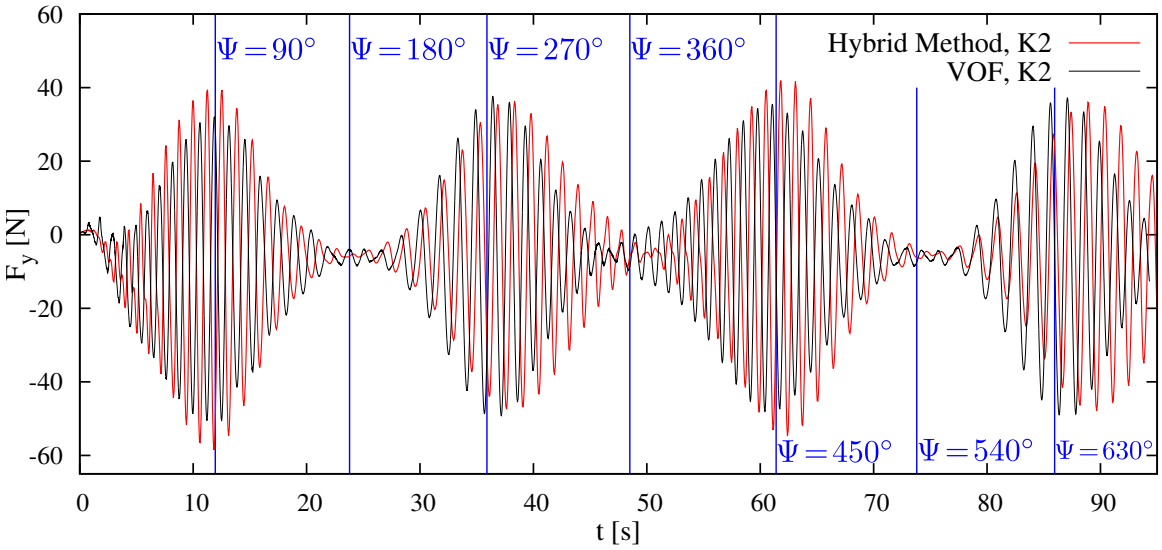

Figure 4.23: VOF and hybrid method sway force throughout KCS turn in waves

Lastly, the total yaw moment is illustrated in Figure 4.24. The findings closely reflect what was exhibited in the DTC hull turning circle in waves. The largest devi-

ations between VOF and the hybrid method are found in oblique sea states, with the hybrid method predicting a larger (negative) moment (moment into starboard turn) compared to the VOF from $\Psi = 0° \rightarrow 90°$. The hybrid method again overpredicts moment (into turn) turning out of head seas from $\Psi = 360° \rightarrow 450°$. The mean yaw moment from the hybrid method is predicted as positive (out of turn) when the vessel is turning into following seas ($(\Psi = 90° \rightarrow 180°$ and again during $\Psi = 450° \rightarrow 540°$).

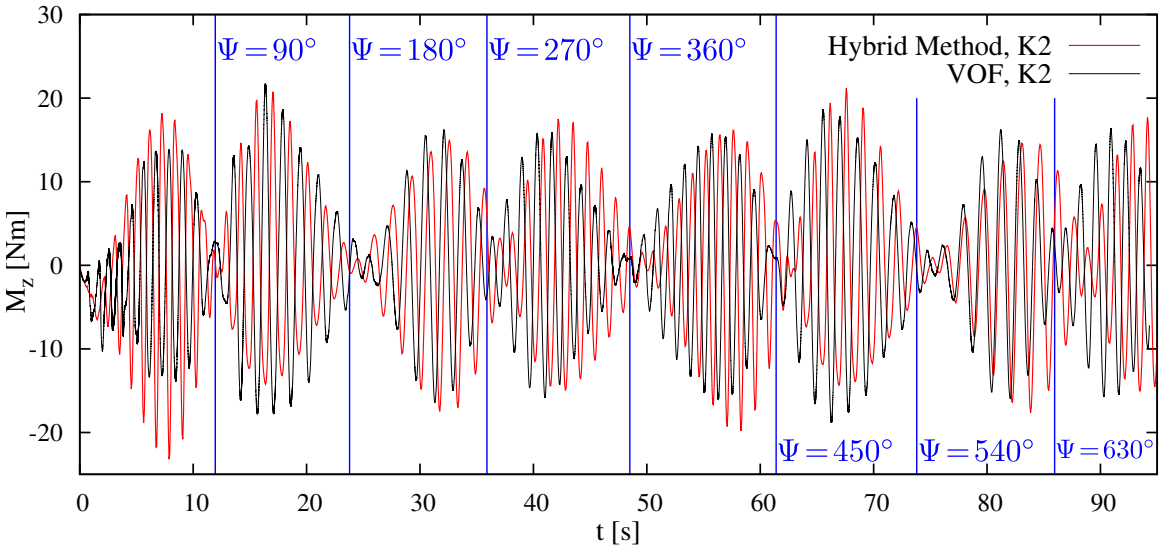

Figure 4.24: VOF and hybrid method yaw moment throughout KCS turn in waves

4.5 Hybrid Method Summary and Computational Cost Comparison

The performance of the hybrid method has been compared to high-fidelity simulations computed with the nonlinear (rigid body dynamics and hydrodynamics) VOF method in the preceding sections. This section provides a numerical comparison between the cost of computing the high-fidelity VOF results and the hybrid method results.

The nonlinear VOF simulations were computed on the Air Force Research Laboratory HPC Thunder. The Thunder HPC features just over 3,200 standard memory

compute nodes with 36 cores per node. The processor architecture on the Thunder HPC is Intel® Xeon® E5-2699v3. Each core possesses a base processor frequency of 2.30 GHz.

The hybrid method simulations for the KCS hull were computed on an HP® desktop running the Ubuntu 14.04 distribution of Linux. The desktop contains two Intel® Xeon® E5-2640 (Sandy Bridge architecture) processors, each with base processor frequency of 2.50 GHz. The BEM was run in serial and, as it was only called every eight CFD time steps, it was not allocated a processor of its own; the task of balancing the twelve cores devoted to solving the CFD and the occasional extra task of solving the BEM was left to the operating system. Testing revealed that the hybrid method run times were slightly reduced when using the dual-threading technology built into the processors and allowing the operating system to handle the extra load of the BEM solution, as opposed to reserving an entire core for the solution of the BEM.

The following aspects and simplifications were considered in the computational cost comparison. The numerical comparison here does not attempt to adjust for scalability of the OpenFOAM software as compiled on the Thunder HPC. Furthermore, though an optimum number of finite volume cells per node exists, this comparison does not consider the efficiency of decomposition of the total number of unknown degrees of freedom. Lastly, when comparing the cost savings of the hybrid method to the VOF method, the 0.20 GHz differential between processor frequencies on each of the systems was disregarded. Therefore, the difference in computational cost comparison does not aim to be precise but rather an order of magnitude estimate.

The hybrid method running on the desktop machine required 750 core-hours to simulate 100 s of the maneuver on mesh K1. The VOF method on mesh K1 was run on 3 compute nodes on the Thunder HPC with a total of 144 cores and required 8,500 core-hours to simulate 100 s of the maneuver on mesh K1. Using the simplifying assumptions above, the hybrid method reduced the computing cost on mesh K1 by a

factor of 11.3.

The hybrid method running on the desktop machine required 3,026 core-hours to simulate 100 s of the maneuver on mesh K2. The VOF method on mesh K2 was run on 4 compute nodes on the Thunder HPC with a total of 192 cores and required 30,342 core-hours to simulate 100 s of the maneuver. The computational cost reduction when using the hybrid method amounted to a factor of 10.0. A summary of cost comparison between the VOF method and hybrid method for the KCS simulations is provided in Table 4.7.

Table 4.7: Cost comparison between hybrid method and VOF in KCS simulations

	Mesh K1	Mesh K2
Cost VOF [cpu-hrs]	8,500	30,342
Cost Hybrid [cpu-hrs]	750	3,026
Cost VOF/Cost Hybrid	11.3	10.0

CHAPTER V

Summary, Contributions, and Future Work

5.1 Summary and Contributions

A hybrid computational method is formulated for the combined solution of a ship maneuvering and seakeeping in a seaway. The hybrid method is designed in a modular way to accurately predict relevant physics in the maneuvering in waves problem while doing so at a reduced computational cost compared to pure CFD approaches. A single-phase, incompressible RANS solution is adopted for its ability to predict viscous and pressure forces that govern the horizontal plane maneuvering dynamics. The wave modeling is removed from the RANS computations and instead addressed through a potential-flow solution using the Boundary Element Method (BEM). The linear time-domain BEM provides a more efficient, yet accurate, way of computing the seakeeping motions and second-order wave loads. The hybrid method utilizes a surrogate model for the propulsion forces (Knight and Maki, 2019, 2020) which in turn permits a larger time-step within the CFD due to removal of the discrete propeller. The rudder is discretized within the CFD and treated with a sliding mesh technique to resolve the flow and resulting steering forces.

The outline of the hybrid formulation in Chapter II describes two ways in which the maneuvering and seakeeping problems are coupled. The three degree of freedom equations of motion are forced by the hull and rudder forces from the RANS compu-

tation, the propeller model forces, and the second-order wave loads which are derived from the seakeeping problem. The solution to the slowly-varying horizontal plane motion drives the mesh motion within the CFD thereby impacting the hydrodynamic response to the vessel maneuvering motions. Meanwhile, the seakeeping problem is linearized about a frame that follows the slowly-varying horizontal plane maneuvering motions. This particular linearization introduces the maneuvering velocities and yaw rate into the BVP's. Furthermore, the position of the ship with respect to the Earth-fixed origin and the maneuvering velocities are used to adjust the incident wave potential in the maneuvering frame, accounting for the ship turning relative to the wave and varying encounter frequency. The result is a two-way-coupled simulation method in which the potential flow seakeeping solution is evolved concurrently with the horizontal plane RANS solution.

Chapter III presents a study on the maneuvering characteristics of the Duisburg Test Case (DTC) hull form. The study first verifies adequate resolution in the mesh built for VOF simulations by computing heave, pitch, and added resistance RAO's for the DTC at $Fn = 0.14$. The VOF computations correspond well with experimental values in the motion RAO's and the added resistance RAO. The calm-water turning circle (35° rudder) of the DTC hull is computed for initial speed of 1.48 m/s ($Fn = 0.2$) using both a simplified hybrid method and also the nonlinear VOF; the two approaches show excellent agreement. Then the performance of DTC hull turning in waves is investigated by comparing computations made with the proposed hybrid method to high-fidelity VOF computations. The trajectories computed with the hybrid method agree well with the results generated using the VOF method. After a simulated time of $t = 110$ s, which corresponds to roughly 630° of heading change, the trajectories are separated by less than $0.3L$.

Chapter IV presents the second test case for the combined seakeeping and maneuvering performance of the KCS hull in regular waves. Seakeeping and added resistance

computations are first computed using the VOF method. The VOF method shows excellent agreement with experimental motion and added resistance RAO's. The calm-water turning circles are then predicted using both the hybrid approach and VOF method at an initial speed of 0.86 m/s ($Fn = 0.157$). The hybrid method predicts the advance and turning diameter well in comparison to the VOF computations, but the hybrid method overpredicts the maximum transfer distance (the maximum excursion of the ship's center of gravity in a direction perpendicular to the ship's initial course before turn).

Chapter IV also includes turning circle predictions into an initial head regular sea state using both the hybrid method and VOF method. The resulting trajectories show less drift than with the parameters of the maneuver for the DTC hull in Chapter III. The hybrid method roughly shows an ability to represent the turning circle in waves. Differences between hybrid method and VOF results are noted in turning diameter and the drift direction. These differences are explained by excessive loss of forward speed in the hybrid method and therefore different exposure windows to various wave headings; the exposure to a certain wave heading ultimately governs the drift distance and direction. The overpredicted loss in forward speed and lag in trajectory of the hybrid method relative to VOF prediction is an effect witnessed in the calm-water circle that carries over to the computation in waves.

The computational savings of the hybrid method are shown to be appreciable over a comparable simulation using the nonlinear VOF method. Table 5.1 summarizes the recorded computational expenses from turning circle in waves simulations in Chapters III and IV. The hybrid method demonstrates an efficiency gain by at least a factor of ten for the four cases tested in this thesis. The hybrid method simulations in this work were computed on meshes with identical discretization below the $z = 0$ calm-water plane and with the air-phase of the VOF mesh truncated. Although this practice was followed in this thesis for consistent comparison, further computational

gains are possible with decreasing mesh density in the hybrid mesh far-field. Without incident waves present in the RANS component of the hybrid method, mesh discretization can be relatively coarse away from the ship hull boundary.

Table 5.1: Cost comparison between hybrid method and VOF method

	DTC D1	DTC D2	KCS K1	KCS K2
Cost VOF [cpu-hrs]	4,145	26,625	8,500	30,342
Cost Hybrid [cpu-hrs]	403	1,354	750	3,026
Cost VOF/Cost Hybrid	10.2	19.5	11.3	10.0

5.2 Future Work

A next investigation for improvement of the method is to pass entire maneuvering state vector to BVP's. While the analytic incident wave potential in this work includes the position, heading, and maneuvering velocities within the horizontal plane, the BVP's are only informed of changes in forward speed in this work, i.e. $\mathbf{W} = \{U(t), 0, 0\}^T$. The maneuvering vector, $\mathbf{W}$, that enters into the BVP's in Chapter II should include time dependent yaw rate and sway velocity in addition to forward speed. As a consequence of this simplification, evolution of radiated and diffracted waves occurs as if the ship was on straight course. This is not an unreasonable assumption for large turning diameters. The second-order wave moment is a quantity that could be expected to improve from full treatment of the turning ship within the maneuvering frame BVP's.

A second extension of this work is to add the roll degree of freedom to the low-frequency maneuvering equations. The calm-water simulations for the KCS demonstrate a sensitivity to either roll angle or inclusion of free-surface effects (or both). The calm-water trajectory computed using the hybrid method without roll shows differences from the nonlinear VOF method. The differences in calm water are recognizable again in the simulations in waves. The inclusion of roll is accomplished by

building a mesh with an air-phase and thus allowing free-surface capturing. The mesh can be very coarse in the far-field as the only source of waves within the domain is the steady radiated wave from the ship. Moreover, the computations can be performed at a similar efficiency level to the single-phase hybrid method results demonstrated in this thesis.

A final extension of this work is to attempt simulation in irregular sea states. The formulation described in this thesis is easily extended to irregular sea states without the force time-averaging explained in Chapter II. While applying the time-averaged force to the maneuvering motions is consistent with the two-time-scale method, the results of Chapter III demonstrate it is unnecessary in practice to average. Extension of the incident regular wave to irregular wave in the BEM is trivial.

APPENDICES

APPENDIX A

Wave Generation in OpenFOAM VOF Framework

The theory behind the two-phase incompressible VOF method and the RANS solver was presented in Chapter II. The wave generation method is now described, beginning with a description of the numerics and followed by a description of grid topology and resolution requirements for propagating a wave using the VOF method. Lastly, spatial and temporal convergence are shown from computations without the ship present. The convergence study is presented to demonstrate that the quality of the incident wave is sufficient for practical usage in wave-body interaction problems using the VOF method.

In this work, waves are generated through a relaxation zone approach (Jacobsen et al., 2012; Filip et al., 2017). The relaxation zone is a region of space where prescribed wave kinematics are blended with the computed solution from the FVM. The blending between computed value, ϕ_{comp}, and prescribed value, ϕ_{BC}, follows the relationship given in Equation A.1, where the blending function, $\chi(\sigma)$, is a third-order polynomial in the nondimensional radial coordinate, σ.

$$\begin{aligned} \phi &= \chi(\sigma)\phi_{\text{BC}} + (1 - \chi(\sigma))\phi_{\text{comp}} \\ \chi(\sigma) &= 2\left(1-\sigma\right)^3 - 3\left(1-\sigma\right)^2 + 1 \end{aligned} \tag{A.1}$$

The radial coordinate is defined in Equation A.2 in terms of an inner and outer radius of the annular relaxation zone, as shown in Figure A.1. Figure A.1 also shows the radial distribution of the blending function magnitude.

$$\sigma = \frac{r - r_i}{r_i - r_o} \tag{A.2}$$

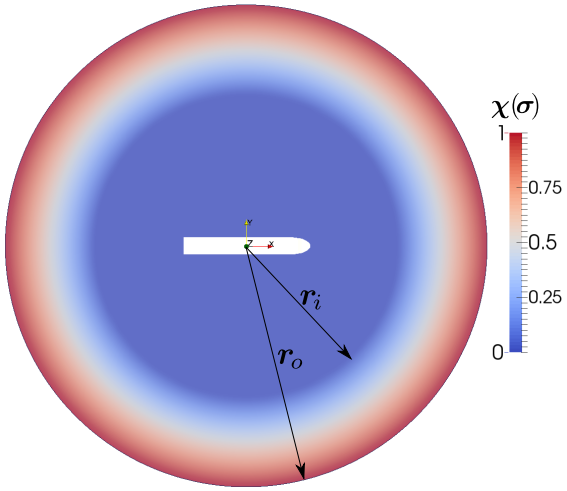

Figure A.1: Maneuvering coordinate system.

The blending function is independent of depth and therefore the weight on the prescribed value has the same lateral distribution throughout the depth of the domain. Numerically, the blending relationship given in Equation A.1 is enforced through addition of a source term to both the momentum equation and phase fraction equation. Referring back to the definition of a source term in Equation 2.23, the source term for wave generation for cell P is given in Equation A.3. It should be noted that $\chi(\sigma) > 0$ and so the implicit term can always be treated implicitly and added onto the diagonal of the linear system.

$$\mathbf{S}^{\phi} = \mathbf{S}_u + \mathbf{S}_p \phi_P = \chi(\sigma)\phi_{\mathrm{BC}} - \chi(\sigma)\phi_P \tag{A.3}$$

The topology and resolution of the grids is now described. The domain is a

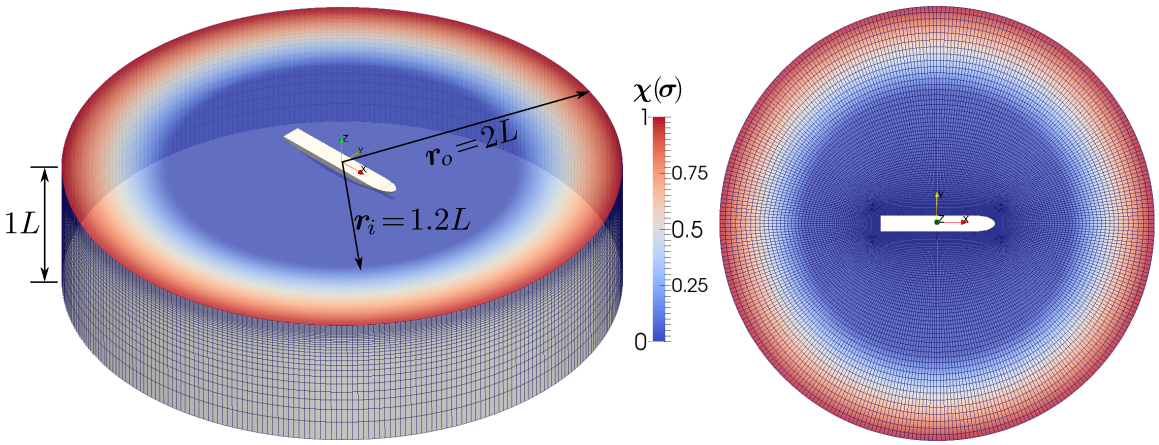

(a) (b)

Figure A.2: (a) Isometric view of mesh D1 ($z > 0$ truncated) (b) Plan view of discretization for mesh D1

cylindrical domain, centered at the mesh origin. The grids utilized for this convergence test are identical to the grids used in Chapter III for the Duisberg Test Case hull, with the exception that the hull is not present in the wave generation study. Nevertheless, the hull is displayed for reference in Figure A.2 and dimensions of the domain are nondimensionalized with reference to the length between perpendiculars of the DTC hull, ($L = 5.577$ m).

The mesh used in the wave generation study is a multiblock (O-H type) hexahedral mesh. The mesh contains a rectangular prismatic region with uniform, orthogonal cells in all three coordinate directions. The prismatic region is large enough to encompass the geometry of the ship hull and rudder, which is required to create the meshes used in Chapter III. The hexahedral meshes used in the wave generation study are created using the meshing software *Pointwise*. Table A.1 provides some metrics of the three refinement levels presented in this study. Two different measures of refinement in the streamwise x-direction are presented, primarily because of stretching and anisotropy in the domain. The first metric presents the number of cells per wavelength, λ, using an average cell length in the x-direction, entitled $\overline{\Delta x}$. The generated wave in this convergence study has the following properties that match the turning

circle test in Chapter III: $\lambda = 5.577$ m and $H = 0.111$ m. The average x-direction cell size is computed by dividing the diameter by the number of cells across the diameter in the x-direction at the $y = 0$ centerline plane. The second metric for x-direction discretization is cells per wavelength using the x-direction cell length in the isotropic region within the rectangular prism. This metric describes discretization along the hull. The three meshes are refined systematically in all three directions by a factor of $\sqrt{2}$, with the mesh labeled $D1$ being the coarsest. Lastly, the number of cells per wave height is listed.

Table A.1: Mesh refinement parameters

	D1	D2	D3
# of cells	1,228,416	3,400,012	9,808,816
$\lambda/\overline{\Delta x}$	60.1	84.7	116.9
$\lambda/\Delta x$ (uniform near hull)	110	160	220
$H/\Delta z$	2.2	3.1	4.4

The waves are generated on a translating grid using the Arbitrary Eulerian Lagrangian approach. The speed of the domain is prescribed as a half-cosine profile and then held constant. The time evolution of the wave field is solved for approximately 16 encounter periods. The coarsest mesh, D1, exhibits some loss of wave amplitude at $X/L = -0.5$ in Figure A.3(a) though the wave elevation is within $\approx 5\%$ of the results on meshes D2 and D3. Figure A.3(b) presents results from three different temporal discretizations using the spatial discretization from mesh D2. The wave computed using 350 time steps per wave period is the only grid to show noticeable decay in wave amplitude. The results computed using 750 and 1000 time steps per wave period are indistinguishable.

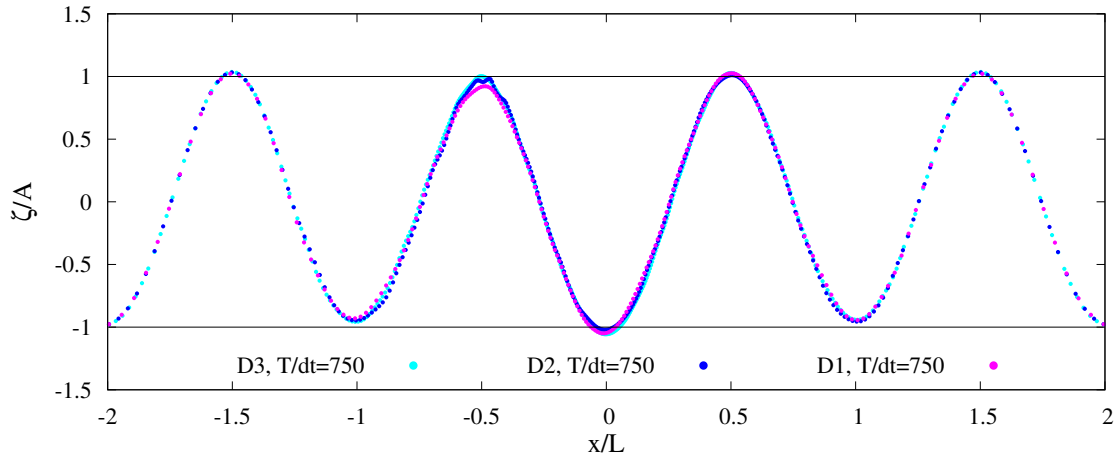

(a)

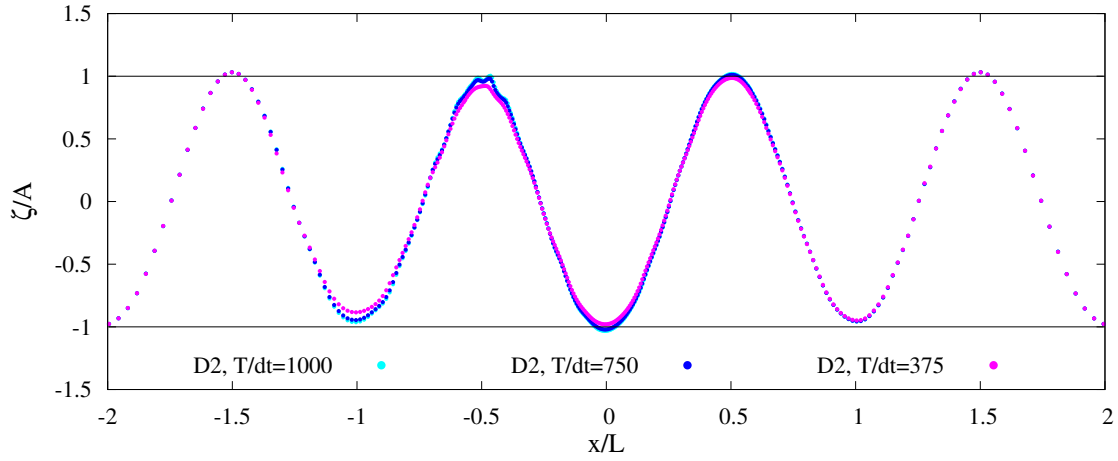

(b)

Figure A.3: (a) Wave sensitivity to spatial discretization (b) Wave sensitivity to temporal discretization

APPENDIX B

Horizontal Plane Maneuvering Forces for DTC hull

The presented method is not at present able to simulate the maneuvering low-frequency radiated waves by virtue of selecting a viscous double-body RANS solution to model the non-oscillatory hydrodynamic derivatives. This section undergoes a study to justify neglecting steady sway force and yaw moment due to a slowly varying ship maneuver at two Froude numbers for the Duisburg Test Case (DTC) hull form.

The numerical experiment involves static drift tests at $\beta = 0°, 5°, 10°, 15°$ at $F_{n,V} = |\vec{V}|/\sqrt{gL} = 0.15$ and $Fn = 0.2$. For each test case, a single-phase double-body (DB) Reynolds-averaged Navier-Stokes (RANS) simulation and a VOF method with free surface capturing are simulated. The Froude number based on ship speed, $|\vec{V}| = \sqrt{U^2 + V^2}$, is held constant while increasing static drift angle. The kinematic viscosity is adjusted for all cases at $Fn_V = 0.15$ to maintain Reynolds number similarity, and so any deviation in wave force due to the viscosity is not captured in this test. The non-dimensional surge force, sway force, and moment are shown in Figures B.1(a)-(d), whereas the nondimensionalization is defined in Equation B.1.

$$(X', Y', N'/L) = \frac{(F_x, F_y, M_z/L)}{\frac{1}{2}\rho|\vec{V}|^2 LT} \tag{B.1}$$

Figure B.1(a) shows that under this scaling (with adjusted kinematic viscosity) the nondimensional surge force from DB RANS exhibits no dependence on Fn_V as expected. The VOF method at $Fn_V = 0.15$ shows a weak dependence on drift angle that exhibits the same trend as the single-phase DB RANS approach. The approximately constant offset between the DB RANS surge force and VOF results is due to steady wave resistance. The VOF results at $Fn_V = 0.2$ indicate a stronger dependence on drift angle and the VOF results show larger deviation from the DB RANS results as β increases.

Figures B.1(b) and B.1(c) show excellent agreement between DB RANS forces and those from the VOF method. This indicates that drift angle dependence on sway force and yaw moment due to the low-frequency maneuvering motion can be accurately captured by single-phase simulations for the range of drift angles and Froude numbers tested here. Further, the component of sway force and yaw moment due to wave-making is only weakly dependent on drift angle.

The nondimensional surge force using the single-phase DB RANS solution are improved by adding the steady wave resistance. The steady wave resistance is obtained in this work by applying the steady body boundary condition, $\vec{W} \cdot \hat{n} = Un_1$, within the potential-flow method. This simplification takes the zero drift angle steady wave resistance and applies it to the surge force for all drift angles. Figure B.1(d) shows that this simple correction is sufficient for $Fn_V = 0.15$ but does not capture the β-dependence of forces and moments related to wave-making at $Fn_V = 0.2$.

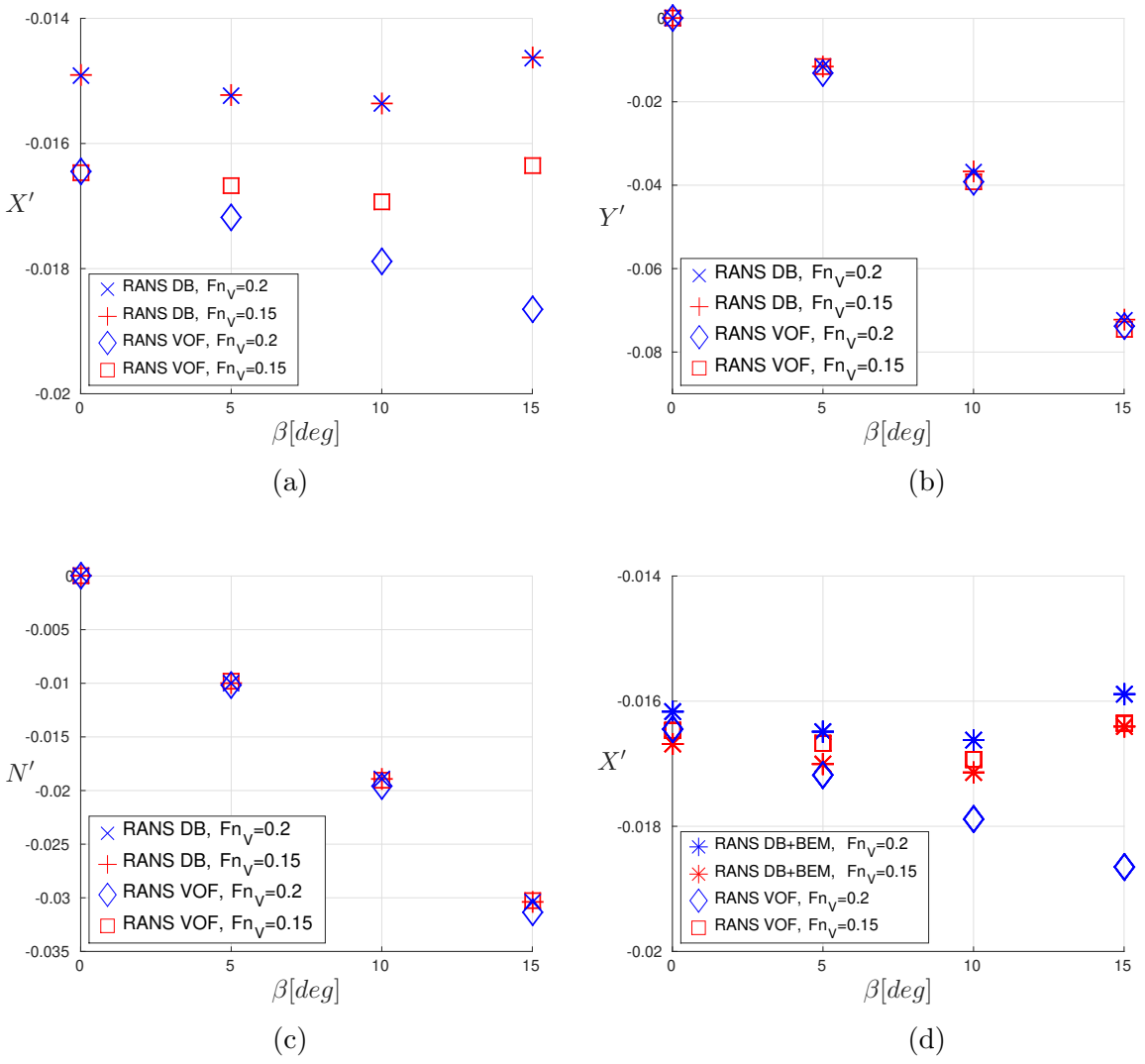

Figure B.1: (a) Nondimensional surge force vs. drift angle (b) Nondimensional sway force vs. drift angle (c) Nondimensional yaw moment vs. drift angle (d) Improved nondimensional surge force with addition of first-order wave resistance

BIBLIOGRAPHY

BIBLIOGRAPHY

Abkowitz, M. (1964). Lectures on ship hydrodynamics - steering and manoeuverability, Report Hy-5. Technical report, Hydro- and Aerodynamics Laboratory, Lyngby, Denmark.

American Bureau of Shipping (2017). ABS Guide for Vessel Maneuverability. Technical report, American Bureau of Shipping, Houston, Texas.

Ashford, G. A. (1996). *An unstructured grid generation and adaptive solution technique for high-Reynolds-number compressible flows*. PhD thesis, University of Michigan.

Bonci, M., Viviani, M., Broglia, R., and Dubbioso, G. (2015). Method for estimating parameters of practical ship manoeuvring models based on the combination of RANSE computations and System Identification. *Applied Ocean Research*, 52:274–294.

Boris, J. P. and Book, D. L. (1973). Flux-corrected transport. I. SHASTA, a fluid transport algorithm that works. *Journal of Computational Physics*, 11(1):38–69.

Carrica, P. M., Ismail, F., Hyman, M., Bhushan, S., and Stern, F. (2013). Turn and zigzag maneuvers of a surface combatant using a URANS approach with dynamic overset grids. *Journal of Marine Science and Technology (Japan)*, 18(2):166–181.

Chillcce, G. and el Moctar, O. (2018). A numerical method for manoeuvring simulation in regular waves. *Ocean Engineering*.

Cura-Hochbaum, A. and Uharek, S. (2016). Prediction of ship manoeuvrability in waves based on RANS simulations. *31st Symposium on Naval Hydrodynamics*, (September):11–16.

Dawson, C. (1977). A practical computer method for solving ship-wave problems. In *2nd International Conference on Numerical Ship Hydrodynamics*.

Deshpande, S. S., Anumolu, L., and Trujillo, M. F. (2012). Evaluating the performance of the two-phase flow solver interFoam. *Computational Science and Discovery*, 5(1).

el Moctar, O., Shigunov, V., and Zorn, T. (2012). Duisburg test case: Post-panamax container ship for benchmarking. *Ship Technology Research*, 59(3):50–64.

el Moctar, O., Sprenger, F., Schellin, T. E., and Papanikolaou, A. (2016). Numerical and experimental investigations of ship maneuvers in waves. *Proceedings of the International Conference on Offshore Mechanics and Arctic Engineering - OMAE*, 2(June).

Faltinsen, O. M., Minsaas, K. J., Liapis, N., and Skjordal, S. O. (1981). Prediction of resistance and propulsion of a ship in a seaway. In *13th Symposium on Naval Hydrodynamics*, pages 505–529, Tokyo, Japan.

Farrell, P. E. and Maddison, J. R. (2011). Conservative interpolation between volume meshes by local Galerkin projection. *Computer Methods in Applied Mechanics and Engineering*.

Fenton, J. D. (1985). A fifth-order Stokes theory for steady waves. *Journal of Waterway, Port, Coastal and Ocean Engineering*.

Filip, G. P., Xu, W., and Maki, K. J. (2017). URANS predictions of resistance and motions of the KCS in head waves. Technical Report 355, University of Michigan Department of Naval Architecture and Marine Engineering, Ann Arbor, Michigan.

Fossen, T. I. (2005). A nonlinear unified state-space model for ship maneuvering and control in a seaway. *International Journal of Bifurcation and Chaos in Applied Sciences and Engineering*, 15(9):2717–2746.

Gaskell, P. H. and Lau, A. K. C. (1988). Curvature-compensated convective transport: SMART, A new boundedness- preserving transport algorithm. *International Journal for Numerical Methods in Fluids*, 8(6):617–641.

Godunov, S. K. (1959). Finite difference method for numerical computation of discontinuous solutions of the equations of fluid dynamics. *Matematicheskii Sbornik*, 47:271–306.

Greenwood, D. T. (2003). *Advanced Dynamics*. Cambridge University Press, New York City.

Harten, A. (1983). High resolution schemes for hyperbolic conservation laws. *Journal of Computational Physics*.

Hirano, M., Takashina, J., Takaishi, Y., and Saruto, T. (1980). Ship Turning Trajectory in Regular Waves. *Transaction of The West-Japan Society of Naval Architects*.

Hirt, C. W. and Nichols, B. D. (1981). Volume of fluid (VOF) method for the dynamics of free boundaries. *Journal of Computational Physics*, 39(1):201–225.

Hoekstra, M. (2006). A RANS-based analysis tool for ducted propeller systems in open water condition. *International Shipbuilding Progress*.

Issa, R. I. (1986). Solution of the implicitly discretised fluid flow equations by operator-splitting. *Journal of Computational Physics*, 62(1):40–65.

ITTC (2008). The Maneuvering Committee: final report and recommendations to the 25th ITTC. In *Proceedings of 25th ITTC*, volume I, pages 143–208.

Jacobsen, N. G., Fuhrman, D. R., and Fredsøe, J. (2012). A wave generation toolbox for the open-source CFD library: OpenFoam®. *International Journal for Numerical Methods in Fluids*, 70:1073–1088.

Joncquez, S. A. G. (2009). *Second order forces and moments acting on ships in waves*. PhD thesis, Technical University of Denmark.

Khosla, P. K. and Rubin, S. G. (1974). A diagonally dominant second-order accurate implicit scheme. *Computers and Fluids*, 2(2):207–209.

Kim, K. H., Seo, M. G., and Kim, Y. (2012). Numerical analysis on added resistance of ships. *International Journal of Offshore and Polar Engineering*, 22(1):21–29.

Knight, B. and Maki, K. (2020). Multi-degree of freedom propeller force models based on a neural network and regression. *Journal of Marine Science and Engineering*, 8(2):89.

Knight, B. G. and Maki, K. J. (2018). Body force propeller model for unsteady surge motion. In *Proceedings of the International Conference on Offshore Mechanics and Arctic Engineering - OMAE*.

Knight, B. G. and Maki, K. J. (2019). A semi-empirical multi-degree of freedom body force propeller model. *Ocean Engineering*.

Larsson, L., Stern, F., and Visonneau, M. (2013). CFD in ship hydrodynamics - Results of the Gothenburg 2010 workshop. In *Computational Methods in Applied Sciences*.

Larsson, L., Stern, F., Visonneau, M., Hino, T., Hirata, N., and Kim, J. (2015). Proceedings, Tokyo 2015 Workshop on CFD in Ship Hydrodynamics. In *Tokyo CFD Workshop*.

Lee, J. H. and Kim, Y. (2020). Study on steady flow approximation in turning simulation of ship in waves. *Ocean Engineering*, 195.

Loukakis, T. A. and Sclavounos, P. D. (1978). Some extensions of the classical approach to strip theory of ship motions, including the calculation of mean added forces and moments. *Journal of Ship Research*, 22(1):1–19.

Luo, W., Soares, C. G., and Zou, Z. (2013). Parameter identification of ship manoeuvring model based on particle swarm optimization and support vector machines. *Proceedings of the International Conference on Offshore Mechanics and Arctic Engineering - OMAE*, 5(January 2015).

Lyu, W. and el Moctar, O. (2017). Numerical and experimental investigations of wave-induced second order hydrodynamic loads.

Maruo, H. (1960). The drift of a body floating on waves. *Journal of Ship Research*, 4:1–5.

McCreight, W. R. (1986). Ship maneuvering in waves. In Webster, W., editor, *Sixteenth Symposium on Naval Hydrodynamics*, pages 456–469, Berkeley, California.

Moukalled, F., Mangani, L., and Darwish, M. (2016). *The finite volume method in computational fluid dynamics : An Advanced Introduction with OpenFOAM and Matlab*. New York City, 1 edition.

Ogilvie, T. (1964). Recent progress toward the understanding and prediction of ship motions. In *5th Symposium on Naval Hydrodynamics*, pages 3–80, Bergen, Norway.

Ogilvie, T. and Tuck, E. (1969). A rational strip theory for ship motions, part 1. Technical report, Department of Naval Architecture and Marine Engineering, University of Michigan.

Oltmann, P. (1993). Roll - an often neglected element of manoeuvring. In *International Conference on Marine Simulation and Ship Manoeuvrability*, pages 463–471, St. John's, Canada.

Piro, D. J. (2013). *A Hydroelastic method for the analysis of global response due to slamming events*. PhD thesis, University of Michigan.

Rusche, H. (2002). *Computational Fluid Dynamics of Dispersed Two-Phase Flows at High Phase Fractions*. PhD thesis, Imperial College of Science, Technology & Medicine.

Sadat-Hosseini, H., Toxopeus, S., Kim, D. H., Sanada, Y., Stocker, M., Otzen, J. F., Toda, Y., and Stern, F. (2015). Experiments and computations for KCS added resistance for variable heading. *5th World Maritime Technology Conference*.

Salvesen, N. (1974). Second-order steady-state forces and moments on surface ships in oblique regular waves. In *International Symposium on the Dynamics of Marine Vehicles and Structures in Waves*, number 1974, pages 225–241.

Sanada, Y., Tanimoto, K., Takagi, K., Gui, L., Toda, Y., and Stern, F. (2013). Trajectories for ONR Tumblehome maneuvering in calm water and waves. *Ocean Engineering*, 72:45–65.

Seo, M. G. and Kim, Y. (2011). Numerical analysis on ship maneuvering coupled with ship motion in waves. *Ocean Engineering*, 38(17-18):1934–1945.

Shen, Z., Wan, D., and Carrica, P. M. (2015). Dynamic overset grids in OpenFOAM with application to KCS self-propulsion and maneuvering. *Ocean Engineering*, 108:287–306.

Skejic, R. and Faltinsen, O. M. (2008). A unified seakeeping and maneuvering analysis of ships in regular waves. *Journal of Marine Science and Technology*, 13(4):371–394.

Söding, H., Shigunov, V., Schellin, T. E., and El Moctar, O. (2014). A Rankine panel method for added resistance of ships in waves. *Journal of Offshore Mechanics and Arctic Engineering*, 136(3):1–7.

Son, K. H. and Nomoto, K. (1981). On the coupled motion of steering and rolling of a high-speed container ship. *Journal of the Society of Naval Architects of Japan*, 1981(150):232–244.

Spalart, P. R. and Allmaras, S. R. (1994). One-equation turbulence model for aerodynamic flows. *Recherche aerospatiale*, (1):5–21.

Spalding, D. B. (1961). A single formula for the "law of the wall". *Journal of Applied Mechanics, Transactions ASME*, (September).

Strøm-Tejsen, J. and Chislett, M. S. (1966). A model testing technique and method of analysis for the prediction of steering and manoeuvring qualities of surface vessels. In *Sixth Symposium on Naval Hydrodynamics*.

Subramanian, R. and Beck, R. F. (2015). A time-domain strip theory approach to maneuvering in a seaway. *Ocean Engineering*, 104(August 2015):107–118.

Sweby, P. K. (1984). High resolution schemes using flux limiters for hyperbolic conservation laws. *SIAM Journal on Numerical Analysis*.

Timman, R. and Newman, J. N. (1962). The coupled damping coefficients of a symmetric ship. *Journal of Ship Research*, 5:1–7.

Triantafyllou, M. S. (1982). Consistent hydrodynamic theory for moored and positioned vessels. *Journal of Ship Research*, 26(2):97–105.

Uharek, S. and Cura-Hochbaum, A. (2018). Power prediction for safe manoeuvring in waves. In *32nd Symposium on Naval Hydrodynamics*, number August, pages 5–10.

van Leer, B. (1974). Towards the ultimate conservative difference scheme. II. Monotonicity and conservation combined in a second-order scheme. *Journal of Computational Physics*, 14(4):361–370.

van Leer, B. (1979). Towards the ultimate conservative difference scheme. V. A second-order sequel to Godunov's method. *Journal of Computational Physics*, 32(1):101–136.

Wang, J. and Wan, D. (2018). Direct simulations of turning circle maneuver in waves using RANS-overset method. *Proceedings of the International Conference on Offshore Mechanics and Arctic Engineering - OMAE*, 11B:1–10.

Waterson, N. P. and Deconinck, H. (2007). Design principles for bounded higher-order convection schemes - a unified approach. *Journal of Computational Physics*, 224(1):182–207.

White, P. F., Knight, B. G., Filip, G. P., and Maki, K. J. (2019). Numerical Simulations of the Duisburg Test Case Hull Maneuvering In Waves. In *SNAME Maritime Convention*, Tacoma, Washington, USA. The Society of Naval Architects and Marine Engineers.

Yasukawa, H. and Nakayama, Y. (2009). 6-DOF motion simulations of a turning ship in regular waves. In *MARSIM '09 Conference, Proceedings*.

Yasukawa, H. and Yoshimura, Y. (2015). Introduction of MMG standard method for ship maneuvering predictions. *Journal of Marine Science and Technology (Japan)*, 20(1):37–52.

Yen, T., Zhang, S., Weems, K., and Lin, W. M. (2010). Development and validation of numerical simulations for ship maneuvering in calm water and in waves. In *28th Symposium on Naval Hydrodynamics*, pages 12–27.

Zalesak, S. T. (1979). Fully multidimensional flux-corrected transport algorithms for fluids. *Journal of Computational Physics*, 31(3):335–362.

Zhang, W., Zou, Z. J., and Deng, D. H. (2017). A study on prediction of ship maneuvering in regular waves. *Ocean Engineering*.